





**Fabrication and Characterization of Integrated Photonic Crystal Cavities  
for Sensing Applications**

**Fabricage en karakterisering van geïntegreerde fotonischekristalcaviteiten  
voor detectietoepassingen**

**Saurav Kumar**

**Promotor: prof. dr. ir. N. Le Thomas  
Proefschrift ingediend tot het behalen van de graad van  
Doctor in de ingenieurswetenschappen: fotonica**

**Vakgroep Informatietechnologie  
Voorzitter: prof. dr. ir. B. Dhoedt  
Faculteit Ingenieurswetenschappen en Architectuur  
Academiejaar 2017 - 2018**



**UNIVERSITEIT  
GENT**

ISBN 978-94-6355-137-3

NUR 950

Wettelijk depot: D/2018/10.500/55



Universiteit Gent  
Faculteit Ingenieurswetenschappen  
en Architectuur  
Vakgroep Informatietechnologie

**Promotor:**

Prof. dr. ir. Nicolas Le Thomas

**Examencommissie:**

Prof. dr. ir. Hendrik Van Landeghem (voorzitter)	Universiteit Gent
Prof. dr. ir. Nicolas Le Thomas (Promoter)	Universiteit Gent
Prof. dr. ir. Dries Van Thourhout	Universiteit Gent
Prof. dr. ir. Peter Bienstman	Universiteit Gent
Prof. dr. ir. Geert Van steenberge	Universiteit Gent
Prof. dr. ir. Andre Skirtach	Universiteit Gent
Prof. dr. ir. Xavier Checoury	Université Paris-Sud

Universiteit Gent  
Faculteit Ingenieurswetenschappen en Architectuur

Vakgroep Informatietechnologie  
Technologiepark-Zwijnaarde 15, B-9052 Gent, België

Tel: +32-9-264 3316  
Fax: +32-9-264 3593

Proefschrift tot het bekomen van de graad van  
Doctor in de ingenieurswetenschappen: fotonica  
Academiejaar 2017-2018



# Dankwoord

This PhD would not have been a success without the support from colleagues, friends, and all my family. First of all, my deepest gratitude goes to professor Nicolas Le Thomas for the countless advice, opportunities, freedom and kind help you have offered to me since the beginning of this PhD project. Thank you for your profound mentorship. Your bright ideas and critical comments have always brought this work to the right track. Thank you for your critical and, at the same time, friendly guidance. I am grateful to jury members of my PhD defense for their suggestions, comments and questions, which helped to improve the quality of this thesis.

Head of the Photonics Research Group at Ghent University, Prof. Roel Baets deserves a special credit for successfully leading our group and creating a pleasant and productive environment for research. The fact that, under his leadership, this research group became one of the largest in the academic world, is probably the greatest recognition and the greatest reward for his work. Other professors from the group: Dries Van Thourhout, Wim Bogaerts, Gunther Roelkens, Peter Bienstman, Geert Morthier, and Bart Kuyken were always helpful, whenever it was needed.

Bulk of the work on this thesis was carried out at Ghent University cleanroom facilities at Zwijnaarde, where I had a privilege to work with some wonderful people. Steven Verstuyft taught me all the secrets of cleanroom processing and provided continuous support and technical assistance throughout my work. Not only me, but virtually all PhD students of the Photonics Research Group in Ghent owe him a deepest gratitude for his vast knowledge, technical expertise, patient guidance and successful efforts in keeping our cleanroom running smoothly and efficiently. It was indeed such a rewarding experience for me to work with him. I am also thankful to Muhammad whose valuable suggestion improved my processing in the cleanroom. While working in the cleanroom, I also enjoyed help from Liesbet, an expert for our focus ion beam (FIB) and scanning electron microscope (SEM) systems, provided enormous help in numerous jobs that required use of these tools. My thanks also go to Jeroen Allaert, and Michael Vanslembrouck for technical support and assistance with measurement equipment and tools. Peter Guns was always there whenever I needed something to be made in the workshop. I would like to express my thanks to our administrative team in our group, Ilse Van Royen, Kristien De Meulder, Ilse Meersman, Mike Van Puyenbroeck, and Bert Coryn.

My office-mates, beginning with Alejandro, Sören, Rodica, Mahmoud, Xiaomin and Nicolas, thanks for a nice day-to-day working environment. Special thanks to Sören for translating my thesis summary (again and again). To Alejandro, Sören, Rodica, Mahmoud, Xiaomin, Nina, Sanja, Amin, Leila, Koen, Lukas, Alessio, Nayyera, Ali, Abdul, Antonio, Paul, Jing, Ana, Anton, Herbert, Ashim, Ananth, Alexandre, Paul, Jesper, Jing, John, Aditya, Alfonso, Chen, Andrew, Utsav, Sarvagya, Pijus, Alfonso, Bendix, Sam and all other colleagues, I would like to say thanks for the good memories I will keep of the positive working environment you create in Zwijnaarde and Technicum. But even more dear are the personal memories of the many occasions we had to spend time together without photonics on our minds.

One very big "thank you" is addressed to some of my countrymen whom I met during my life in Ghent and with whom I shared so many beautiful moments: Aditya-Kirti, Gaurav-Nikki, Utsav, Sarvagya, Manan-Nammi-Tashi, Ananth-Kamal-Reyansh, Christophe-Priyanka-Mira, Pawan-Neha-Prisha, Nikhil-Tripti-Ivan, Ratnesh-Akansha-Parv. Thanks for all the Diwali, Holi, new years and other celebrations we did.

I would also like to thank my current colleague at CommScope for their immense support: Jan, Cristina, Salvatore, Vivek, Stefano, Thierry, Danny, Walter, Ann, Heidi, Rudi. They warmly welcomed me in the group and have a wonderful working atmosphere. I would like to express my gratitude to Jan for always being there whenever I needed any guidance.

Lastly, I would like to thank my family for all their love and encouragement. Especially Sulakshna, with whom I have shared moments of deep anxiety but also of big excitement. I couldn't have made it without your continuous support and thank you for always being there for me. Her presence was very important in a process that is often felt as tremendously solitaire.

Ghent, April 2013-June 2018  
Kumar Saurav

# Table of Contents

<b>LIST OF FIGURES .....</b>	<b>I</b>
<b>LIST OF TABLES .....</b>	<b>IX</b>
<b>LIST OF ABBREVIATIONS.....</b>	<b>X</b>
<b>NEDERLANDSTALIGE SAMENVATTING.....</b>	<b>XIII</b>
<b>ENGLISH SUMMARY .....</b>	<b>XIX</b>
<b>1 OPTICAL CAVITY ENHANCED LABEL-FREE DETECTION.....</b>	<b>1</b>
<b>1.1 Introduction .....</b>	<b>2</b>
<b>1.2 Important aspects and parameters in biosensor development .....</b>	<b>4</b>
<b>1.3 Label-free biosensor .....</b>	<b>5</b>
1.3.1 Surface Plasmon resonance (SPR) biosensors .....	5
1.3.2 Ring resonator sensors .....	6
1.3.3 Interferometric waveguide sensors.....	7
1.3.4 1D photonic crystal grating based sensors .....	8
1.3.5 Photonic crystal cavity based sensors .....	9
<b>1.4 State of the art on refractive index sensing .....</b>	<b>11</b>
1.4.1 Bulk RI Sensing .....	12
1.4.2 Biological macromolecule sensing.....	13
1.4.3 Particle Sensing.....	14
<b>1.5 Thesis Organization .....</b>	<b>16</b>
<b>1.6 Publications.....</b>	<b>17</b>

<b>International Journals</b> .....	<b>17</b>
<b>International Conferences</b> .....	<b>18</b>
<b>References</b> .....	<b>18</b>
<b>2 PLANAR PHOTONIC CRYSTAL CAVITIES</b> .....	<b>25</b>
<b>2.1 Classification of PhC structures</b> .....	<b>26</b>
<b>2.2 Band diagram and photonic bandgap</b> .....	<b>28</b>
<b>2.3 Planar photonic crystal</b> .....	<b>29</b>
<b>2.4 Photonic Crystal Waveguides</b> .....	<b>31</b>
<b>2.5 Planar photonic crystal Cavities</b> .....	<b>32</b>
2.5.1 L3 based PhC cavities .....	35
2.5.2 Hollow core based PhC cavities .....	37
<b>2.6 Conclusions</b> .....	<b>39</b>
<b>References</b> .....	<b>39</b>
<b>3 WAFER SCALE FABRICATION OF PHC CAVITIES</b> .....	<b>43</b>
<b>3.1 Silicon-On-Insulator platform</b> .....	<b>44</b>
<b>3.2 Fabrication of 2D photonic crystal slabs</b> .....	<b>45</b>
3.2.1 Anisotropic etching of silicon substrate .....	48
3.2.1 Lapping and polishing of silicon substrate .....	50
3.2.2 Masking materials .....	52
3.2.3 Mask layer opening using photolithography .....	52
3.2.4 Fabrication of Spot size converters .....	55
3.2.5 Isotropic etch of silicon dioxide layer .....	57
<b>3.3 Fabrication of nano-fiber tip</b> .....	<b>61</b>
<b>3.4 Conclusion</b> .....	<b>63</b>
<b>Reference</b> .....	<b>64</b>

**4 DEVELOPMENT OF AN ADVANCED OPTICAL SET-UP FOR CHARACTERIZING PhC CAVITIES ..... 67**

**4.1 Overview and general considerations .....68**  
4.1.1 End-fire path .....69  
4.1.2 Visible imaging path .....69  
4.1.3 Infrared imaging path.....70

**4.2 Spectral characterization of different types of PhC cavities.....71**  
4.2.1 L3 based PhC cavities .....71  
4.2.2 Hollow core PhC cavities.....73

**4.3 Technique to spatially characterize the interaction volume of PhC cavities. ....74**

**4.4 Experimental determination of the sizing capabilities of the PhC cavity.....78**

**4.5 Investigation of mode volume of PhC cavity using nano-tip .....80**

**4.6 Conclusion .....80**

**References .....81**

**5 INVESTIGATION OF THE INTRINSIC DETECTION LIMIT OF PHOTONIC CRYSTAL CAVITIES ..... 83**

**5.1 Introduction .....84**

**5.2 Experiment.....85**

**5.3 Cavity spectral noise .....88**

**5.4 Fundamental thermorefractive noise.....91**

**5.5 Ultimate detection limit.....93**

**5.6 Conclusion .....96**

**References .....97**

<b>6 CONCLUSIONS AND PERSPECTIVES.....</b>	<b>101</b>
<b>6.1 Conclusions .....</b>	<b>101</b>
<b>6.2 Perspectives .....</b>	<b>103</b>

# List of Figures

- Figuur 1:** SEM-afbeelding van een vrijstaande fotonische kristalcaviteitreeks zonder substraat. Bijgevoegde afbeelding toont een zoom-in van de caviteit..... XIV
- Figuur 2:** Transmissiespectra van een fotonische kristalcaviteit (a) met substraat en (b) zonder substraat. Bijgevoegde afbeelding toont het intensiteitspatroon van het caviteitsveld bij resonantie. De rode schaal komt overeen met 1.5  $\mu\text{m}$ . ..... XV
- Figuur 3:** Gemeten mapping van de intensiteitsvariatie geïnduceerd door de interactie tussen de nanovezeltip en de L3 caviteit in verstrooiingsmode. .... XVI
- Figuur 4:** Ruis-sigitaalverhouding  $\Delta U/U$  van de fotospanning  $U$  geïnduceerd door het stralingsveld van de fotonische kristalcaviteit versus belastingsweerstand  $R_{\text{load}}$  van de fotodetector, en de overeenkomstige acquisitietijd  $t_{\text{acq}}$  voor een pomp detuning  $x=0$  (donkere punten) en  $x=0.29$  (blauwe punten). De foutbalken komen overeen met de standaardafwijking van tien herhaalde metingen. De zwarte en blauwe stippellijnen komen overeen met de ruislimiet van de oscilloscoop voor respectievelijk  $x=0$  en  $x=0.29$ . Het gecapteerd vermogen gemeten bij resonantie met  $R_{\text{load}}=1\text{M}\Omega$  voor  $x=0$  en  $x=0.29$  zijn respectievelijk 8 $\mu\text{W}$  en 6 $\mu\text{W}$ . Parse datapunten: ruis-sigitaalverhouding zonder fotonische kristalcaviteit tussen de laserbron en de fotodetector voor hetzelfde gecapteerd vermogen, als in het geval van  $x=0$ . Het grijze gebied verwijst naar een regime gelimiteerd door fundamentele thermo-optische ruis. .... XVII
- Figure 1:** SEM image of a free-standing substrate-less photonics crystal cavity array (Inset shows the zoomed in image of the cavity)..... XX
- Figure 2:** Transmission spectra of suspended photonic crystal cavity (a) with substrate and (b) without substrate, respectively, (Inset) Intensity pattern of the cavity field at resonance; the red scale of the image corresponds to 1.5  $\mu\text{m}$ . .... XXII

**Figure 3:** Measured map of the intensity variation induced by the interaction between the nano-tip fiber and the L3 cavity in Scattering mode. .... XXIII

**Figure 4:** Noise-to-signal ratio  $\delta U/U$  of the photovoltage  $U$  induced by the radiated field from the PhC cavity versus the load resistance  $R_{load}$  of the photodetector, and the corresponding acquisition sampling time  $t_{acq}$  for pump frequency detunings of  $x = 0$  (dark points) and  $x = 0.29$  (blue points). The error bars correspond to the standard deviation of ten repeated measurements. The black and blue dashed lines correspond to the noise limit imposed by the oscilloscope for  $x = 0$  and  $x = 0.29$ , respectively. The collected powers measured at resonance with  $R_{load} = 1 \text{ M}\Omega$  for  $x = 0$  and  $x = 0.29$  are  $8 \text{ }\mu\text{W}$  and  $6 \text{ }\mu\text{W}$ , respectively. Purple data points: noise-to-signal ratio without any PhC cavity between the laser source and the photodetector for the same collected power, as in the case of  $x = 0$ . The gray area corresponds to a regime limited by the fundamental thermo-optic noise. .... XXIII

**Figure 1.1:** In labelled biosensing, the target molecules bind to receptor molecules on a substrate so they become immobilised. After that, marker molecules bind to another site of the target molecules. Excess marker molecules are removed and the substrate is illuminated. The intensity of the light is then measured, providing information on the target molecule concentration. .... 2

**Figure 1.2:** A transducer is coated with receptor molecules. When target molecules bind to these receptor molecules, the physical properties of the analyte generate an altered state of the transducer which translates into a measurable signal. .... 3

**Figure 1.3:** Schematic of SPR sensing method. Surface plasmon resonance (SPR) detects changes in the refractive index in the immediate vicinity of the surface layer of a sensor chip. SPR is observed as a sharp shadow in the reflected light from the surface at an angle that is dependent on the mass of material at the surface. The SPR angle shifts when biomolecules bind to the surface and change the mass of the surface layer. .... 6

**Figure 1.4:** Schematic overview of a ring resonator sensor, in which RI changes are measured as a change in transmission wavelength, as the light coupled from the input waveguide to the circular waveguide changes,

because of the change in the resonant wavelength of the circular waveguide..... 7

**Figure 1.5:** Illustration of a MZI sensor..... 8

**Figure 1.6:** Overall mechanism of biosensing using PhC grating. (a) An example of the 1-D PC slab surface. (b) Corresponding resonance peak wavelength for this PC slab. (c) Functionalization of the slab surface and biological binding event via antigen–antibody interaction. (d) Peak wavelength shift as a result of this interaction. Reproduced from [20]... 9

**Figure 1.7:** Schematic overview of a photonic crystal based sensor, where binding of an analyte to the antibody results in a shift in transmission wavelength..... 10

**Figure 2.1:** SEM images of one-, two-, and three-dimensional PhCs. (a) 1D: Bragg mirror reproduced from [1], (b) 2D: Microstructured fiber reproduced from [2], (c) 3D: Yablonovite structure reproduced from [3].  
..... 26

**Figure 2.2:** Planar photonic crystal waveguide fabricated in silicon membrane suspended in air, reproduced from [4]..... 27

**Figure 2.3:** (a) Band folding in a periodic ‘empty’ lattice. (b) bandgap is formed when the refractive index contrast is introduced..... 28

**Figure 2.4:** Guided mode dispersion of TE modes in a dielectric slab. . 30

**Figure 2.5:** (a) Schematic of silicon based PhC structure with a triangular lattice (b) Dispersion diagram of silicon based planar PhC with the air and dielectric bands enclosing the bandgap. Shaded blue area represents the air-light cone..... 31

**Figure 2.6:** (a) Schematic of silicon based bulk PhC based W1 waveguide in triangular lattice (a) Dispersion diagram highlighting waveguide modes within a line defect photonic crystal..... 32

**Figure 2.7:** (a) Schematic of silicon based PhC cavity in triangular lattice (b) Dispersion diagram highlighting the discrete state formation in the bandgap which occurs due to creation of a small defect by reducing the hole radius. .... 33

**Figure 2.8:** SEM image of cavity fabricated using 193 nm immersion lithography: (a) standard L3 cavity, (b) L3 cavity based on Noda’s proposed design and (c) Savona’s proposed design. Red circle represents the hole which has been displaced..... 36

**Figure 2.9:** The layout of a PhC where a linear sub-wavelength-wide air slot is introduced in the center of the line defect and cavity is realized by

(a) increasing the slot width from (100 nm to 120 nm) at the center of PhC structure, (b) by a local line-defect-width modulation via transversally shifting holes away from the slot. Air holes colored red, yellow, and blue are shifted outward by 15 nm, 10 nm, and 5 nm, respectively. .... 38

**Figure 2.10:** Change in the slot waveguide mode dispersion upon increasing the slit width from 70 to 160 nm. .... 38

**Figure 3.1:** A full (220 nm) and shallow (70 nm) etch step is executed on the top silicon (device) layer using DUV lithography at imec. .... 44

**Figure 3.2:** Hole diameters and line widths as a function of lithography exposure dose. Markers: hexagonal lattices of holes, marked with design pitch and diameter. Lines: Lines marked with design line width. Reproduced from [4]. .... 46

**Figure 3.3:** Plot of deviation in fabrication of diameter and slot width of PhC compared to the designed ones. .... 47

**Figure 3.4:** Schematic of an integrated PhC cavity cross-section (a) highlighting the congestion of the high NA signal detection system and (b) of the microdroplet transportation system of the analytes. .... 48

**Figure 3.5:** Schematic of dry etching (left), isotropic wet etching (middle), and anisotropic etching (right) of Silicon. .... 49

**Figure 3.6:** Anisotropic etching of <100> silicon. .... 50

**Figure 3.7:** Schematic of process flow for fabrication of substrate-less free-standing PhC membrane. The top side of the chip was protected by placing the chip placed in a holder (see **Figure 3.8**). .... 51

**Figure 3.8:** Camera image of the holder (a) in which the chip is mounted for silicon substrate etch and (b) with a mounted chip inside. .... 53

**Figure 3.9:** Optical microscope image of local silicon substrate etched PhC array seen from (a) backside and (b) topside. .... 54

**Figure 3.10:** SEM image of the cross section of PhC cavity after removal of the silicon substrate. .... 54

**Figure 3.11:** SEM image of (a) Peeling of patterned SU8 waveguide observed after mechanical lapping. (b) Patterned SU8 waveguide after silicon substrate removal. (c) Zoomed in interface of SU8 waveguide and silicon wire waveguide. .... 56

**Figure 3.12:** Optical microscope image of the substrate-less chip dried (a) without CPD (b) with CPD. .... 58

<b>Figure 3.13:</b> SEM image of the substrate-less PhC array where some PhC membrane collapsed due to stress developed between top silicon and BOX layer. ....	59
<b>Figure 3.14:</b> Optical microscope image of the free-standing substrate-less PhC array. ....	59
<b>Figure 3.15:</b> SEM image of a free-standing substrate-less photonics crystal cavity array (Inset shows the zoomed in image of the cavity). ...	60
<b>Figure 3.16:</b> (a) White light interferometer image of substrate-less free-standing PhC cavities (b) Upward deflection of 320 nm was measured.	60
<b>Figure 3.17:</b> (a) Experimental setup for the characterize the PhC cavities. Transmission spectra of suspended PhC cavity (a) with substrate and (b) without substrate, respectively. (Inset) Intensity pattern of the cavity field at resonance; the red scale of the image corresponds to 1.5 $\mu\text{m}$ .....	61
<b>Figure 3.18:</b> Schematics of the meniscus etching process. The fiber at time zero (left), at time $\tau/2$ (middle) and at time $\tau$ (right). The meniscus formed at the liquid–liquid and liquid–solid interfaces lowers height, as the fiber radius decreases. When the fiber radius converges to zero at time $\tau$ , the final taper portion is created. ....	62
<b>Figure 3.19:</b> Setup for nano-fiber tip fabrication.....	62
<b>Figure 3.20:</b> SEM image of fabricated nano-fiber tip (a) without and (b) with vertical fiber movement.....	63
<b>Figure 4.1:</b> Schematic of the experimental apparatus illustrating the main functions. The PhC cavities are excited using a tunable laser diode, on the bottom left. The light scattered out of the plane by the photonic structure is collected in the IR imaging arm (red area). Blue LED illuminate the sample that is imaged on the CCD camera. ....	68
<b>Figure 4.2:</b> Visible camera image of PhC cavity (a) with substrate and (b) without substrate below. ....	70
<b>Figure 4.3:</b> Infrared path used for real-space imaging (Inset - intensity pattern of a cavity field at resonance captured by the IR camera).....	71
<b>Figure 4.4:</b> (a) Scanning Electron Micrograph image of a standard L3 cavity, (b) Transmission spectra of free standing L3 cavity, (Inset - intensity pattern of the cavity field at resonance). ....	72
<b>Figure 4.5:</b> (a) Scanning Electron Micrograph image of a modified L3 cavity, (b) Transmission spectra of free standing modified L3 cavity, (Inset - intensity pattern of the cavity field at resonance).....	73

**Figure 4.6:** (a) Scanning Electron Micrograph image of a standard L3 with slot cavity (slot width = 80 nm), (b) Transmission spectra of free standing L3 with slot cavity. .... 74

**Figure 4.7:** (a) Scanning Electron Micrograph image of a width modulated slot cavity, (b) Transmission spectra of free standing L3 with slot cavity (Inset: intensity pattern of the cavity field at resonance). .... 74

**Figure 4.8:** (a) Visible image of a PhC cavity array along with a nano-tip (by high NA microscope objective) fiber in the neighborhood. The highlighted PhC structure has fiber coupled at the input and the output, (b) Cavity excitation scheme,  $\lambda_0$  is the resonance and pump wavelength respectively. .... 75

**Figure 4.9:** Measured map of the intensity variation induced by the interaction between the nano-tip fiber and the L3 cavity in (a) Scattering mode, (b) transmission mode, (c) Simulated mode profile of a L3 cavity at the cavity surface (red and blue represents high and low intensity respectively), (d) variation of intensity at center of the cavity in y direction along red dotted line in scattering mode (extracted from (a)). .... 76

**Figure 4.10:** Superposition principle: Scattered intensity collected from the cavity surface due to the presence of the nano-tip at different axial positions normal to cavity surface is subtracted to calculate the impact of the resulting nano-object on collected intensity. .... 78

**Figure 4.11:** Measured map of the intensity variation induced by the interaction between the nano-tip fiber and the modified L3 cavity. .... 79

**Figure 4.12:** Measured intensity variation induced by the interaction between the nano-tip fiber and center of the modified L3 cavity along y direction at different axial position (z). .... 79

**Figure 4.13:** Comparison of the mapped mode volume between a standard L3 and modified L3. .... 80

**Figure 5.1** (a) Scanning electron micrograph of the top surface of an integrated L3 PhC cavity. The silicon oxide has been removed below the 215 nm thick free-standing slab. The blue arrows indicate the light path of the pump laser beam at a frequency  $\omega_p$ . (b) Experimental optical spectrum of the cavity (dark curve) with the corresponding Lorentzian fit (red dotted curve) whose cavity linewidth is  $\Delta\omega = \omega_0/3800$ . The resonant frequency  $\omega_0$  corresponds to a wavelength of 1599.3 nm. On the right: Time traces of the photovoltage induced by the collected scattered light  $I_{scat}$  for a  $x =$

0 (black trace) and  $x = 0.29$  (blue trace) frequency detuning. Each of the traces is made of 50,000 equidistant data points. .... 85

**Figure 5.2.** Noise-to-signal ratio  $\delta U/U$  of the photovoltage  $U$  induced by the radiated field from the PhC cavity versus the load resistance  $R_{load}$  of the photodetector, and the corresponding acquisition sampling time  $t_{acq}$  for pump frequency detuning of  $x = 0$  (dark points) and  $x = 0.29$  (blue points). The error bars correspond to the standard deviation of ten repeated measurements. The black and blue dashed lines correspond to the noise limit imposed by the oscilloscope for  $x = 0$  and  $x = 0.29$ , respectively. The collected powers measured at resonance with  $R_{load} = 1 \text{ M}\Omega$  for  $x = 0$  and  $x = 0.29$  are  $8 \text{ }\mu\text{W}$  and  $6 \text{ }\mu\text{W}$ , respectively. Purple data points: noise-to-signal ratio without any PhC cavity between the laser source and the photodetector for the same collected power, as in the case of  $x = 0$ . The gray area corresponds to a regime limited by the fundamental thermo-optic noise..... 87

**Figure 5.3** (a) and (b) Optical spectra of L3 PhC cavities with  $Q = 2200$  and  $Q = 16800$ , respectively. The red dotted lines are Lorentzian fits. (c) and (d) Near-infrared optical images of the resonant field radiated from the  $Q = 2200$  and  $Q = 16800$  PhC cavities, respectively. (e) Noise-to-signal ratio  $\delta U/\Delta U$  of the photo voltage  $U$  versus the quality factor for  $x = 0$  (black dashed line) and  $x = 0.29$  (blue dashed line) with a load resistance of  $R_{load} = 119 \text{ k}\Omega$ . Black and blue dashed lines are expected variations with the effective mode volume of the  $Q = 3800$  cavity. The blue dotted line is the expected variation with the effective mode volume of the  $Q = 16800$  cavity. The collected power at  $x = 0$  is  $0.17 \text{ }\mu\text{W}$ ..... 90

**Figure 5.4:** (a) Square and circle symbols are the minimum relative frequency shift that can be detected versus the load resistance  $R_{load}$ , and the corresponding acquisition time  $t_{acq}$  for three different quality factors  $Q$  with the same input power and the same frequency detuning  $x = 0.29$ . The purple, blue, and red dashed lines are oscilloscope noise limits for the powers of  $15$ ,  $6$ , and  $1.25 \text{ }\mu\text{W}$  that are collected with  $R_{load} = 1 \text{ M}\Omega$  for each cavity, respectively. Dark dot-dashed line is the oscilloscope noise for an optimal light collection. The purple dot-dashed line pinpoints the saturation level due to the thermal and mechanical noise for  $Q = 2200$ . (b) Minimum relative frequency shift normalized to the quality factor for two load resistances pinpointed by the black and blue arrows in (a). The red dashed line and dotted line are the fundamental thermal noise limits

associated with a fundamental mode volume of  $V_{\text{eff}} = 0.060 \mu\text{m}^3$  (i.e., for  $Q = 2200$  and  $Q = 3800$ ) and  $V_{\text{eff}} = 0.126 \mu\text{m}^3$  (i.e., for  $Q = 16800$ ), respectively..... 92

**Figure 5.5:** Relative frequency shift  $\delta\omega/\Delta\omega|T$  induced by the fundamental thermal noise normalized to  $Q/V_{\text{eff}}$  versus the effective cavity mode volume  $V_{\text{eff}}$ . This quantity is proportional to the minimal nanoparticle volume that the sensor can detect when the fundamental thermal noise limit is reached. The arrow pinpoints the value for the standard L3 PhC cavity.  $V_{\text{eff}}$  is normalized to  $(\lambda/n_{\text{Si}})^3$  where  $n_{\text{Si}}$  is the index of the silicon material and the wavelength  $\lambda = 1.6 \mu\text{m}$ ..... 93

# List of Tables

<b>Table 1.1:</b> Reported figure of merit (F) of different microcavities. .....	11
<b>Table 1.2:</b> Reported bulk RI sensitivities of different 2D PhC structures. ....	12
<b>Table 1.3:</b> Reported detection limits and dynamic range for sensing biomolecules and particles using 2D PhCs in three different assay modes. ....	15



# List of Abbreviations

<b>ALD</b>	Atomic layer deposition
<b>BHF</b>	Buffered-Hydrofluoric
<b>CMOS</b>	Complementary metal-oxide-semiconductor
<b>CPD</b>	Critical point drying
<b>DL</b>	Detection limit
<b>FIB</b>	Focus ion beam
<b>FLOWER</b>	Frequency locked optical whispering evanescent resonator
<b>FWHM</b>	Full-width at half-maximum
<b>IC</b>	Integrated circuits
<b>IPA</b>	Isopropyl alcohol
<b>LED</b>	Light emitting diode
<b>LPCVD</b>	Low pressure chemical vapor deposition
<b>MPW</b>	Multi-project-wafer
<b>MZI</b>	Mach- Zehnder interferometer
<b>NA</b>	Numerical aperture
<b>NSOM</b>	Near-field scanning optical microscopy
<b>PBG</b>	Photonic band gap
<b>PEB</b>	Post exposure bake
<b>PECVD</b>	Plasma enhanced chemical vapor deposition

<b>PhC</b>	Photonic crystal
<b>PIC</b>	Photonic integrated circuit
<b>RF</b>	Radio frequency
<b>RI</b>	Refractive index
<b>RIE</b>	Reactive Ion Etching
<b>RIN</b>	Relative intensity noise
<b>RIU</b>	Refractive index units
<b>SEM</b>	Scanning electron microscope
<b>SNOM</b>	Scanning Near-field Optical Microscopy
<b>SOI</b>	Silicon-on-insulator
<b>SPR</b>	Surface Plasmon resonance
<b>TE</b>	Transverse-Electric
<b>TIR</b>	Total internal reflection
<b>TM</b>	Transverse magnetic
<b>VCSEL</b>	Vertical cavity surface emitting laser
<b>WG</b>	Whispering gallery

# Nederlandstalige samenvatting

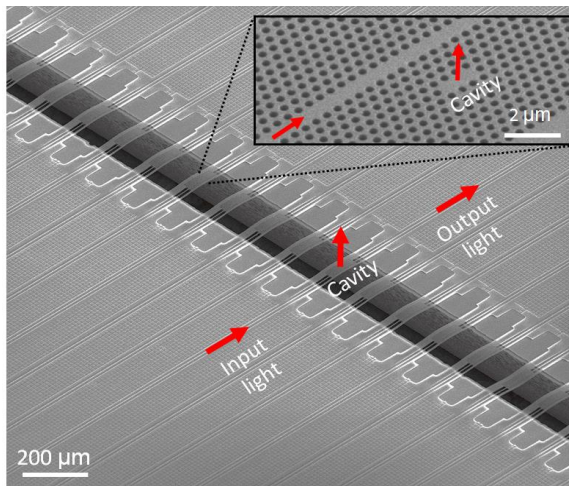
De markt van biosensoren wordt gedreven door de toenemende vraag naar snelle analyse-instrumenten om biomoleculaire interacties te meten en de aanwezigheid van pathogenen of andere gevaarlijke substanties te detecteren. De rol van biosensoren is erg belangrijk in de medische wetenschap en nuttig voor de vroege detectie van humaan interleukine-10 (dat hartziekten veroorzaakt) en het humaan papilloma-virus. Zulke biosensoren kunnen pathogenen detecteren bij concentraties die een minimum aan fysiologische risico's met zich meebrengen. Om ziekteverspreiding te voorkomen is detectie van dergelijke pathogenen in een vroeg stadium daarom van cruciaal belang. Labelvrije detectie heeft een significant voordeel om dit doel te bereiken. Hierbij worden doelmoleculen niet gelabeld of gewijzigd maar gedetecteerd in hun natuurlijke vorm, wat het detectieproces op zich relatief gemakkelijk en goedkoop maakt. Een labelvrije sensor kan elektrisch, mechanisch of fotonisch zijn. In dit werk leggen we de nadruk op fotonische sensoren, met een bijzondere focus op brekingsindex-gebaseerde sensoren. Zulke sensoren zijn veelbelovend voor gevoelige, labelvrije platformen voor de detectie van pathogenen (of andere analyten).

Fotonisch geïntegreerde circuits combineren en miniaturiseren optische functies als laserbronnen, filters en fotodetectoren op chips. Zulke fotonische chips kan men fabriceren met nanoschaal afmetingen en zonder extra instrumentontwikkelingskosten omdat men gebruik maakt van complementaire metaal-oxide-halfgeleider (CMOS)-technologie. Op die manier kan een lagekosten lab-on-a-chip detectie-instrument ontwikkeld worden. Onder de verschillende fotonische sensoren, blijken planaire fotonische kristalcaviteiten het meeste potentieel te hebben om lage concentraties te detecteren. Niettemin hebben zulke sensoren hun ultieme capaciteit nog niet bereikt. Het belangrijkste doel van dit werk was om de ultieme detectie-eigenschappen van 2D fotonische kristalcaviteiten te onderzoeken. Dit heeft mede de ontwikkeling van een specifiek fabricageproces en toegewijde karakterisatie-opstelling gevestigd.

Fotonische kristallen zijn structuren die gedefinieerd worden door een periodieke modulatie van de brekingsindex van dezelfde grootte-orde als de golflengte van het licht dat met de structuren interageert. Wanneer een elektromagnetische golf invalt op een 1D, 2D of 3D periodieke structuur, wordt de golf gedeeltelijk verstrooid op elke diëlektrische interface. De superpositie van dergelijke verstrooiingen leidt tot een interval van elektromagnetische frequenties waarvoor

lichtpropagatie onmogelijk wordt in een of meerdere richtingen. Een dergelijk frequentie-interval wordt een fotonische bandkloof genoemd. Het bestaan van een

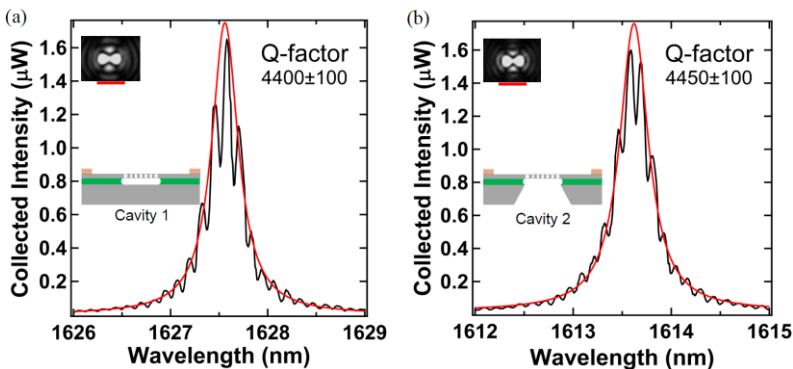
fotonische bandkloof geeft aanleiding tot een aantal interessante en nuttige eigenschappen, onder meer de lokalisatie van licht bij defecten en op oppervlakken en het voorkomen van radiatie. Door omzichtig ontwerp van de fotonische kristal geometrie, kan men optische caviteiten met zeer scherpe resonanties realiseren. De infiltratie van een pathogeen analyt binnenin zulke defecten leidt tot een verschuiving van de optische resonantiefrequentie. Een dergelijke verschuiving kan getraceerd worden door de afname in de transmissie bij de resonantiefrequentie te monitoren van het caviteitsspectrum.



**Figuur 1:** SEM-afbeelding van een vrijstaande fotonische kristalcaviteitreeks zonder substraat. Bijgevoegde afbeelding toont een zoom-in van de caviteit.

Fotonische kristalcaviteiten zijn afgelopen jaren veelvuldig onderzocht in hun toepassing voor biodetectie omwille van hun hoge kwaliteitsfactor (Q-factor) en laag modevolume (V). Een hoge Q en laag V laat versterkte licht-materie interacties in het caviteitsmodevolume toe en kan in principe aanleiding geven tot snelle labelvrije detectie met hoge gevoeligheid. In het bijzonder zijn fotonische kristalcaviteiten die gedefinieerd zijn in dunne silicium membranen interessant omwille van hun ultrahoge Q-factor, laag V, gemak tot interactie met golfgeleiders en kleine voetafdruk. Zulke voordelen maken fotonische kristalcaviteiten de perfecte kandidaat voor toepassingen als nanoschaal brekingsindexsensoren en voor een verscheidenheid aan biodetectie-toepassingen als accurate diagnosetool, drugsopsporing, toxiciteitsmetingen, enkelvoudige moleculedetectie, ...

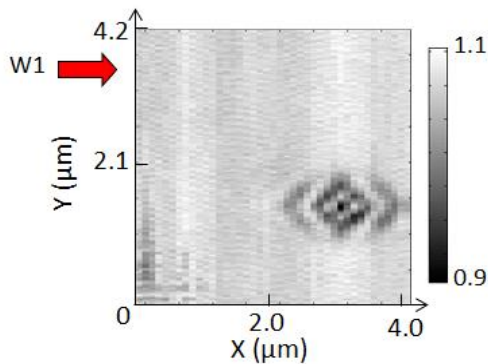
De meest gebruikte methode om fotonische kristalsensoren te fabriceren is e-beam lithografie. Dit is omwille van zijn veelzijdigheid in prototyping. Het is echter geen geschikte methode voor massaproductie. In deze thesis hebben we de fabricage van fotonische kristalcaviteiten onderzocht op een silicium-op-isolator (SOI) platform waarbij gebruik gemaakt wordt van diepe UV lithografie. De chips werden gefabriceerd bij imec, welke beschikt over commercieel distributie-mogelijkheden. We wijzen er ook op dat niet alle fotonische kristalstructuren die kunnen gerealiseerd worden via e-beam lithografie ook via diepe UV lithografie gefabriceerd kunnen worden. Daarom hebben we ons beperkt tot structuren die wel geschikt zijn voor fabricage door middel van diepe UV lithografie. In DUV lithografie verkleint de breedte van de silicium golfgeleider met toenemende belichtingsdosis en neemt de diameter van de gaten van de fotonische kristallen toe. Om beide structuren op target te fabriceren moet men daarom een bias toepassen op het masker. We bespreken de gebruikte bias-tabel voor fabricage van de fotonische kristalstructuren bij de gewenste golflengte.



**Figuur 2:** Transmissiespectra van een fotonische kristalcaviteit (a) met substraat en (b) zonder substraat. Bijgevoegde afbeelding toont het intensiteitspatroon van het caviteitsveld bij resonantie. De rode schaal komt overeen met 1.5  $\mu\text{m}$ .

Een verlaging van het detectievolume  $V$  van de fotonische kristalcaviteit bemoeilijkt de transport van analyten met standaard geïntegreerde microfluidische kanalen omwille van het verdwijnen van de vloeistofsnelheid bij de kanaalwanden. Afhankelijk van de concentratie van de analyten, varieert de tijd die de analyten nodig hebben om te diffunderen van de bulk oplossing tot het sensoroppervlak van dagen tot zelfs jaren. Dit massatransport vertraagt de detectiesnelheid in grote mate. Daarom is er een nood aan sensorarchitecturen bij dewelke het transport van de analyten op een meer effectieve wijze kan worden gedaan.

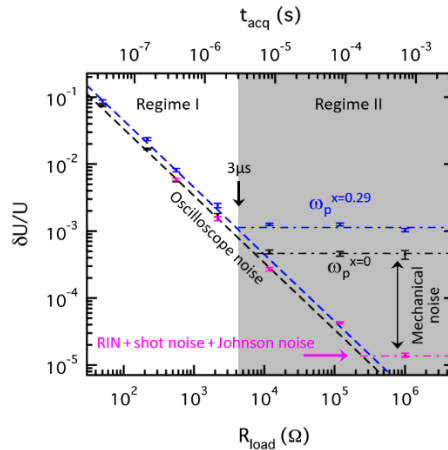
Een mogelijke oplossing is om de analyten in kleine hoeveelheden te transporteren naar het caviteitsoppervlak met beschikbare afgiftetechnieken, zoals bijvoorbeeld micropipetering of druppelbevlekking. Fotonische kristallen met vrije toegang van beide zijden hebben als voordeel hun gemak tot transport van de analyten en de simultane detectie van signaalvariaties geïnduceerd door de analyten. Ook kan een fotodetector geïntegreerd worden aan een zijde van de fotonische kristalcaviteit waarbij het transport van de analyten plaatsvindt aan de andere zijde van de caviteit. Om vrije toegang te krijgen tot beide zijden van de caviteit moet het substraat onder de caviteit lokaal verwijderd worden. Merk op dat biomoleculen zich over het algemeen in een waterige omgeving bevinden, wat maakt dat de Q-factor drastisch gereduceerd wordt omwille van lichtabsorptie. Dit effect kan men echter minimaliseren door de voorgestelde aanpak die gebruik maakt van lokaal transport.



**Figuur 3:** Gemeten mapping van de intensiteitsvariatie geïnduceerd door de interactie tussen de nanovezel tip en de L3 caviteit in verstrooiingsmode.

In deze doctoraatssthesis introduceren we een fabricageproces dat toelaat om het substraat lokaal te verwijderen onder een fotonisch kristal membraan zonder dat de toplaag met devices wordt aangetast. Dit proces leidt tot een reeks van gefabriceerde silicium-gebaseerde fotonische kristalcaviteiten zonder substraat met een venstergrootte van 3.5 mm bij 50  $\mu\text{m}$ . Zo'n reeks kan meer dan 150 fotonische kristalcaviteiten bevatten, waarbij elke caviteit gekoppeld wordt met een andere toegangsgolfguide. Dit maakt het zeer compatibel voor biologische detectie op grote schaal. Het geeft ook de mogelijkheid tot implementatie van verschillende types caviteitsontwerp met een verscheidenheid aan beoogde toepassingen. Alhoewel we het proces voor fabricage zonder substraat voorstellen op chipniveau kan dit zonder meer worden uitgebreid naar waferschaalniveau. Belangrijk hierbij is dat de toplaag (met devices) geen nood heeft aan een

specifiek maskermateriaal, wat maakt dat hetzelfde proces gebruikt kan worden voor eender welke toplaag (zoals bijvoorbeeld III-V, siliciumnitride of polymeren) en voor actieve devices. **Figuur 1** toont een rasterelektronenmicroscop-afbeelding van een vrijstaande fotonische kristalcaviteitreeks.



**Figuur 4:** Ruis-sigtaalverhouding  $\delta U/U$  van de fotospanning  $U$  geïnduceerd door het stralingsveld van de fotonische kristalcaviteit versus belastingsweerstand  $R_{load}$  van de fotodetector, en de overeenkomstige acquisitietijd  $t_{acq}$  voor een pomp detuning  $x=0$  (donkere punten) en  $x=0.29$  (blauwe punten). De foutbalken komen overeen met de standaardafwijking van tien herhaalde metingen. De zwarte en blauwe stippellijnen komen overeen met de ruislimiet van de oscilloscoop voor respectievelijk  $x=0$  en  $x=0.29$ . Het gecaptureerd vermogen gemeten bij resonantie met  $R_{load}=1M\Omega$  voor  $x=0$  en  $x=0.29$  zijn respectievelijk  $8\mu W$  en  $6\mu W$ . Paarse datapunten: ruis-sigtaalverhouding zonder fotonische kristalcaviteit tussen de laserbron en de fotodetector voor hetzelfde gecaptureerd vermogen, als in het geval van  $x=0$ . Het grijze gebied verwijst naar een regime gelimiteerd door fundamentele thermo-optische ruis.

We tonen aan dat het voorgestelde proces compatibel is met de integratie van micrometergrootte SU8-gebaseerde polymeer golfgeleiders. Zulke polymeer golfgeleiders kunnen in combinatie met silicium-gebaseerde geïnverteerde tapers dienstdoen als spotgrootte-omzetter. We vergelijken experimenteel de transmissie-spectra van een vrijhangende fotonische kristalcaviteit met en zonder substraat. We tonen aan dat de Q-factor van beide caviteiten niet beïnvloed wordt door de talrijke processtappen, wat de devicearchitectuur een goede kandidaat maakt voor detectietoepassingen. **Figuur 2** toont de transmissie-spectra van vrijhangende fotonische kristalcaviteiten respectievelijk met en zonder substraat.

De bijgevoegde afbeelding toont het verstrooiingspatroon van het caviteitsveld bij resonantie.

Na devicefabricage hebben we de caviteiten gekarakteriseerd door een nanovezeltip te plaatsen in het nabije veld van de caviteit en tezelfdertijd de intensiteitsverdeling van de caviteitsmode te meten. Het positioneren van de nanotips met verschillende groottes liet toe om de spectrale gevoeligheid van de caviteit te bepalen. Dit is gebaseerd op het meten van de verstrooide intensiteitsvariatie van het geëxciteerde caviteitsoppervlak omwille van de aanwezigheid van de nanovezeltip in de nabijheid van het caviteitsoppervlak. **Figuur 3** toont de mapping van de interactie tussen de nanovezeltip en het caviteitsveld in verstrooiingsmode.

In deze thesis hebben we de detectielimiet van fotonische kristalcaviteiten voor detectietoepassingen bestudeerd. In het bijzonder hebben we het compromis bepaald tussen detectielimiet en meetsnelheid. Zoals weergegeven in **Figuur 4**, belangrijk is dat we een regime gevonden hebben waar de thermische fluctuaties de intrinsieke detectielimiet bepalen voor de meettijd  $t_{acq}$  die groter is dan  $3 \mu s$ . Een dergelijke fundamentele limiet komt overeen met een frequentieverschuiving van  $1/2000$  van de lijnbreedte van de caviteitsresonantie voor een effectief modevolume van  $0.06 \mu m^3$ . De resultaten van het onderzoek geven aan dat het mogelijk is om tot 33 miljoen deeltjes per seconde met een grootte tot 34 nm te monitoren. Dit maakt de techniek uitermate geschikt voor snelle nanodeeltjes- en biodetectie in reële tijd.

# English summary

The market of biosensor is driven by increasing demand for rapid analysis tools to measure biomolecular interactions and detect the presence of pathogens or other harmful substances. The role of biosensors in medical science including early stage detection of human interleukin-10 causing heart diseases, rapid detection of human papilloma virus, etc. are important aspects. Such biosensors can detect pathogens at concentrations at or below the lowest levels that yield physiological risk. Therefore, early detection of these pathogens is crucial for preventing the spread of disease. Label-free sensing provides a significant advantage in achieving this goal. In the label-free detection, target molecules are not labeled or altered, and are detected in their natural forms which makes the detection relatively easy and cheap to perform. This kind of sensor can be of electric, mechanic or photonic nature. In this work, we will focus on photonic sensors, in particular on refractive index based sensors. These sensors have shown promise for sensitive, label-free platforms for pathogen (or any other analyte) detection.

Photonic integrated circuits combine and miniaturize optical functions such as laser sources, filters and detectors, on chips. These photonic chips can be fabricated with nanoscale features and with no extra equipment development cost since they use complementary metal-oxide-semiconductor (CMOS) processing technology. As a result, low-cost lab-on-a-chip sensing tool can be developed. Among different photonic sensors, planar photonic crystal cavities, have shown the potential to achieve low concentration detection capabilities. However, the ultimate capability of such sensors has not been reached yet. The main objective of this work was to investigate the ultimate sensing properties of 2D photonic crystal cavities. It has required the development of dedicated fabrication process and dedicated characterization set-up.

Photonic crystals are photonic structures characterized by a periodic modulation of the refractive index that is of the same order of magnitude as the wavelength of the light that interacts with them. When an electromagnetic is incident on a 1D, 2D or 3D periodic structures, it undergoes partial scattering at each dielectric interface. The resulting multiple scattering phenomenon gives rise to a range of electromagnetic frequencies for which light propagation is prohibited in one or several directions. Such a frequency range is called photonic bandgap. The existence of photonic band gap gives rise to a number of interesting and useful

properties including the localization of light at defects and surfaces and the inhibition of radiation. By carefully designing the geometry of the photonic crystal patterned defects, optical cavities with sharp resonances can be realized. The infiltration of any pathogenic analyte within such defects causes a shift in optical resonance. This shift can be tracked by monitoring the decrease in transmission at the resonance frequency from the cavity spectrum.

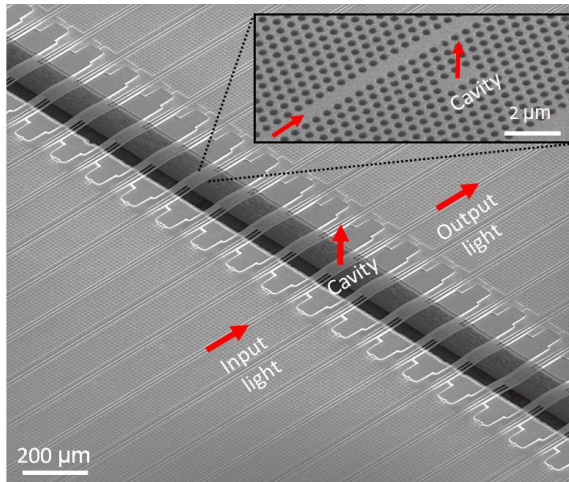


**Figure 1:** SEM image of a free-standing substrate-less photonic crystal cavity array (Inset shows the zoomed in image of the cavity).

Photonic crystal cavities have been intensively investigated in recent years for biosensing applications due to their high quality (Q) factor and low mode volume (V). High Q factor and low V enables enhanced light-matter interactions in the cavity mode volume and can in principle provide fast label-free detection with high sensitivity. In particular, photonic crystal cavities patterned in thin membrane of silicon benefit from ultra-high Q factor, low V, convenience in integration with waveguides, small footprint. With such assets, these cavities are potential candidates as nanoscale refractive sensors (RI) for various biosensing applications such as accurate diagnosis, drug discovery, toxicity issues, single molecule detection, etc.

The most common method used for fabricating photonic crystals sensor is electron beam (e-beam) lithography. This is due to its versatility in the prototyping process but they are not a suitable tool for mass production. In this thesis, we have investigated fabrication of photonic crystal cavities on Silicon-on-Insulator technological platform using deep ultraviolet (DUV) lithography at imec that can produce chips at commercial distribution scales. We point out that not all the photonic crystal structures realized using e-beam lithography can be fabricated

using DUV lithography and hence we also investigated various suitable photonic crystal cavity structures in this regard. In DUV lithography, with increasing exposure dose, the lines (width of the silicon waveguide) shrink and diameter of the holes grow. Therefore, to pattern both the structures together on target, a bias must be applied to one or the other on the mask. We present the bias chart needed for the fabrication of the photonic crystal structures which operates in desired wavelength and have dimensions similar to that of designed ones.

Decreasing the sensing volume  $V$  of the photonic crystal cavity, challenges the transportation of analytes with standard integrated microfluidic channels as the velocity of fluid vanishes at the channel wall. Depending on the concentration of the analytes, the time that these analytes require to diffuse from the bulk solution to the sensor surface can vary from days to even years till the total flux of the analytes gets transported on the surface of the sensor. This mass transportation problem significantly slows down the detection speed. As a result, there is a need for sensor architectures in which the transportation of analytes to the sensor surface can be done more effectively.

One of the possible solution is to transport the analytes in small amounts toward the cavity surface with available dispensing techniques, e.g., micropipetting or droplet spotting. photonic crystal cavities with a free access from both sides benefit from ease in the transportation of analytes and simultaneous detection of signal variation induced by the analytes. Moreover, the photodetector can be integrated on one side of the photonic crystal cavity while the analytes transportation can be carried out from the other side. In order to have a free accessibility from both the sides of the cavity, the substrate below the cavity needs however to be removed locally. Note that in general, biomolecules are in aqueous environment, which can drastically reduce the  $Q$  factor of the cavity due to light absorption. Such a detrimental effect can be advantageously minimized by the proposed local transportation approach.

In this PhD thesis, we introduce a fabrication process flow that allows us to locally remove the substrate below photonic crystal membrane without jeopardizing the top device layer. This process yields an array of fabricated silicon based photonic crystal cavities free of substrate with a window size as large as  $3.5 \text{ mm} \times 50 \text{ }\mu\text{m}$ . This array can contain more than 150 photonic crystal cavities, each coupled to different access waveguides which is compatible with a large scale biological sensing. It offers the opportunity for the implementation of various types of cavity design that targets different dedicated applications. Although we present the process for substrate-less fabrication at the chip level, it can conveniently be transposed at a wafer scale. Importantly, the top layer (device) does not need any kind of masking material, which means that the same process flow can be used

for any kind of top layer (e.g., III–V, silicon nitride, polymer), as well as for various active devices. **Figure 1** shows the scanning electron micrograph of a substrate-less free-standing suspended photonic crystal cavity array.

We show that the proposed process is compatible with the integration of micrometer-sized SU8-based polymer waveguides. These polymer waveguides, together with high index contrast adiabatic nanometer-sized silicon inverted tapers, act as spot size converters. We experimentally compare the transmission spectra of air-suspended photonic crystal cavity with and without substrate. We show that the Q factor of both cavities remain unaffected despite of the various processing steps, which makes our device architecture a good candidate for sensing applications. **Figure 2** shows the transmission spectra of suspended photonic crystal cavity with substrate and without substrate, respectively. The inset displays the scattered intensity pattern of the cavity field at resonance.

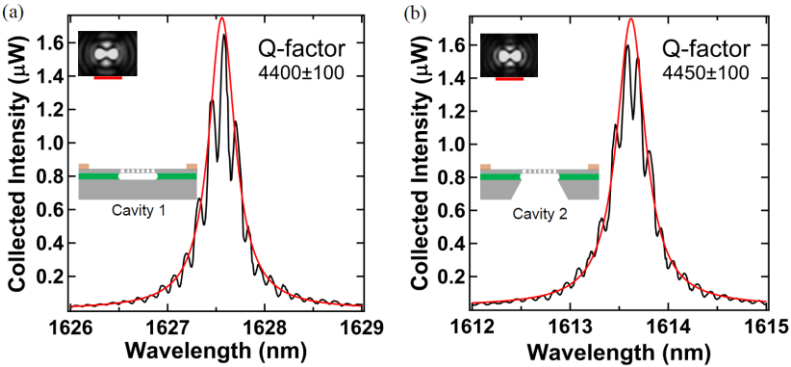


**Figure 2:** Transmission spectra of suspended photonic crystal cavity (a) with substrate and (b) without substrate, respectively, (Inset) Intensity pattern of the cavity field at resonance; the red scale of the image corresponds to 1.5  $\mu\text{m}$ .

After fabrication of these devices, we spatially probed such cavities by positioning a nano-fiber tip in the near field of the cavity and simultaneously measuring the intensity distribution of the cavity mode. The positioning of nano-tips of various apex sizes allowed us to determine the spectral sensitivity of the cavity. This investigation relies on measuring the scattered intensity variation from the excited cavity surface due to the presence of the nano-tip near cavity surface. **Figure 3** shows the map of the interaction between the nano-fiber tip and the cavity field in scattering mode.

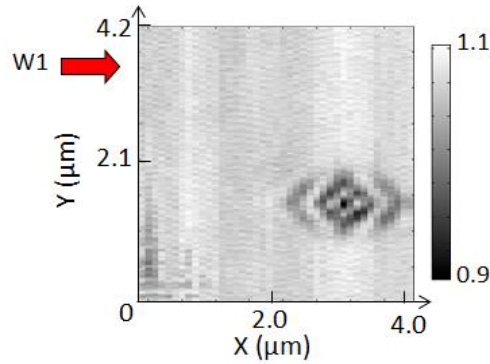


**Figure 3:** Measured map of the intensity variation induced by the interaction between the nano-tip fiber and the L3 cavity in Scattering mode.

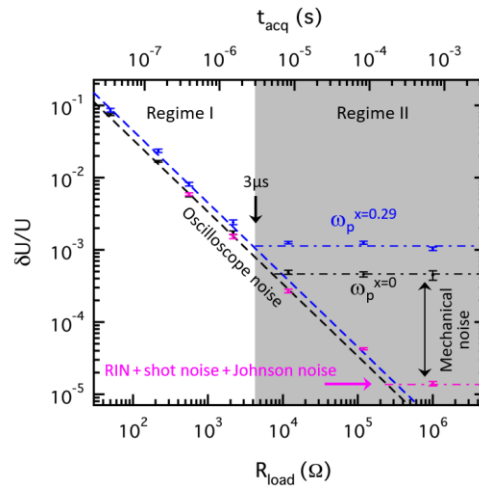


**Figure 4:** Noise-to-signal ratio  $\delta U/U$  of the photovoltage  $U$  induced by the radiated field from the PhC cavity versus the load resistance  $R_{\text{load}}$  of the photodetector, and the corresponding acquisition sampling time  $t_{\text{acq}}$  for pump frequency detunings of  $x = 0$  (dark points) and  $x = 0.29$  (blue points). The error bars correspond to the standard deviation of ten repeated measurements. The black and blue dashed lines correspond to the noise limit imposed by the oscilloscope for  $x = 0$  and  $x = 0.29$ , respectively. The collected powers measured at resonance with  $R_{\text{load}} = 1 \text{ M}\Omega$  for  $x = 0$  and  $x = 0.29$  are  $8 \text{ }\mu\text{W}$  and  $6 \text{ }\mu\text{W}$ , respectively. Purple data points: noise-to-signal ratio without any PhC cavity between the laser source and the photodetector for the same collected power, as in the case of  $x = 0$ . The gray area corresponds to a regime limited by the fundamental thermo-optic noise.

In this thesis, we have also studied the detection limit of photonic crystal cavities for sensing application. In particular, we have determined the trade-off between the detection limit and acquisition speed. Importantly as shown in the **Figure 4**, we have reached a regime where the fundamental thermal fluctuations set the intrinsic detection limit for acquisition sampling times  $t_{\text{acq}}$  larger than  $3 \mu\text{s}$ . Such an intrinsic fundamental limit corresponds to a frequency shift of  $1/2000$  of the linewidth of the cavity resonance for the effective mode volume as small as  $0.06 \mu\text{m}^3$ . The results of this study indicate that it is possible to monitor up to 33 million particles per second with a particle size down to 34 nm, making it a promising technique for fast real-time nanoparticle sensing and biosensing.

# 1

## **Optical cavity enhanced label-free detection**

Optical sensors are powerful detection and analysis tools that rely on changes in the transmission, reflection, absorption, or emission of light. If such a sensor is used for detection and quantification of biological samples, then such kind of sensor can be termed as optical biosensor. In a solution, the detected material is called analyte and could be a disease biomarker, an enzyme, a virus or a protein etc. Optical biosensors are immune to electromagnetic interference and can provide multiplexed detection within a single device. Such tools have vast applications in health care, drug development, food safety, agriculture, environmental monitoring, defense, and homeland security [1-3].

There are different ways of doing biosensing [2-5] and they fall into two classes: labeled and label-free biosensing. In the following sections, we will review the basic principle of both methods. This chapter reviews the recent progress in optical biosensors that use the label-free detection protocol, in which biomolecules are unlabeled or unmodified, and are detected in their natural forms. In this PhD thesis, we will focus on the photonic crystal (PhC) cavities based optical sensors that probe the refractive index (RI) change induced by label-free molecules.

## 1.1 Introduction

It is challenging to detect low concentration of analytes directly through their intrinsic physical properties (such as mass, size, electrical impedance, or dielectric permittivity). So, biological research has historically relied upon attachment of some sort of “label” to one or more of the molecules/viruses/cells being studied [4]. The label is designed to be easily measured by its ability to generate photons at a particular wavelength and acts as a substitute to indirectly indicate the presence of the analyte to which it has been attached. For example, many commercially available fluorescent dyes can be conjugated with DNA, proteins, or cells so that, when illuminated with a laser at the excitation wavelength of the fluorophore, light is emitted at a characteristic wavelength. The process is illustrated in **Figure 1.1**. Such sensors are used due to its selectivity and sensitivity.

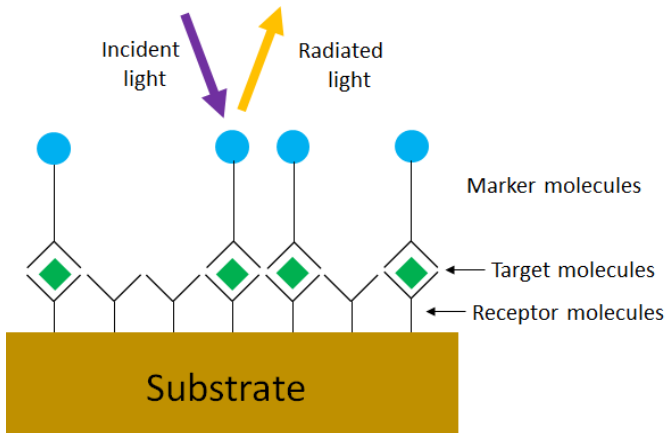


**Figure 1.1:** In labelled biosensing, the target molecules bind to receptor molecules on a substrate so they become immobilised. After that, marker molecules bind to another site of the target molecules. Excess marker molecules are removed and the substrate is illuminated. The intensity of the light is then measured, providing information on the target molecule concentration.

While labeled detection methods can be sensitive down to a single molecule [5], there are several disadvantages associated with the use of labels themselves. First, it may suffer from laborious labeling processes, that may also interfere with the function of a biomolecule and is costly. Markers sometimes do not bind directly to the target molecule so an intermediary molecule is required [6]. Second, labels can structurally and functionally alter the assay. Often, these labels degrade over time, which can reduce the efficiency of the assay. Third, the required washing

between the different steps of the assay increases the sample preparation, it is time consuming, and can reduce the effective throughput. Fourth, these assays can only be performed in an ‘end-point’ fashion, i.e. the signal is only interrogated after the complete assay is finished. This does not allow for continuous, real-time monitoring of molecular interactions so that no kinetic information (i.e. binding of target to receptor molecules as a function of time) can be obtained. Lastly, labelling can be expensive and may suffer from potential bleaching.

In light of the above considerations, significant effort and time have been invested in the development of label-free biosensors for the direct detection of analytes. In the label-free detection, target molecules are not labeled or altered, and are detected in their natural forms which makes the detection relatively easy and cheap to perform.

There are now many methods that allow direct detection of biological analytes without labels. Label-free detection generally involves a transducer capable of directly measuring some physical property of the chemical compound, DNA molecule, peptide, protein, virus, or cell. For example, all biochemical molecules and cells have finite mass, volume, viscoelasticity, dielectric permittivity, and conductivity that can be used to indicate their presence or absence using an appropriate sensor. The sensor functions as a transducer that can convert one of these physical properties (such as the mass of a substance deposited on the sensor’s active surface) into a quantifiable signal that can be gathered by an appropriate instrument (such as a current or voltage proportional to the deposited mass), see **Figure 1.2**. Moreover, a highly-multiplexed assay is easy to perform by measuring multiple transducers with different receptor molecules on the same substrate [7]. Sample preparation is almost not required which decreases costs and enhances the throughput.

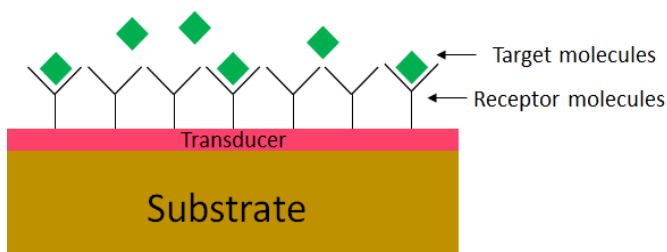


**Figure 1.2:** A transducer is coated with receptor molecules. When target molecules bind to these receptor molecules, the physical properties of the analyte generate an altered state of the transducer which translates into a measurable signal.

In this chapter, label-free optical detection based platform is discussed. The particular type of label-free optical biosensor that is the subject of this research, the planar photonic crystal (PhC) cavity sensor, will be introduced in great detail in the next chapter. These sensors are made of silicon, Earth's second most abundant element, and their fabrication is compatible with techniques that have already been optimized in the semiconductor industry. The sensors are extremely small (tens of microns), so they could eventually be interfaced with lab-on-a-chip systems to become robust, compact, user-friendly diagnostic tools. The scope of this chapter is to provide an overview of RI-based sensing for label-free detection using PhC cavity.

## 1.2 Important aspects and parameters in biosensor development

Depending on the purpose of a biosensor, it should meet several criteria. For example, if the biosensor is designed to detect low concentrations of specific analyte, the biosensor should have a low detection limit (DL) and specificity. The most commonly used quantity in this respect is the detection limit (DL). When utilizing an optical resonator based sensor that tracks a spectral shift, DL is defined as the ratio of the minimum detectable wavelength shift ( $\delta\lambda_{\min}$ ) in the resonator spectrum to the sensitivity (S). This sensitivity can refer to either a change in bulk refractive index, or a change in a concentration of a certain molecule [8,9]. It should be noted that the DL, i.e., the smallest detectable wavelength shift  $\delta\lambda_{\min}$  is not simply the resonator linewidth ( $\Delta\lambda_{\text{FWHM}}$ ). It is only a shift in fraction of the linewidth that can be sensed, i.e.  $\delta\lambda_{\min} = F \cdot \Delta\lambda_{\text{FWHM}}$ , where F is the figure of merit. F can also be defined in term of the quality (Q) factor of the resonator as  $F = Q \cdot \delta\lambda_{\min} / \lambda$ , where  $\lambda$  is the operating wavelength. **Table 1.1** shows reported value of F for different microcavities with acquisition time in millisecond - seconds. Such measurements can compromise the accuracy of the tracking of single biomolecule motion at an acquisition time in line with its inertial time, in view of sensing fast chemical or biological events at the nanoscale. In this thesis, we will experimentally demonstrate that using a PhC cavity,  $F = 1/2000$  at acquisition time of 3  $\mu\text{s}$  can be achieved in air in real-time, which is the lowest value ever reported.

For an optical RI-based label-free sensor, typically there are three ways to specify the DL. First as explained in the last paragraph, since all these sensors are sensitive to the RI change in bulk solution, DL in units of refractive index units (RIU) is naturally used to quantify the sensor performance, which enables a comparison of the sensing capability among different optical technologies and structures. The second way is to use surface mass density (or total mass) in units of  $\text{pgmm}^{-2}$  (or

pg), which is what a biosensor actually measures. While experimentally surface mass density is difficult to determine accurately, it reflects the intrinsic detection capability of a sensor and can be used to evaluate or compare the sensor performance. The third way is to use sample concentration (in units of ng/mL or molarity). Sample concentration is quite useful and easy to determine from an experimental point of view, as no detailed information regarding the mass density on the surface is needed. However, the DL defined in this way depends on the target molecule and its affinity to the biorecognition molecule on the surface, and therefore needs to be specified for each type of a biomolecule. These three DLs are correlated and the detailed relationship among them needs to be studied for each individual optical biosensor. Improvement in the DL can be accomplished by increasing the sensitivity or reducing the noise level.

There are several other criteria for assessing the performances of a typical biosensor, in particular when mass production is considered. These criteria are: specificity, scalability to smaller dimension, measurement time and costs, multiplexing capabilities. We will now discuss various types of integrated photonic refractive index sensors that predated this work.

## 1.3 Label-free biosensor

In the past decade, optical sensor development has been an enthralling and fast-paced area. Various optical structures have been investigated for sensitive label-free detection such as surface plasmon resonance (SPR) based sensors, optical ring resonator based sensors, interferometric waveguide based sensors, 1D photonic crystal (PhC) grating based sensors and PhC cavity based sensor. This chapter also provides an overview on various PhC cavities that have been reported for biosensing application.

### 1.3.1 Surface Plasmon resonance (SPR) biosensors

The SPR sensor is a widely-used type of biosensor. Surface plasmons can be excited when an incident beam of transverse magnetic (TM)-polarized light strikes a thin electrically conducting layer at interface of a thin metal film and a dielectric material. Under condition of total internal reflection (TIR), the incident light will be coupled to a surface plasmon if the incident light wave vector component parallel to the surface matches the surface plasmon wave vector. In SPR biosensing, the adsorption of a targeted analyte by a surface bioreceptor is measured by tracking the change in the conditions of the resonant coupling between the incident light and the propagating surface plasmon wave. The resonant coupling appears as a dip in the reflectivity of the light spectrum, which

is traditionally tracked by measuring the wavelength, the incident angle or the intensity of the reflected light (**Figure 1.3**). The best SPR sensor based on prism coupling provides a DL of  $10^{-7}$  RIU [10]. SPR is widely used due to its robustness and simplicity. However, its large size makes it complex to achieve miniaturization suitable for lab-on-a-chip devices.

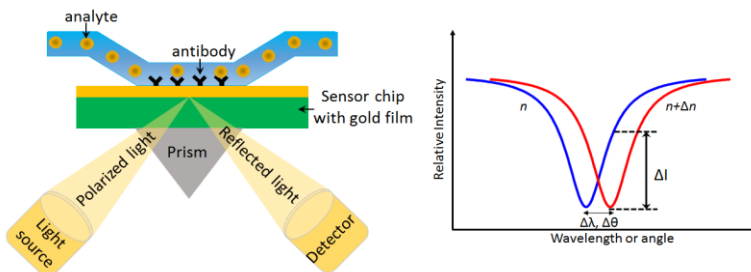


**Figure 1.3:** Schematic of SPR sensing method. Surface plasmon resonance (SPR) detects changes in the refractive index in the immediate vicinity of the surface layer of a sensor chip. SPR is observed as a sharp shadow in the reflected light from the surface at an angle that is dependent on the mass of material at the surface. The SPR angle shifts when biomolecules bind to the surface and change the mass of the surface layer.

### 1.3.2 Ring resonator sensors

In ring resonator sensors, light is coupled into a circular waveguide via the evanescent field of an input waveguide. In general, it consists of a loop and a coupling mechanism to access this loop. When the waves that travel in the loop have a round trip phase shift that equals an integer times  $2\pi$ , the waves interfere constructively and the cavity is in resonance. As a result of TIR along the curved boundary, the waves propagate through the waveguide. Such wave circulates along the resonator surface many times where it interacts with the analyte via the evanescent field. In contrast with straight waveguides, the interaction is no longer determined by the length of the waveguide, but by the number of light circulations within the ring, which is characterized by the resonator quality factor (Q-factor). The presence of an analyte causes RI change near the surface of the ring resonator and changes the effective RI, leading to a spectral shift in the resonance. This can be monitored by scanning the wavelength or by measuring the intensity profile at a fixed wavelength. **Figure 1.4** shows a schematic overview of a ring resonator sensor. Ring resonators have the potential to be combined into highly dense arrays, which is a valuable feature for multiplexing. DL of  $7.6 \times 10^{-7}$  RIU [11] and  $1.5 \text{ pg/mm}^2$  [12] have been achieved. Katrien *et al.* [13] has reported a ring resonator in silicon with a detection limit of  $10^{-5}$  RIU.

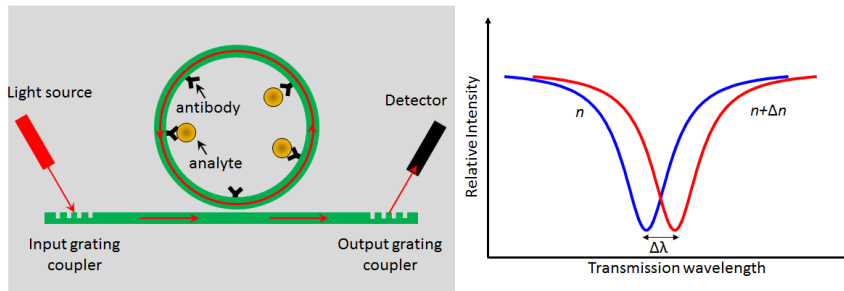


**Figure 1.4:** Schematic overview of a ring resonator sensor, in which RI changes are measured as a change in transmission wavelength, as the light coupled from the input waveguide to the circular waveguide changes, because of the change in the resonant wavelength of the circular waveguide.

Microtoroid and microsphere based resonator also have high Q-factor which supports WGM modes and detects the binding of analyte molecules as changes in the resonance frequency. However, such sensors are difficult to integrate with waveguide and further multiplexing. The detection of single viruses, proteins, or other biomolecules using microsphere has been demonstrated by [14].

### 1.3.3 Interferometric waveguide sensors

In interferometric sensors, two or more confined light waves form an interference pattern which is measured over time. Interactions with the external medium (sample) via the evanescent field result in changes in velocity between the waves, which can be analyzed from the interference pattern. High sensitivities can be achieved, due to the option of using long interaction lengths.

The most basic and most common type of interferometric sensor is the Mach-Zehnder interferometer (MZI). As illustrated in **Figure 1.5**, the monochromatic and polarized light from the laser source is coupled into the input waveguide. This light gets split via a Y-junction into two arms (sensing arm and reference arm) and is recombined again through a similar structure. The sensing arm and reference arm does not necessarily have to be of equal length. After recombination, the intensity depends on the cosine of the accumulated phase difference. Because of the presence of the analytes in the sensing window, a phase difference  $\Delta\varphi$  between the sensing arm and the reference arm occurs due to change in effective refractive index of the guiding mode in the sensing arm. This results in an intensity modulation caused by the interference of the two arms at the waveguide output. The presence of the analytes can be detected by measuring

the interference intensity at the output waveguide. A DL of  $5 \times 10^{-8}$  RIU was reported by Heideman and Lambeck [15]. Apart from MZI, there are other examples of interferometric devices which can be used as biosensors such as bimodal [16], dual polarization [17], Hartman [18] and Young interferometers [19].

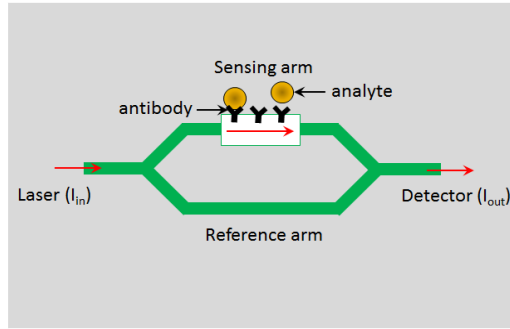
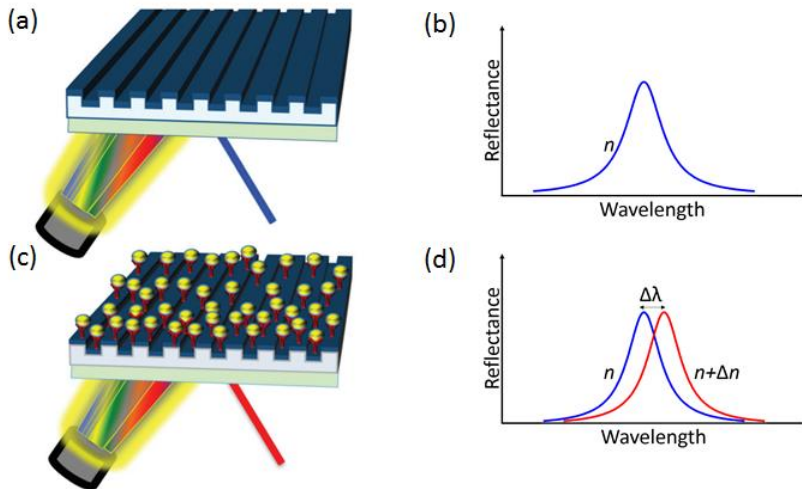


Figure 1.5: Illustration of a MZI sensor.

### 1.3.4 1D photonic crystal grating based sensors

One dimensional PhC structures are commonly fabricated from a high refractive index coating layer over a periodically arranged low refractive index grating layer (Figure 1.6). In these PhC gratings, only the zeroth order mode is allowed, while higher order modes are restricted at normal incidence, provided that the period of the grating is smaller than the wavelength of the incident light. Such PhC gratings can be designed to reflect a narrow band of wavelengths and produce a sharp peak in the reflection spectrum.

Resonance occurs when a diffracted mode from the grating couples to a leaky waveguide mode. Radiation from the leaky mode undergoes constructive interference with the reflected wave and destructive interference with the transmitted wave, resulting in a resonant reflection. This resonance behavior of PhC gratings is highly sensitive to the localized changes in refractive index on the grating surface, which makes it suitable for, biosensing application [20]. A biochemical interaction (e.g., binding) on the PhC surface causes a change in the effective refractive index, which results in a shift of the resonance wavelength peak, which is proportional to the concentration of the biotarget (Figure 1.6).



**Figure 1.6:** Overall mechanism of biosensing using PhC grating. (a) An example of the 1-D PC slab surface. (b) Corresponding resonance peak wavelength for this PC slab. (c) Functionalization of the slab surface and biological binding event via antigen–antibody interaction. (d) Peak wavelength shift as a result of this interaction. Reproduced from [20].

### 1.3.5 Photonic crystal cavity based sensors

Photonic crystal (PhC) based sensors consist of a periodic pattern whose lattice constant consists of the order of the wavelength of the light. Due to a periodicity, photonic bandgaps (PBG) are generated; the light whose wavelength lies within the PBG cannot propagate through the PhC. This results in a wide stopband in the transmission or reflection spectrum. However, by locally perturbing the structure of the PhC, a photonic “defect” within the bandgap can be introduced, leading to the formation of a defect mode. Consequently, light resonant with this defect mode can propagate through the PhC, resulting in a high transmission peak within the bandgap. The spectral position of this peak strongly depends on the local environment around the defect. For that reason, this can be used for sensing molecules binding to the defect, which is illustrated schematically in **Figure 1.7**. Parallel detection and light interaction with volumes down to femtolitres are possible, because light can be localized and concentrated in very small volumes.

PhC cavity based sensors have many advantages compared to other kinds of sensors. Firstly, PhC has very small footprint and high quality factor/volume (Q/V) ratio. It has been proven that with fine structural optimization a photonic crystal cavity can have a quality factor (Q) as high as  $10^6$  [22–25] with very small dimensions [26,27], on the order of  $\lambda^3$ , which enhances light-matter interaction

effects. It should be noted that the enhancement of the light-matter interaction is concomitant with a decrease of the interaction volume.

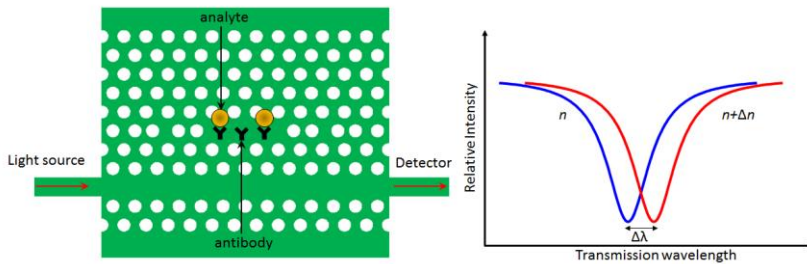


**Figure 1.7:** Schematic overview of a photonic crystal based sensor, where binding of an analyte to the antibody results in a shift in transmission wavelength.

Therefore, tiny variations in refractive index are measurable and reflected in the optical properties of the photonic crystal cavities. Secondly, photonic crystal can be easily integrated with other on-chip elements. A potential utilization of this feature is being used as an on-chip label-free biosensor in planar geometries [28].

All the above mentioned microcavities can be characterized by two figures of merits: the temporal confinement is described by the quality ( $Q$ ) factor of the mode, and the spatial confinement is characterized by the mode volume ( $V$ ). While  $Q$ -factor is imperative in many applications, minimizing mode volume is very important for biochemical sensing application. In particular, a high  $Q/V$  ratio is desirable in biochemical sensors. However, extremely high sensitivity of resonance wavelengths to slight changes in the environmental noise (temperature, pressure, etc.) can easily shift the resonance. To circumvent this shortcoming, resonance stabilization schemes need to be employed and therefore all the experiments are implemented in temperature-stabilized laboratory environments, which limits their practical applications and makes the detection-set-up bulky and expensive. So, there is a need of a robust resonator which can have moderately high  $Q$  factor ( $\sim 10^4$ ) where cavity stabilization is not required but simultaneously can have low mode volume ( $\sim 0.06\mu\text{m}^3$ ). PhC based cavities can have such values of  $Q$  and  $V$  and hence can be a promising candidate for a biosensing specially for single molecule detection. One of the objective of the PhD thesis was to evaluate DL of such cavities.

Nowadays, integrated PhC cavity based sensors represent a potential class of photonic sensors which can be employed for physical and chemical/biochemical sensing. The choice of the substrate for semiconductor-based planar PhC sensors

depends on whether an active or passive optical cavity is used. The slab material must provide optical gain for active cavity devices, so compound semiconductors are chosen because of their desirable electronic band properties. For these types of devices, hetero-epitaxial layers such as AlGaAs, InGaAs, GaAs, III-nitride compound layers are typically used. These devices potentially offer the full on-chip integration with sources and detectors, or may be operated as lasers [29] to decrease the detection level. In addition, they can be employed using remote readout, not requiring the delicate attachment of optical fibers or electrical wiring. Silicon based substrates (Si or SiN) are most often used for passive optical cavity sensors. The most common substrate used for passive cavity slab-PhCs is silicon-on-insulator (SOI), in which a thin device layer of Si (< 500 nm) is situated on top of a thicker layer of SiO<sub>2</sub>. Nearly all passive-cavity slab-PhCs operate at IR wavelengths, although some SiN devices can potentially operate at visible wavelength [30].

**Table 1.1:** Reported figure of merit (F) of different microcavities.

Device	F	Reference
Ring resonator	1/15	[13]
Microsphere	1/78	[31]
Microtoroid	1/25000	[32]
1D PhC grating	1/4.8	[21]

## 1.4 State of the art on refractive index sensing

In last decade, 2D planar PhC sensors have been widely investigated for detecting analytes. This section covers a review of experimental results that have been reported in the literature, organized into the following sub-sections: bulk-RI sensing (of a liquid or gaseous volume), detection of biological macromolecules (e.g. proteins, nucleic acids), and detection of targets with a particle morphology (e.g. nanoparticles, viruses). In order to sense an analyte, bulk-RI sensing measurements do not require any particular surface functionalization of the sensor surface. Thus, bulk-RI sensing is relatively simpler compared as it does not require some form of chemical or biochemical binding interaction to ensure target capture by an immobilized probe at the sensor surface.

### 1.4.1 Bulk RI Sensing

Bulk-RI sensitivity measurement is often used as a performance metric to compare different PhC sensor designs. As all of the PhC sensors that have been used to measure bulk-RI changes have relied on the shift in the cavity spectrum, the RI sensitivity is reported as wavelength redshift per refractive index unit (nm/RIU). **Table 1.2** displays a list of the reported bulk-RI sensitivities, as well as detection limits if they were reported. The highest reported bulk-RI sensitivity was over 1500 nm/RIU, achieved by Di Falco *et al.* with a slotted PhC cavity [39]. The authors attributed the high sensitivity to the length of the cavity and the strength of the electric field within the narrow-slotted channel. But it should be noted that this high value of sensitivity was measured only for a change in RI of a solution to another one. If we plot the reported shift in resonance due to change in RI of background solution, then data points will not follow a linear behavior. This raises a question about the uniqueness of the cavity mode. It may happen that sensitivity of 1500 nm/RIU was measured with two different cavity modes.

This table also shows the corresponding figure of Merit,  $F (= Q \cdot \delta\lambda_{\min} / \lambda)$ , where  $Q$  is the quality factor of the cavity,  $\delta\lambda_{\min}$  is the minimum detected wavelength shift in the cavity spectrum, and  $\lambda$  in the pump wavelength. In can be seen from that even though Di Falco *et al.* reported highest reported sensitivity,  $F$  is only 1/2.6.

**Table 1.2:** Reported bulk RI sensitivities of different 2D PhC structures.

Bulk RI Measurements						
2D PhC Design	S (nm/RIU)	$\Delta n$ (RIU)	$\delta\lambda_{\min}$ (nm)	Q	F	Reference
Microcavity	176	NR	NR	NR	NR	[33]
Microcavity	200	$1 \times 10^{-3}$	0.2	400	1/18.75	[34]
PhC waveguide	64	NR	NR	NR	NR	[35]
Point-shift nanocavity	350	$9 \times 10^{-5}$	0.0315	1617	1/31.75	[36]
PhC waveguide	88,120	NR	NR	NR	NR	[37]
Waveguide heterostructure cavity	80	NR	NR	NR	NR	[38]
Slotted heterostructure cavity	1538	$7.8 \times 10^{-6}$	0.012	50000	2.6	[39]

Width modulated cavity	103	$2.4 \times 10^{-3}$	0.247	3033	2.02	[40]
Microcavity	161-176	NR	NR	NR	NR	[41]
Suspended PhC lattice	510	NR	NR	NR	NR	[42]
Active cavity in a honeycomb lattice	135	$1 \times 10^{-3}$	0.135	2800	1/4.016	[43]
Periodic lattice in silk polymer	400	$7 \times 10^{-3}$	2.8	9.4	1/19.95	[44]
Microcavity	280	NR	NR	NR	NR	[45]
Pillar microcavity	350	$3 \times 10^{-4}$	2.45	27600	1/0.022	[46]
Slotted PhC	510	$1 \times 10^{-5}$	0.0051	26000	1/11.82	[47]
Single hole and multiple hole defects in L3 cavity	91,98	NR	NR	NR	NR	[48]
Microcavity coupled to W1 waveguide	65.5	$1 \times 10^{-2}$	0.655	457	1/5.212	[49]
L7 cavity with three pairs of small radius holes	460	NR	NR	NR	NR	[50]
L13 cavity coupled to W1 waveguide	52,66	NR	NR	NR	NR	[51], [52]

## 1.4.2 Biological macromolecule sensing

The ability to detect changes in the bulk-RI of a solution is not sufficient for the implementation of a planar PhC as a biosensor. In order to use planar PhC cavities as a biosensor, it must provide a selective response for a particular analyte. This requires the PhC membrane surface to be specifically functionalized with a receptor that can selectively bind a target analyte. **Table 1.3** summarizes the reported detection of a number of different biological molecules with a planar PhC sensor. As indicated in the table, detection results have been achieved for several assay formats: end-point measurement of dried chips, measurement of sensors immersed in stationary liquids, and measurement of sensors integrated with microfluidic flow channels.

### 1.4.3 Particle Sensing

In the previous subsection, detection of nucleic acids and proteins was considered. Such macromolecules typically have dimensions of the order of a few nanometers. However, biological targets such as viruses and cell organelles, have dimensions on the order of tens to hundreds of nanometers. These targets are considered to have a “particle-like” morphology. Due to lab safety concerns regarding the handling of virus samples, latex particles are often used as “virus simulants” in preliminary sensing experiments. Reported detection results for particle-like targets are displayed in the lower section of **Table 1.3**.

These studies have demonstrated the ability of 2D PhCs to detect particles in complex matrices such as serum and saliva, albeit in an end-point assay format. This provides motivation for the further development of these devices to achieve the predicted sensitivity of a single particle in fluidic environment. If this sensitivity can be achieved experimentally, then, it could either aid in the early diagnosis of diseases or in monitoring the disease condition during the treatment procedures. Hence, we have focused our research efforts in developing a microcavity which can find application in detecting nanoparticles in a microfluidic flow or in air with the ultimate goal of detecting a single particle.

It is important to note that the field of 2D PhCs as label-free biosensors is still at an early stage. The optical mode overlap with the analyte molecule, the probe density and the assay mode are all vastly different among the PhC designs reported in the literature. Consequently, the reported detection limit for analyte detection cannot be directly compared between different PhC designs. Additionally, many of these designs are reported as “proof-of-concept” structures, and are highly un-optimized. Therefore, the table should be strictly viewed as an overview of all the biosensing studies conducted thus far with 2D PhCs, and performance metrics assessed with substantial caution.

All the PhC structures mentioned in Table 1.3 were fabricated using electron-beam lithography and hence cannot be used for mass production. Recently, Feng *et al.* reported detection of biomarker down to sub-pg/ml with photonic crystal nanobeam cavities fabricated with scalable deep-UV (DUV) lithography [68].

The demonstration of PhC cavity sensing on industrial scale is yet to be demonstrated. The goal of this thesis is to present fabrication of planar 2D PhC cavities for sensing application using DUV lithography. Several aspects that need to be considered regarding the fabrication of such structures using DUV lithography are presented in chapter 3.

**Table 1.3:** Reported detection limits and dynamic range for sensing biomolecules and particles using 2D PhCs in three different assay modes.

Assay Mode	Analyte	Analyte-Ligand	Reported DL	Reference
Dry	Protein	BSA (covalently bound to glutaraldehyde modified surface)	2.5 fg	[53]
		Streptavidin binding to Biotin	0.86 nm shift for 2.5 nm thick protein layer	[37]
		BSA (adsorbed to octadecanethiol modified surface)	2.2 fg	[54]
		IgG-anti-IgG	6.7 nM, 1.5 fg	[49]
Wet	Protein	BSA (adsorbed)	10 $\mu\text{g}/\text{mL}$	[35]
		BSA (adsorbed)	4 fg, 500 pg/ $\text{mm}^2$	[40]
		anti-BSA binding to BSA	0.2 fg, 2.1 pg/ $\text{mm}^2$	[55]
		BSA (covalently bound to glutaraldehyde surface)	255 fM	[36]
		Rat Anti-human IL-10 IgG binding to human IL-10	98 ag, 10.6 ag (22 pg/ $\text{mm}^2$ )	[51], [56], [57]
		ZEB 1 from lung lysates	2 cells/ $\mu\text{L}$	[58]
	Nucleic acid	Complimentary ssDNA to probe ssDNA	19.8 nM	[59]
		Anti-biotin binding to biotinylated BSA	20 pM, 21 ag	[41]
Microfluidic	Protein	Insulin binding to anti-insulin	6pM	[61]
		Avidin binding to biotin	1 $\mu\text{g}/\text{mL}$ , 100 ag, 60 pg/ $\text{mm}^2$	[62]
Dry	Particle	Latex particle (~370 nm in diameter, adsorbed)	Single particle	[63]
		Latex particle (~100 nm in diameter, adsorbed)		[64]
		Influenza virus binding to specific antibodies	1 ng/mL (spiked in saliva)	[65]

		<i>Legionella pneumophila</i> (bacteria) binding to antibodies	200 cells/mL	[66]
		HPV VLPs binding to specific antibodies	1.5 nM (spiked in FBS)	[67]

Konopsky *et al.* used two-mode photonic structures and demonstrated their ability to track the thickness of adsorbed molecules and their conformation [69]. In terms of single-particle detection, optical resonators such as microspheres [70] and microtoroids [70-72] have been used to detect individual virus particles (~100 nm). Judith *et al.* reported improvement in detection capability by using a frequency locked optical whispering evanescent resonator (FLOWER) [32]. In FLOWER, light is evanescently coupled into a glass microtoroid optical resonator using an optical fiber. FLOWER detects changes in the effective index of refraction of the microtoroid as particles enter its evanescent field. These RI changes are detected by monitoring the corresponding changes in the resonance frequency of the microtoroid. With this system, they have reported the detection of single nanoparticles with a radius of 2.5 nm. But, it should be noted that for a microtoroid to detect particles of comparable size to single protein molecules (2.5 nm radius), one must be able to resolve a wavelength shift less than 0.006 fm. This kind of shift detection is very difficult to achieve as the pump wavelength must be stabilized. In order to detect such small wavelength shifts, they used frequency locking in combination with filtering techniques to reduce the noise level to  $9.6 \times 10^{-4}$  fm over one-millisecond intervals. This kind of technique is slower and requires some data processing whereas the PhC cavity only require shift in picometer meter range to detect a sub nanoparticles particle in real time [73, 74].

## 1.5 Thesis Organization

The outline of the remainder of this thesis is as follows:

**In the second chapter**, a brief introduction to photonic crystals is provided. Photonic bandgap effects, cavity defect mode formation and waveguide defects are explained and illustrated. Focus is then made specifically on the properties of two-dimensional silicon photonic crystal membranes and cavities. Finally, an overview of planar photonic crystal cavities in silicon membranes is provided.

**In the third chapter**, a complete description of the optical set up is provided. This set-up is needed to accurately investigate the physical properties of PhC cavities. The first section includes an overview and general considerations for the

setup. Each of the following sections is then dedicated to the accurate assembly and characteristics of a separate constituent. The main parts described are the End-fire path, visible imaging path, near infrared imaging path.

**The fourth chapter** provides a methodology to post-process a large array of a few hundred-nanometer thin photonic membranes that were fabricated using complementary metal-oxide-semiconductor (CMOS) technological platform. The postprocessing results in local removal of the silicon substrate and of the buried oxide, which provides a free access from both side of the membrane of the photonic structures. The membranes are patterned with photonic crystal cavities by deep ultraviolet lithography. It is shown that the proposed process is compatible with the integration of micrometer-sized SU8-based polymer waveguides. In addition, although a significant number of processing steps is required to achieve such free-standing substrate-less cavities, the quality (Q) factors of the cavities that is of the order of a few thousand remains unaffected.

**In the fifth chapter**, the experimental results that have been achieved regarding the quantification of the intrinsic detection limit in a planar photonic crystal cavity are presented. The main limiting factors are investigated. The current study makes it possible to answer the question: what is the trade-off between the acquisition speed and the detection limit to track a nanoparticle in real time with a resonant cavity field.

The **sixth chapter** provides concluding remarks on the technological advancements accomplished for 2D PhC biosensor platform in this thesis. In addition, future directions for the further development of this biosensing platform will be highlighted.

## 1.6 Publications

### International Journals

- [1] Tormo, A.D., Khalenkow, D., Saurav, K., Skirtach, A.G. and Le Thomas, N., 2017. Superresolution  $4\pi$  Raman microscopy. *Optics Letters*, 42(21), pp.4410-4413.
- [2] Saurav, K. and Le Thomas, N., 2017. Probing the fundamental detection limit of photonic crystal cavities. *Optica*, 4(7), pp.757-763.
- [3] Saurav, K., Kumari, S. and Le Thomas, N., 2017. CMOS fabricated large array of free standing substrate-less photonic crystal cavities for biosensing applications. *IEEE Photonics Journal*, 9(2), pp.1-8.

## International Conferences

- [1] K. Saurav, S. Kumari, N. Le Thomas, "CMOS fabricated large array of free standing substrate-less photonic crystal cavities for biosensing applications", IEEE Photonics Conference (IPC), (2017).
- [2] K. Saurav, N. Le Thomas, "Impact of the light coupling on the sensing properties of photonic crystal cavity modes", SPIE Photonics West, United States, pp. paper 10077OP (2017).
- [3] K. Saurav, N. Le Thomas, "Imaging of photonic crystal cavity mode via refractive index sensing", Proceedings of the 21st Annual Symposium of the IEEE Photonics Benelux Chapter, Belgium, pp. 255-258 (2016).
- [4] K. Saurav, N. Le Thomas, "Mapping nano-object induced perturbations of photonic crystal cavity modes", PECS-XII, United Kingdom, (2016).
- [5] K. Saurav, N. Le Thomas, "Fabrication of substrate-less planar silicon photonic crystal cavities ", Proceedings of the 20th Annual Symposium of the IEEE Photonics Benelux Chapter, (2015).
- [6] K. Saurav, N. Le Thomas, "On-chip photonic crystal cavity designs for nanoparticle characterization ", Taking Detection to the Limit: Biosensing with Optical Microcavities., Germany, (2014).

## References

- [1] Lieberzeit, P. A.; Dickert, F. L., Rapid Bioanalysis with Chemical Sensors: Novel Strategies for Devices and Artificial Recognition Membranes. *Anal. Bioanal. Chem.* 2008, 391, 1629-1639.
- [2] J. H. T. Luong, K. B. Male, J. D. Glennon, Biosensor technology: technology push versus market pull. *Biotechnol. Adv.* 26, 492–500 (2008).
- [3] Nakamura, H.; Karube, I., Current research activity in biosensors: review. *Anal Bioanal Chem* 2003, 377, 446-468.
- [4] M. A. Cooper, B. T. Cunningham, in *Label-Free Biosensors: Techniques and Applications*, M. A. Cooper, Ed. (Cambridge University Press, NY, 2009), pp. 1–10.
- [5] Campos, L.A., Liu, J., Wang, X., Ramanathan, R., English, D.S. and Muñoz, V., 2011. A photoprotection strategy for microsecond-resolution single-molecule fluorescence spectroscopy. *Nature methods*, 8(2), p.143.
- [6] M. L. Phelan and S. Nock. Generation of bioreagents for protein chips. *Proteomics*, 3:2123–2134, November 2003.
- [7] K. De Vos. Label-free Silicon Photonics Biosensor Platform with Microring Resonators. Phd dissertation, Ghent University, Ghent, 2010.
- [8] I.M. White, X. Fan, *Opt. Express* 16 (2008) 1020.
- [9] N.A. Mortensen, S. Xiao, J. Pedersen, *Microfluid. Nanofluid.* 4 (2008) 117.
- [10] J. Homola, "Surface plasmon resonance sensors for detection of chemical and biological species," *Chemical Reviews* 108, 462- 493 (2008).
- [11] M. Iqbal, M. A. Gleeson, B. Spaugh, F. Tybor, W. G. Gunn, M. Hochberg, T. Baehr- Jones, R. C. Bailey, and L. C. Gunn, "Label- Free Biosensor

- Arrays Based on Silicon Ring Resonators and High-Speed Optical Scanning Instrumentation,” *IEEE J. Sel. Top. Quant. Electron.* 16, 654–661 (2010).
- [12] M. S. Luchansky, A. L. Washburn, T. A. Martin, M. Iqbal, L. C. Gunn, and R. C. Bailey, “Characterization of the evanescent field profile and bound mass sensitivity of a label-free silicon photonic microring resonator biosensing platform,” *Biosens. Bioelectron.* 26, 1283–1291 (2010).
- [13] K. De Vos, I. Bartolozzi, E. Schacht, P. Bienstman, and R. Baets. Silicon-on-Insulator microring resonator for sensitive and label-free biosensing. *Optics Express*, 15(12):7610–7615, June 2007.
- [14] Vollmer, F. and Arnold, S., 2008. Whispering-gallery-mode biosensing: label-free detection down to single molecules. *Nature methods*, 5(7), p.591.
- [15] Heideman, R.G. and Lambeck, P.V., 1999. Remote opto-chemical sensing with extreme sensitivity: design, fabrication and performance of a pigtailed integrated optical phase-modulated Mach–Zehnder interferometer system. *Sensors and Actuators B: Chemical*, 61(1-3), pp.100-127.
- [16] Dante, S., Duval, D., Fariña, D., González- Guerrero, A.B. and Lechuga, L.M., 2015. Linear readout of integrated interferometric biosensors using a periodic wavelength modulation. *Laser & Photonics Reviews*, 9(2), pp.248-255.
- [17] Estevez, M.C., Alvarez, M. and Lechuga, L.M., 2012. Integrated optical devices for lab-on-a-chip biosensing applications. *Laser & Photonics Reviews*, 6(4), pp.463-487.
- [18] Xu, J., Suarez, D. and Gottfried, D.S., 2007. Detection of avian influenza virus using an interferometric biosensor. *Analytical and bioanalytical chemistry*, 389(4), pp.1193-1199.
- [19] Schmitt, K., Schirmer, B., Hoffmann, C., Brandenburg, A. and Meyrueis, P., 2007. Interferometric biosensor based on planar optical waveguide sensor chips for label-free detection of surface bound bioreactions. *Biosensors and Bioelectronics*, 22(11), pp.2591-2597.
- [20] Inan, H., Poyraz, M., Inci, F., Lifson, M.A., Baday, M., Cunningham, B.T. and Demirci, U., 2017. Photonic crystals: emerging biosensors and their promise for point-of-care applications. *Chemical Society Reviews*, 46(2), pp.366-388.
- [21] Cunningham, B., Zhang, M., Zhuo, Y., Kwon, L. and Race, C., Review of Recent Advances in Biosensing with Photonic Crystal Surfaces. *IEEE Sens. J.*, pp.1-1.
- [22] Y. Akahane, T. Asano, B. S. Song, and S. Noda, “High-Q photonic nanocavity in a two-dimensional photonic crystal,” *Nature* 425(6961), 944–947 (2003).
- [23] Y. Akahane, T. Asano, B. S. Song, and S. Noda, “Fine-tuned high-Q photonic-crystal nanocavity,” *Opt. Express* 13(4), 1202–1214 (2005).
- [24] B. Song, S. Noda, T. Asano, and Y. Akahane, “Ultra-high-Q photonic double-heterostructure nanocavity,” *Nat. Mater.* 4(3), 207–210 (2005)
- [25] T. Asano, B. S. Song, and S. Noda, “Analysis of the experimental Q factors (~ 1 million) of photonic crystal nanocavities,” *Opt. Express* 14(5), 1996–2002 (2006).

- [26] S. Johnson, S. Fan, P. Villeneuve, J. Joannopoulos, and L. Kolodziejski, "Guided modes in photonic crystal slabs," *Phys. Rev. B* 60(8), 5751–5758 (1999).
- [27] T. Krauss and R. De La Rue, "Photonic crystal in the optical regime—past, present and future," *Prog. Quantum Electron.* 23(2), 51–96 (1999).
- [28] N. Mortensen, S. Xiao, and J. Pedersen, "Liquid-infiltrated photonic crystals: enhanced light-matter interactions for lab-on-a-chip applications," *Microfluid. Nanofluid.* 4(1–2), 117–127 (2008).
- [29] Dündar, M.A., Ryckeboosch, E.C., Nötzel, R., Karouta, F., van IJzendoorn, L.J. and van der Heijden, R.W., 2010. Sensitivities of InGaAsP photonic crystal membrane nanocavities to hole refractive index. *Optics express*, 18(5), pp.4049–4056.
- [30] Kassa-Baghdouche, L., Boumaza, T., Cassan, E. and Bouchemat, M., 2015. Enhancement of Q-factor in SiN-based planar photonic crystal L3 nanocavity for integrated photonics in the visible-wavelength range. *Optik-International Journal for Light and Electron Optics*, 126(22), pp.3467–3471.
- [31] Baaske, M.D., Foreman, M.R. and Vollmer, F., 2014. Single-molecule nucleic acid interactions monitored on a label-free microcavity biosensor platform. *Nature nanotechnology*, 9(11), p.933.
- [32] Su, J., Goldberg, A.F. and Stoltz, B.M., 2016. Label-free detection of single nanoparticles and biological molecules using microtoroid optical resonators. *Light: Science & Applications*, 5(1), p.16001.
- [33] Lonkar, M., Scherer, A. & Qiu, Y. Photonic crystal laser sources for chemical detection. *Appl. Phys. Lett.* 82, 4648 (2003).
- [34] Chow, E., Grot, A, Mirkarimi, L. W., Sigalas, M. & Girolami, G. Ultracompact biochemical sensor built with two-dimensional photonic crystal microcavity. *Opt. Lett.* 29, 1093–5 (2004).
- [35] Skivesen, N., Têtu, A., Kristensen, M. & Lyngby, D.-K. Photonic-crystal waveguide biosensor. *Opt. Express* 15, 3169–76 (2007).
- [36] Kita, S., Nozaki, K. & Baba, T. Refractive index sensing utilizing a CW photonic crystal nanolaser and its array configuration. *Opt. Express* 16, 8174–80 (2008).
- [37] Buswell, S. C., Wright, V. A, Buriak, J. M., Van, V. & Evoy, S. Specific detection of proteins using photonic crystal waveguides. *Opt. Express* 16, 15949–57 (2008).
- [38] Sunner, T. Stichel, T., Kwon, S. –H., Schlereth, T. W., Hofling, S., Kamp, M. & Forchel, A. Photonic crystal cavity based gas sensor. *Appl. Phys. Lett.* 92, 261112 (2008).
- [39] Di Falco, A., O’Faolain, L. & Krauss, T. F. Chemical sensing in slotted photonic crystal heterostructure cavities. *Appl. Phys. Lett.* 94, 063503 (2009).
- [40] Dorfner, D., Zabel, T., Hurlimann, T., Hauke, N., Frandsen, L., Rant, U., Abstreiter, G. & Finley, J. Photonic crystal nanostructures for optical biosensing applications. *Biosens. Bioelectron.* 24, 3688–92 (2009).
- [41] Zlatanovic, S., Mirkarimi, L. W., Sigalas, M. M., Bynum, M. A., Chow, E., Robotti, K. M. Burr, G. W., Esener, S. & Grot, A. Photonic crystal

- microcavity sensor for ultracompact monitoring of reaction kinetics and protein concentration. *Sensors Actuators B Chem.* 141, 13–19 (2009).
- [42] Huang, M., Yanik, A. A., Chang, T.-Y. & Altug, H. Sub-wavelength nanofluidics in photonic crystal sensors. *Opt. Express* 17, 24224–33 (2009).
- [43] Kim, S., Lee, J., Jeon, H. & Kim, H. J. Fiber-coupled surface-emitting photonic crystal band edge laser for biochemical sensor applications. *Appl. Phys. Lett.* 94, 133503 (2009).
- [44] Amsden, J. J. Perry, H., Boriskina, S. V., Gopinath, A., Kaplan, D. L., Negro, L. D. & Omenetto, F. G. Spectral analysis of induced color change on periodically nanopatterned silk films. *Opt. Express* 17, 21271–9 (2009).
- [45] Dündar, M. A., Ryckebosch, E. C. I., Notzel, R., Karouta, F., van IJzendoorn, L. J. & van der Heijden, R. W. Sensitivities of InGaAsP photonic crystal membrane nanocavities to hole refractive index. *Opt. Express* 18, 4049–56 (2010).
- [46] Xu, T., Zhu, N., Xu, M. Y. -C., Wosinski, L., Aitchison, J. S. & Ruda, H. E. Pillar-array based optical sensor. *Opt. Express* 18, 5420–5 (2010).
- [47] Jágerská, J., Zhang, H., Diao, Z., Le Thomas, N. & Houdré, R. Refractive index sensing with an air-slot photonic crystal nanocavity. *Opt. Lett.* 35, 2523–5 (2010).
- [48] Kang, C., Phare, C. T., Vlasov, Y. a, Assefa, S. & Weiss, S. M. Photonic crystal slab sensor with enhanced surface area. *Opt. Express* 18, 27930–7 (2010).
- [49] Pal, S., Guillermain, E., Sriram, R., Miller, B. L. & Fauchet, P. M. Silicon photonic crystal nanocavity-coupled waveguides for error-corrected optical biosensing. *Biosens. Bioelectron.* 26, 4024–31 (2011).
- [50] Liu, Y. & Salemink, H. W. M. Photonic crystal-based all-optical on-chip Sensor. *Opt. Express* 20, 19912–20 (2012).
- [51] Lai, W.-C., Chakravarty, S., Zou, Y. & Chen, R. T. Silicon nano-membrane based photonic crystal microcavities for high sensitivity bio-sensing. *Opt. Lett.* 37, 1208–10 (2012).
- [52] Lai, W.-C., Chakravarty, S., Zou, Y., Guo, Y. & Chen, R. T. Slow light enhanced sensitivity of resonance modes in photonic crystal biosensors. *Appl. Phys. Lett.* 102, 41111 (2013).
- [53] Lee, M. R. & Fauchet, P. M. Two-dimensional silicon photonic crystal based biosensing platform for protein detection. *Opt Express* 15, 4530–35 (2007).
- [54] Lu, T.-W., Lin, P.-T., Sio, K.-U. & Lee, P.-T. Optical sensing of square lattice photonic crystal point-shifted nanocavity for protein adsorption detection. *Appl. Phys. Lett.* 96, 213702 (2010).
- [55] García-Rupérez, J., Toccafonda, V., Bañuls, M. J., Castelló, J. G., Griol, A., Peransi-Llopis, S. & Maquieira, Á. Label-free antibody detection using band edge fringes in SOI planar photonic crystal waveguides in the slow-light regime. *Opt. Express* 18, 24276–86 (2010).
- [56] Zou, Y., Chakravarty, S., Lai, W.-C., Lin, C.-Y. & Chen, R. T. Methods to array photonic crystal microcavities for high throughput high sensitivity biosensing on a silicon-chip based platform. *Lab Chip* 12, 2309–12 (2012).

- [57] Chakravarty, S., Zou, Y., Lai, W.C. and Chen, R.T., 2012. Slow light engineering for high Q high sensitivity photonic crystal microcavity biosensors in silicon. *Biosensors and Bioelectronics*, 38(1), pp.170-176.
- [58] Chakravarty, S., Lai, W. -C., Zou, Y., Drabkin, H. A., Gemmill, R. M., Simon, G. R., Chin, S. H. & Chen, R. T. Multiplexed specific label-free detection of NCI-H358 lung cancer cell line lysates with silicon based photonic crystal microcavity biosensors. *Biosens. Bioelectron.* 43, 50–5 (2013).
- [59] Toccafondo, V., García-Rupérez, J., Bañuls, M. J., Castelló, J. G., Peransi-Llopis, S. & Maquieira, A. Single-strand DNA detection using a planar photonic-crystal-waveguide-based sensor. *Opt. Lett.* 35, 3673–5 (2010).
- [60] Zlatanovic, S., Mirkarimi, L. W., Sigalas, M. M., Bynum, M. A., Chow, E., Robotti, K. M. Burr, G. W., Esener, S. & Grot, A. Photonic crystal microcavity sensor for ultracompact monitoring of reaction kinetics and protein concentration. *Sensors Actuators B Chem.* 141, 13–19 (2009).
- [61] Endo, T., Sato, M., Kajita, H., Okuda, N., Tanaka, S. & Hisamoto, H. Printed two-dimensional photonic crystals for single-step label-free biosensing of insulin under wet conditions. *Lab Chip* 12, 1995–9 (2012).
- [62] Scullion, M. G., Krauss, T. F. & Di Falco, A. Slotted photonic crystal for biosensing applications. *Proc SPIE* 8425, 842507–8 (2012).
- [63] Lee, M.R. and Fauchet, P.M., 2007. Nanoscale microcavity sensor for single particle detection. *Optics letters*, 32(22), pp.3284-3286.
- [64] Lee, M. R., Miller, B. L. & Fauchet, P. M. Two-dimensional photonic crystal slot microcavity sensor for virus-sized particle detection. *Integr. Photonics Nanophotonics Res. Appl. ITuC4* (2008).
- [65] Endo, T., Ozawa, S., Okuda, N., Yanagida, Y., Tanaka, S. & Hatsuzawa, T. Reflectometric detection of influenza virus in human saliva using nanoimprint lithography-based flexible two-dimensional photonic crystal biosensor. *Sensors Actuators B Chem.* 148, 269–76 (2010).
- [66] Li, N., Cheng, X. R., Brahmendra, A., Prashar, A., Endo, T., Guyard, C., Terebiznik, M. & Kerman, K. Photonic crystals on copolymer film for bacteria detection. *Biosens. Bioelectron.* 41, 354–8 (2013).
- [67] Pal, S., Yadav, A. R., Lifson, M. A., Baker, J. E., Fauchet, P. M. & Miller, B. L. Selective virus detection in complex sample matrices with photonic crystal optical cavities. *Biosens. Bioelectron.* 44, 229–34 (2013).
- [68] Feng Liang, Nigel Clarke, Parth Patel, Marko Loncar, and Qimin Quan, "Scalable photonic crystal chips for high sensitivity protein detection," *Opt. Express* 21, 32306-32312 (2013).
- [69] Konopsky, V.N. and Alieva, E.V., 2007. Photonic crystal surface waves for optical biosensors. *Analytical chemistry*, 79(12), pp.4729-4735.
- [70] He LN, Ozdemir S,K, Zhu JG, Kim W, Yang L. Detecting single viruses and nanoparticles using whispering gallery microlasers. *Nat Nanotechnol* 2011; 6: 428–432.
- [71] Vollmer F, Arnold S, Keng D. Single virus detection from the reactive shift of a whispering-gallery mode. *Proc Natl Acad Sci USA* 2008; 105: 20701–20704.

- 
- [72] Zhu JG, Ozdemir S,K, He LN, Chen DR, Yang L. Single virus and nanoparticle size spectrometry by whispering-gallery-mode microcavities. *Opt Express* 2011; 19: 16195–16206.
- [73] Quan, Q., Floyd, D.L., Burgess, I.B., Deotare, P.B., Frank, I.W., Tang, S.K., Ilic, R. and Loncar, M., 2013. Single particle detection in CMOS compatible photonic crystal nanobeam cavities. *Optics Express*, 21(26), pp.32225-32233.
- [74] Liang, F. and Quan, Q., 2015. Detecting single gold nanoparticles (1.8 nm) with ultrahigh-Q air-mode photonic crystal nanobeam cavities. *Acs Photonics*, 2(12), pp.1692-1697.



# 2

## Planar photonic crystal cavities

This chapter is divided into three sections. First, a brief introduction about photonic crystal (PhC) structures with emphasis on 2D PhC slabs is provided. In the next subsection, focus is made on defects in PhC slab and their design consideration during DUV fabrication. Finally, in the last section of this chapter, a conclusion is provided.

This chapter introduces the basic concepts related to photonic crystal (PhC) in a brief manner. Photonic bandgap effects, cavity defect mode formation and waveguide defects are explained and illustrated.

Two distinct features of photonic crystals distinguish them from bulk dielectric media: the presence of a photonic band-gap, and optical modes with group velocities that can be much lower than the velocity of light in bulk media. In this chapter, the formalism used to quantify light propagation in photonic crystals is described, by means of which, the presence of a photonic band-gap in such structures is explained. Computational tools are then introduced and used to calculate dispersion relations for photonic crystals. After noting practical issues relating to viable geometries, cavity construction using photonic crystals is outlined. A discussion of the mechanisms for cavity-Q enhancement follows, and finally the cavity geometries studied in this thesis are described.

## 2.1 Classification of PhC structures

Photonic crystals (PhC) are photonic structures characterized by a periodic modulation of the refractive index that is of the same order of magnitude as the wavelength of the light that interacts with them. When an electromagnetic wave is incident on a 1D, 2D or 3D periodic structures, it undergoes partial scattering at each dielectric interface. The resulting multiple scattering phenomenon gives rise to a range of electromagnetic frequencies for which light propagation is prohibited in one or several directions. Such a frequency range is called photonic bandgap. The existence of photonic band gap gives rise to a number of interesting and useful properties including the localization of light at defects and surfaces and the inhibition of radiation.

An example of 1D PhC structure is a dielectric Bragg mirror (DBR) (**Figure 2(a)**), which is formed using alternative layers of different refractive index ( $n$ ). Each layer has thickness of one quarter of the desired incident wavelength ( $\lambda$ ), i.e.,  $\lambda/4n$ . Such mirrors can provide reflectivity over 99.99%. These Bragg reflectors finds application in DBR lasers, distributed feedback (DFB) lasers and vertical cavity surface emitting laser (VCSEL).

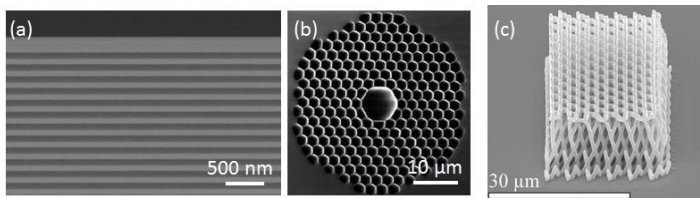


**Figure 2.1:** SEM images of one-, two-, and three-dimensional PhCs. (a) 1D: Bragg mirror reproduced from [1], (b) 2D: Microstructured fiber reproduced from [2], (c) 3D: Yablonovite structure reproduced from [3].

If the periodicity is two dimensional (2D), we talk about 2D PhC. Strictly speaking, these structures are assumed to be infinitely long in the direction perpendicular to the plane in which 2D periodicity exists. One of the most interesting applications of 2D PhCs is photonic crystal fiber (**Figure 2.1(b)**). In such a structure, light is confined to the core by the photonic band gap (PBG) and propagates through the fiber, along the PhC holes.

By introducing spatial periodicity in all three dimensions, real three-dimensional (3D) PhC can be realized (**Figure 2.1(c)**). The advantage of 3D PhCs is that they can control the propagation of light in all three dimensions and even enable a photonic bandgap in all the direction of the space. It should be noted that full photonic bandgap exists in only a few types of 3D PhC. These structures can be

realized using standard etching techniques, multiple thin-film deposition techniques, self-assembly, micromanipulation, etc.

Fabrication of 3D PhC structures is still a difficult process, and hence limits the types of possible structures (lattice symmetry, materials etc.). A more appealing approach was introduced based on the use of lower-dimensional PhCs. A structure that has recently attracted a lot of attention is a semiconductor slab perforated with a 2D lattice of holes (**Figure 2.2**).

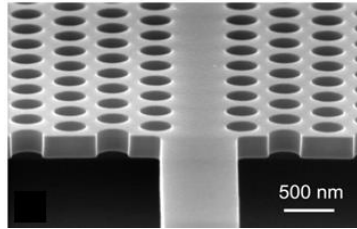


**Figure 2.2:** Planar photonic crystal waveguide fabricated in silicon membrane suspended in air, reproduced from [4].

The big advantage of such planar PhC is their fabrication procedure, which is compatible with current standard planar technology used to construct microelectronic devices. The size of nanophotonic devices based on the planar PhC concept is comparable to the wavelength of the light in the material and therefore it is possible to realize functional photonics components that are at least an order of magnitude smaller than conventional devices. Therefore, planar PhC devices offer the promise to replace conventional photonics in highly integrated optical systems. Planar PhCs show even greater promise for the realization of devices that cannot be made using a conventional approach. Highly dispersive super-prism [5] and self-collimators are some examples of using the unusual dispersion characteristics of PhCs. However, one of the most attractive planar PhC devices is a compact and resonant nanocavity with high quality (Q) factor. This is due to extraordinary feature of planar PhCs to localize high electromagnetic fields into very small volumes for long periods of time.

In this thesis, I focused specifically on 2D silicon membranes in which the PhC structure was defined by a triangular lattice of holes. The choice of the triangular lattice of holes over other configurations (for example, a square lattice of holes) comes from its higher degree of symmetry, which allows for a complete omnidirectional bandgap (in silicon) for the Transverse-Electric (TE) polarization.

## 2.2 Band diagram and photonic bandgap

The properties of the PhC structures with respect to the light propagation can be described in the form of a band diagram or dispersion diagram. The photonic band diagram represents the dispersion relation between the wave vector  $k$  of the eigen modes of the photonic structure and the angular frequency  $\omega$  of the periodic electromagnetic field configurations. The eigen modes are called Bloch modes.

In order to understand the salient features of PhC structures, we will focus on the 1D PhC that exhibits periodic RI modulation in one direction  $y$  (see **Figure 2.3**) and remains homogeneous in the two other directions. Such a structure is formed by a dielectric unit cell that is repeated along  $y$  with the basic step given by the lattice constant  $a$ :  $\varepsilon(y) = \varepsilon(y+a) = \varepsilon(y+ma)$ , where  $m$  is an integer and  $\varepsilon$  is the dielectric constant. This implies that the structure has a discrete translational symmetry in the  $y$ -direction. According to the Bloch-Floquet theorem [6], such discrete translational symmetry implies an electromagnetic wave solution called Bloch mode in the form of  $\vec{E}(\vec{y}) = \vec{u}(\vec{y})e^{i\vec{k}\cdot\vec{y}}$ , where  $\vec{u}(\vec{y})$  is a periodic (Bloch) function, and  $\vec{k}$  is the wavenumber.

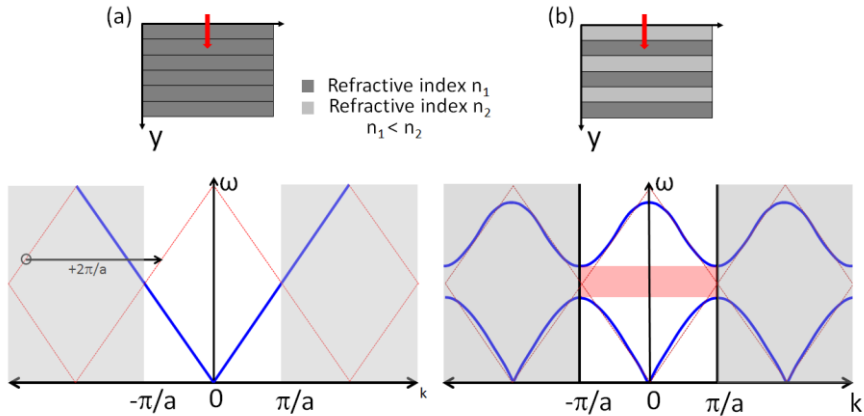


**Figure 2.3:** (a) Band folding in a periodic ‘empty’ lattice. (b) bandgap is formed when the refractive index contrast is introduced.

Let us consider the case of a plane wave with wavevector  $\vec{k}$  impinging at normal incidence on a Bragg mirror with period  $a$  (see **Figure 2.3**). Because of the periodicity in  $y$ -direction, the electromagnetic modes of the stack can be characterized by the wavevector  $k_y$ , with  $k_y$  restricted to  $-\pi/a < k_y < \pi/a$ , called the first Brillouin zone.

The superposition of the incident wave ( $k_y = \pi/a$ ) and the reflected wave ( $k_y = -\pi/a$ ) results in a standing wave pattern. The coupling of the two counter-propagating waves (with the same energy  $\omega_0$ ) by the reciprocal vector  $G = 2\pi/a$  results in a band-splitting that removes the degeneracy and generates two states at frequencies  $\omega_1$  and  $\omega_2$ . The width of the bandgap gets larger as the contrast in permittivity increases. The propagating modes on the lower side of the PBG correspond to a state where the electric field is mainly located in the higher refractive index layers, while the modes on the upper side of the PBG correspond to a state where the electric field is mainly located in the lower refractive index layers. As a consequence, the region located below the PBG is commonly referred to as "dielectric band" while the region located above the PBG is referred to as the "air band".

## 2.3 Planar photonic crystal

One typical example of a planar PhC is the perforated membrane shown in **Figure 2.2**. An optically thin semiconductor slab (of thickness  $\approx \lambda/2n$ ) is surrounded with a lower refractive index material (usually air) and patterned with a 2D lattice of holes. In planar PhC, the localization of light in all three dimensions is made possible by combining two mechanisms. In the vertical direction, light is confined to the slab by means of total internal reflection (TIR) resulting from the high-index-contrast between the patterned dielectric slab and the low-index surrounding. In the lateral direction, the light propagation is controlled by Bragg reflection resulting from the presence of the periodic 2D lattice of holes.

In order to understand the guiding mechanism in a planar PhC, the light line is a very important concept to be considered. The notion of the light line is a useful tool to distinguish between guided and non-guided modes in dielectric slab waveguides. Also for more complicated structures with 2D mode confinement, the light lines can often be used to divide a dispersion diagram into a region of a non-guided continuum of modes, a region of discrete guided modes and a forbidden region, where no propagating modes can exist.

In order to plot the light line, index guiding (due to TIR) in a slab waveguide needs to be considered. TIR can be visualized by Snell-Descartes law which states that the refraction of a light ray at an interface between the core and the cladding of the waveguide, is described as:

$$n_1 \sin \theta_1 = n_2 \sin \theta_2 \quad (2.1)$$

where  $n_1$  and  $n_2$  is the refractive index of core and cladding respectively;  $\theta_1$  and  $\theta_2$  are angle of incidence and refraction at the core cladding interface respectively.

A mode can be guided in the waveguide when  $\sin \theta_2 \geq 1$  and exists only for  $n_2 < n_1$ . Snell-Descartes law is a consequence of the conservation of the component  $k_{\parallel}$  of the wavevector  $k$  in the plane parallel to the interface. For a given frequency  $\omega$ , only the modes with  $|k| \leq n_2\omega/c$  can propagate in the cladding.

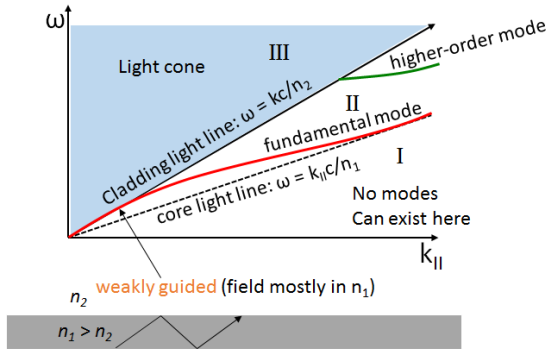


**Figure 2.4:** Guided mode dispersion of TE modes in a dielectric slab.

Let us consider the dispersion relation of a simple slab waveguide with refractive index  $n_1$  surrounded by a medium with index  $n_2 < n_1$ . The dispersion diagram is actually divided into three distinct regions (see **Figure 2.4**): (I) In the region below the light line of the core no modes can exist. (II) Between the core and the cladding light line the truly guided modes can be excited. They exhibit very low propagation losses (due to material absorption and/or residual structural disorder) and their field profile decays exponentially into the cladding. (III) The region above the cladding light line, namely the light cone, comprises a continuum of radiative modes.

In case of a planar PhC as shown in **Figure 2.2**, the third dimension is neither periodic nor infinite. **Figure 2.5** shows the dispersion diagram of a planar PhC in 220 nm thick silicon membrane with a triangular lattice of holes. The region above the light line, where leaky modes exist, is represented as the blue region. Since the radiative modes exist at all frequencies, including the bandgap region, and thus a complete bandgap is no longer found in such planar PhCs. However, the forbidden frequency range remains for the guided modes within the slab. Any defects introduced into the photonic crystal lattice can now couple propagating guided modes to radiative modes and scatter light from the slab. These defects can either be intentional, in the form of missing holes for example, or unintentional, resulting from fabrication imperfections. These two kind of enhance the mode coupling to leaky modes and increase the photonic crystal

losses. Clearly, care needs to be taken when designing and fabricating photonic crystals to minimize undesired losses.

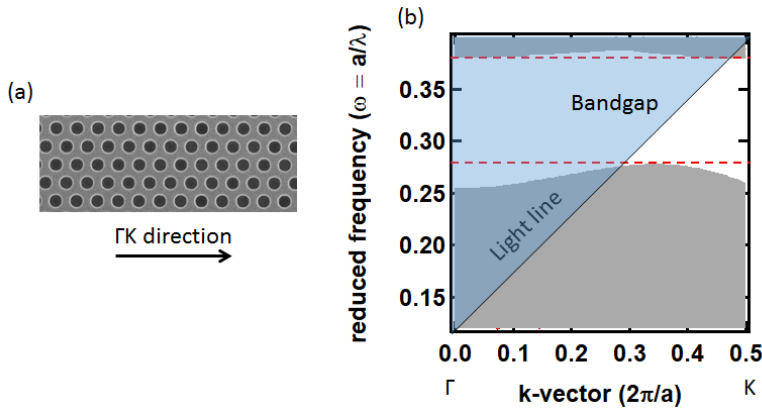


**Figure 2.5:** (a) Schematic of silicon based PhC structure with a triangular lattice (b) Dispersion diagram of silicon based planar PhC with the air and dielectric bands enclosing the bandgap. Shaded blue area represents the air-light cone.

## 2.4 Photonic Crystal Waveguides

Guiding of optical radiation is possible with planar integrated waveguides that work on the basis of total internal reflection. In order to create a waveguide mode in a PhC, a row of holes can be removed which creates a line defect in the lattice [7]. For a convenient design of the defect, some of these states should be located within the band gap of the photonic crystal. Since light cannot propagate in the photonic crystal at this frequency, it is localized in the surrounding of the defect, i.e., the line defect acts as a waveguide. Depending on the number of rows that are removed, it can be labelled as a W1, W2 or Wn waveguide. In the case of a standard W1 waveguide with one row of holes removed, the spatially even-like mode falls into the bandgap from the air band as shown in the computed W1 band diagram in **Figure 2.6**.

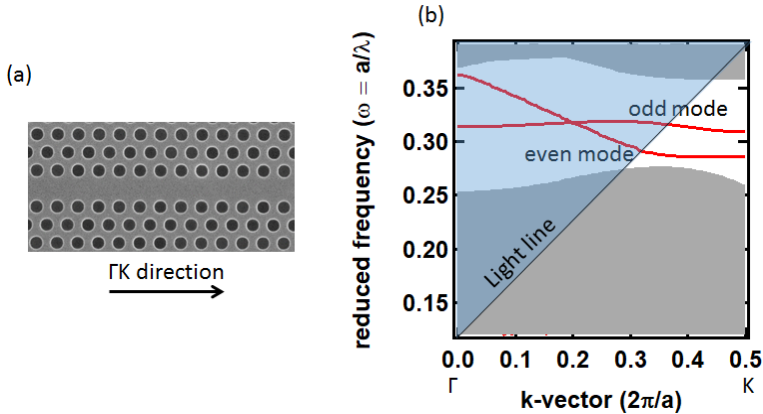


**Figure 2.6:** (a) Schematic of silicon based bulk PhC based W1 waveguide in triangular lattice (a) Dispersion diagram highlighting waveguide modes within a line defect photonic crystal.

## 2.5 Planar photonic crystal cavities

From a planar PhC structure, it is possible to realize compact and resonant optical cavities with high quality factors ( $Q$ ) and small mode volumes ( $V_{\text{mode}}$ ) by creating a defect. Moreover, PhC cavities can be engineered to concentrate a large fraction of the trapped mode in the low index material, and thus are natural candidates for the investigation of interaction between light and matter on a nanoscale level. Photonic crystal cavities can be formed by modifying one or more holes in the photonic crystal lattice. **Figure 2.7** shows the dispersion diagram of a silicon based planar PhC cavity.

The defect mode frequency increases as  $\epsilon_{\text{defect}}$  decreases. The first possibility to create a defect cavity consists in decreasing the size of a single hole from a perfect triangular lattice in a slab. This results in a local increase of the dielectric constant, i.e., a positive value for  $\Delta\epsilon$ . According to the perturbation theory [8], for such a positive value, the corresponding frequency shift is negative and a discrete mode can fall into the bandgap from the bottom of the upper air band. Another example of such type of cavity is a standard L3 cavity [9]. We have used various L3 based cavities throughout this thesis due to its robustness in fabrication and cavity excitation. The majority of the electromagnetic (EM) field in such cavity is localized in the high RI material. More info about these cavities will follow in next section.

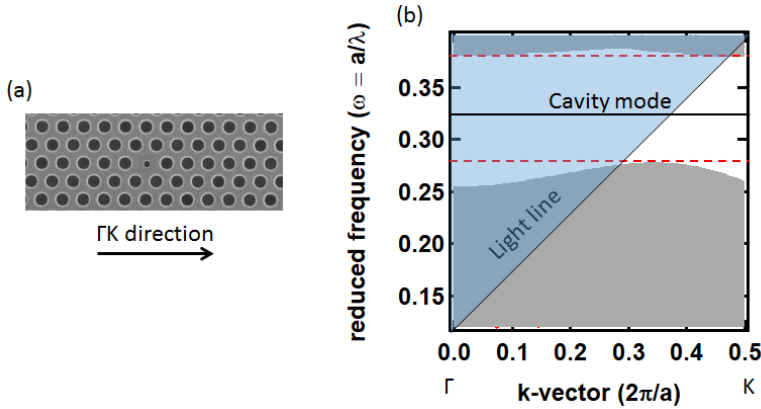


**Figure 2.7:** (a) Schematic of silicon based PhC cavity in triangular lattice  
 (b) Dispersion diagram highlighting the discrete state formation in the bandgap which occurs due to creation of a small defect by reducing the hole radius.

The second possibility is through an increase in the size of a single hole in the periodic lattice. This results in a decrease in the presence of dielectric content leading to a negative value of  $\Delta\epsilon$ . Perturbation theory shows that for such a negative value, the corresponding frequency shift is positive and a discrete mode arises out of the top of the lower dielectric band [8]. Air-slot based cavity falls under this type of classification where the main part of the EM field is confined in the low index material (air). More detailed description about design and fabrication of such cavities will follow in next section.

In the case of an ideal 2D infinite PhCs, light can be completely trapped at the defect. However, in optical cavities defined within photonic crystal slabs, modes also suffer from radiation losses through coupling into the continuum of radiation modes in the light cone. Since the cavity mode is localized in real space, it is extended in reciprocal space as governed by the Fourier transform properties. It therefore consists of  $k$ -vector components that are positioned within the light cone and these components contribute to the out-of-plane losses of the cavity. At the same time, light can leak laterally due to the limited number of the photonic crystal layers surrounding the cavity, contributing to the in-plane losses of the resonator.

The capability of a resonator to store light is quantified by its quality factor ( $Q$ ). For a given resonant mode of frequency  $\omega_0$ , the  $Q$  factor is defined by

$$Q = \omega_0 \frac{\text{stored energy}}{\text{power loss per cycle}} = -\omega_0 \frac{U}{dU/dt} \quad (2.2)$$

where  $\omega_0$  is the resonant frequency, and  $U$  is the energy stored in the cavity. Therefore, an ideal cavity would have an infinite  $Q$ .

The real cavities are limited by losses, both due to radiation and absorption which decreases the lower  $Q$  factor. In order to improve the  $Q$  factor of a planar PhC based microcavity, one needs to significantly reduce the out-of-plane (vertical) losses from these structures, while maintaining or even improving upon the in-plane losses. In case of a planar PhC surrounded by a medium with refractive index  $n_{\text{clad}}$ , the optical mode confinement inside the slab is only possible if the vertical component of the wave vector i.e.  $\vec{k}_z$  is imaginary outside the slab. Therefore, we can define a condition for which the optical confinement in the structure is possible,

$$k_{\text{in-plane}} = \sqrt{k_x^2 + k_y^2} > n_{\text{clad}}\omega/c \quad (2.3)$$

If we go back to the dispersion curve corresponding to the point defect cavity (**Figure 2.7**), we notice that a large section of this “band” lies within the light cone, which implies that the cavity mode contains plane wave components with in-plane wave vectors that do not satisfy the condition in equation 2.3. As a result, although the cavity mode is perfectly confined in the  $xy$  plane by the in-plane photonic band gap, its energy will be lost due to vertical radiation.

Susumu Noda’s group [9] reported a general design recipe for the realization of high- $Q$  nanocavities in 2D PhC slabs: To suppress radiation loss, the envelope of the cavity mode field should follow a Gaussian function, and the field profile should vary smoothly and gently [9]. The strategy is simple: if the cavity mode is concentrated outside the light cone of air in the 2D  $k$  space, the cavity mode cannot be coupled to the radiation modes. At the same time the mode is kept as confined as possible, thanks to the fact that Gaussian function are Fourier transform limited:  $\Delta k \cdot \Delta x = 2\pi$ .

It has to be noted that different loss mechanism can affect the  $Q$ -factor of a planar PhC cavity. The  $Q$ -factor can be expressed as:

$$\frac{1}{Q} = \frac{1}{Q_{\text{radiative}}} + \frac{1}{Q_{\text{absorptive}}} + \frac{1}{Q_{\text{disorder}}} + \frac{1}{Q_{\text{coupling}}} \quad (2.4)$$

where  $Q_{radiative}$  and  $Q_{absorptive}$  denotes the radiative and absorptive losses associated to the cavity and material system respectively and  $Q_{disorder}$  denotes the increase in the losses due to the presence of structural disorder.  $Q_{coupling}$  on the other hand, depends on how light can be coupled into the cavity mode. A waveguide, for instance, can be used to couple the light into the microcavity through evanescent coupling and the coupling strength can also influence the measured Q-factors.

If a finite amount of energy is injected into the system at time,  $t = 0$ , the total energy decay can be monitored in time and the number of oscillations for this field decay can be determined. This is also one of the preferred methods used in certain numerical methods such as FDTD to determine the Q factor. The Fourier transform of such a time decaying field is given by a Lorentzian function as follows:

$$S = \frac{1}{(\omega - \omega_0)^2 + (\omega_0/2Q)^2} \quad (2.5)$$

It implies that the full width at half maximum of the cavity spectrum can be used to directly estimate the Q factor.

This definition is convenient to retrieve the value of Q-factor from experimental or simulated cavity transmission spectra:

$$Q = \frac{\omega_0}{\Delta\omega} = \frac{\lambda_0}{\Delta\lambda} \quad (2.6)$$

where  $\Delta\omega$  is the full-width at half-maximum (FWHM) of the resonant power spectrum.

### 2.5.1 L3 based PhC cavities

A standard L3 cavity is defined by removing 3 adjacent holes in the  $\Gamma$ -K direction of a triangular lattice of holes. **Figure 2.8(a)** shows the SEM image of a standard L3 cavity. The Q factor of such cavity is around 4000. Fabrication of such cavities is feasible by a standard DUV lithography.

The Q factor of a standard L3 can be increased by laterally shifting the holes and by varying the hole dimeter. Akahane et.al. [9] proposed one of such design, where 3 holes along  $\Gamma$ K direction on the both sides of cavity are laterally shifted away from the core by a length of  $(0.2a, 0.025a, 0.2a)$ , where  $a$  is the lattice

constant of the cavity. Lai et.al. [10] also proposed another L3 cavity based design where five nearest edge holes are outward shifted along the cavity axis ( $\Gamma$ K symmetry direction of the triangular lattice) by  $0.3370a$ ,  $0.2706a$ ,  $0.0874a$ ,  $0.3223a$ ,  $0.1737a$ , symmetrically on both sides of the cavity. The realization of such cavities using a standard DUV lithography is hardly possible. The reason is that the interhole spacing of the displaced holes in above mentioned cavity structure can be as small as 70 nm while the minimum interhole spacing that can be realized by a standard DUV lithography is limited to 150 nm. Nevertheless, it is possible to fabricate PhC cavities with such critical dimension on wafer scale by making use of 193 nm immersion lithography.

Immersion lithography [11] is a photolithography resolution enhancement technique for manufacturing integrated circuits (ICs) that replaces the usual air gap between the final lens and the wafer surface with a liquid medium that has a refractive index greater than one. The resolution is increased by a factor equal to the refractive index of the liquid. Current immersion lithography tools use highly purified water for this liquid, achieving feature sizes below 45 nanometers.

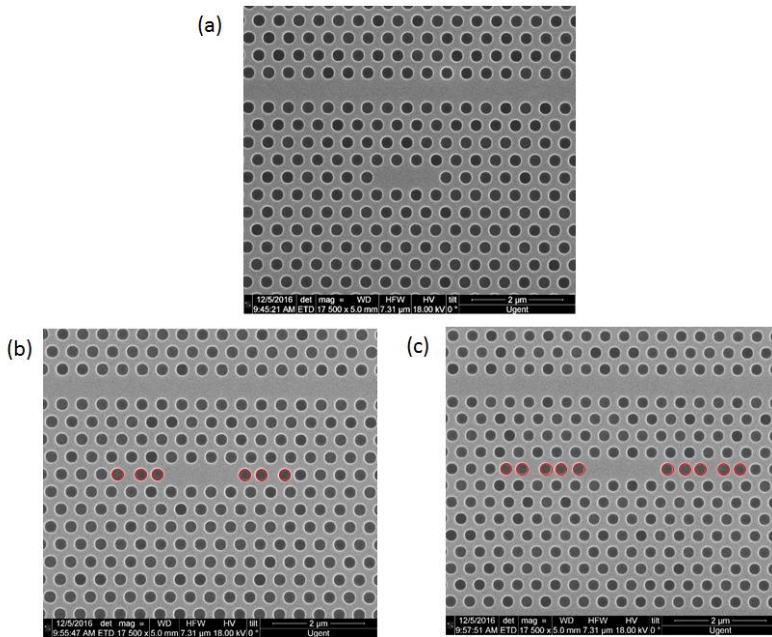


**Figure 2.8:** SEM image of cavity fabricated using 193 nm immersion lithography: (a) standard L3 cavity, (b) L3 cavity based on Noda's proposed design and (c) Savona's proposed design. Red circle represents the hole which has been displaced.

For one batch of samples, we had access to immersion lithography. It must be noted that the offset in hole diameter and slot width between designed and fabricated PhC structures was as low as 2 nm (limited by SEM accuracy). The experimental characterization of all the above cavities will be discussed in next chapter.

### 2.5.2 Hollow core based PhC cavities

Almeida and co-workers [12] have shown that light can be confined within a narrow slot etched inside a waveguide. In subsequent works [13,14], this concept was taken and implemented within a standard W1 photonic crystal waveguide. Such waveguide is theoretically expected to have a lossless mode with an extremely small modal area [12].

Such kind of structures are advantageous to light-matter interaction experiments as the majority of the electric field is confined in the low refractive index medium. The physical mechanism can be simply understood as the local field enhancement at dielectric boundaries. Generally, the electric field of the TE mode in the PhC cavity is mainly x-polarized (see **Figure 2.9**), so that the boundary condition for the electric field

$$\varepsilon E_x(r_{in}) = \varepsilon_0 E_x(r_{out}) \quad (2.7)$$

holds at the surfaces of the air-slot walls. Here,  $r_{in}$  and  $r_{out}$  represent slightly apart positions inside and outside the slot, respectively. Therefore,  $E_x(r_{out})$  is enhanced by a factor of  $\varepsilon/\varepsilon_0$  compared with  $E_x(r_{in})$ .

To create a slot based PhC cavity, one can either modify the dimensions of the slot itself or the properties of the PhC mirror. The first approach was adopted by Jagerska *et al.* [15], who locally reduced the air slot width by 20 nm to delimit the volume of the cavity, as shown in **Figure 2.9(a)**. A reduced slot width results in the formation of reflective barriers for the cavity mode. **Figure 2.10** shows the dispersion plot from to study the dependence of the dispersion curve on the slot width varying from 70 nm to 160 nm. If the slot width is below 70 nm, the slot mode is found within the dielectric band and is not fully guided within the plane. However, further increase of the slot width induces a rapid shift of the mode cutoff towards the upper air band, which is correlated to the increase of the slope of the linear part of the dispersion curve. Such a high sensitivity of the dispersion to the slit width results in high sensitivity of the device to disorder and an accentuated need for high precision fabrication.

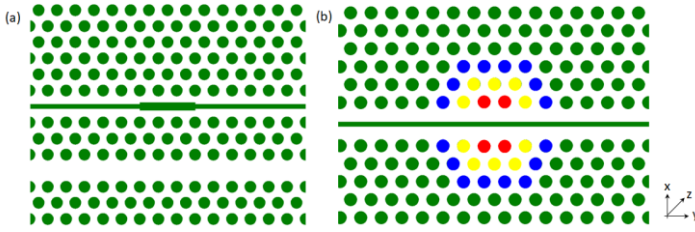


**Figure 2.9:** The layout of a PhC where a linear sub-wavelength-wide air slot is introduced in the center of the line defect and cavity is realized by (a) increasing the slot width from (100 nm to 120 nm) at the center of PhC structure, (b) by a local line-defect-width modulation via transversally shifting holes away from the slot. Air holes colored red, yellow, and blue are shifted outward by 15 nm, 10 nm, and 5 nm, respectively.

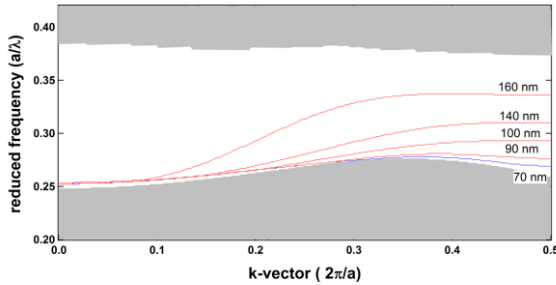


**Figure 2.10:** Change in the slot waveguide mode dispersion upon increasing the slit width from 70 to 160 nm.

The second approach for slot cavity was realized by two methods. A. Di Falco and coworkers [16], locally reduced the lattice constant of the photonic crystal to create a heterostructure cavity, while Yamamoto *et al.* [17] (Figure 2.9(b)) and Gao *et al.* [18], shifted the holes adjacent to the slot to form a width-modulated line-defect cavity. As reported by Yamamoto *et al.* (Figure 2.7(b)), a linear air slot is introduced in the center of the line defect of a mode-gap confined PhC cavity, which is realized by local width modulation of a line-defect width [17]. Without the width modulation, the structure is nothing but a slot waveguide. In this design, the light confinement is achieved by the gradual width modulation of the PhC waveguide, which can strongly suppress vertical radiation loss. Note that, in order to obtain maximum enhancement, the slot width  $s$  should be infinitesimally narrow because the new cavity mode after the introduction of such a narrow slot is almost the same as the original one. As a result, the strongest electric field of the original (slot-less) cavity can be enhanced further by introducing the air slot [19]. In contrast, for larger slot width, the maximum of the

electric field is shifted toward the inside of the PhC material, thus decreasing the field strength at the slot boundaries.

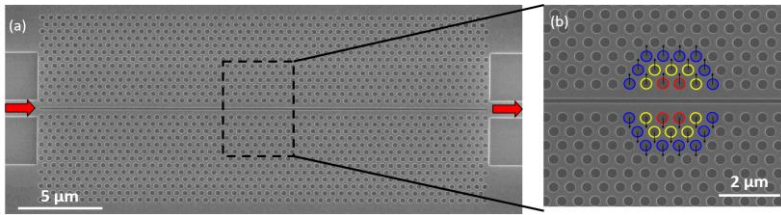


**Figure 2.11:** (a) SEM image of air-slot cavity, (b) zoomed in SEM image of slot cavity highlighting the shifting of holes denoted by the black arrows (red: 15 nm; yellow: 10 nm; blue: 5 nm).

The SEM images of the fabricated slot cavities based on Yamamoto's reported design is shown in **Figure 2.11**. Such structures are also fabricated using DUV lithography at imec. The circle highlights the holes which were shifted to realize the slot cavity. The red, yellow and blue circle were shifted by 15 nm, 10 nm and 5 nm respectively. For the fabrication of slot cavities with even narrower width, immersion lithography was used. The characterization of such cavity will be discussed in next chapter.

## 2.6 Conclusions

This chapter presented a brief introduction to PhC structures, with emphasis on 2D PhC slabs. Focus was made on the point and line defects in a silicon based PhC slab and their design consideration during DUV fabrication. Silicon based PhC cavities were classified in two types where light is concentrated in either a high index material (silicon) or a low index material (air). The notion of the light cone has been introduced. The dispersion relations for PhC structures were also discussed.

## References

- [1] [http://anff-act.anu.edu.au/HTML/News\\_detail/nl22\\_art2.html](http://anff-act.anu.edu.au/HTML/News_detail/nl22_art2.html)
- [2] <http://spie.org/newsroom/1371-photonic-crystal-fiber-characteristics-benefit-numerous-applications?SSO=1>
- [3] Rybin, M.V., Shishkin, I.I., Samusev, K.B., Belov, P.A., Kivshar, Y.S., Kiyani, R.V., Chichkov, B.N. and Limonov, M.F., 2015. Band structure of photonic crystals fabricated by two-photon polymerization. *Crystals*, 5(1), pp.61-73.

- [4] McNab, S.J., Moll, N. and Vlasov, Y.A., 2003. Ultra-low loss photonic integrated circuit with membrane-type photonic crystal waveguides. *Optics express*, 11(22), pp.2927-2939.
- [5] Glöckler, F., Peters, S., Lemmer, U. and Gerken, M., 2007. Tunable superprism effect in photonic crystals. *physica status solidi (a)*, 204(11), pp.3790-3804.
- [6] Savona, V., 2011. Electromagnetic modes of a disordered photonic crystal. *Physical Review B*, 83(8), p.085301.
- [7] Johnson, S.G., Villeneuve, P.R., Fan, S. and Joannopoulos, J.D., 2000. Linear waveguides in photonic-crystal slabs. *Physical Review B*, 62(12), p.8212.
- [8] Joannopoulos, J.D., Johnson, S.G., Winn, J.N. and Meade, R.D., 2011. *Photonic crystals: molding the flow of light*. Princeton university press.
- [9] Akahane, Y., Asano, T., Song, B.S. and Noda, S., 2003. High-Q photonic nanocavity in a two-dimensional photonic crystal. *Nature*, 425(6961), p.944.
- [10] Lai, Y., Pirotta, S., Urbinati, G., Gerace, D., Minkov, M., Savona, V., Badolato, A. and Galli, M., 2014. Genetically designed L3 photonic crystal nanocavities with measured quality factor exceeding one million. *Applied Physics Letters*, 104(24), p.241101.
- [11] Switkes, M., Kunz, R.R., Rothschild, M., Sinta, R.F., Yeung, M. and Baek, S.Y., 2003. Extending optics to 50 nm and beyond with immersion lithography. *Journal of Vacuum Science & Technology B: Microelectronics and Nanometer Structures Processing, Measurement, and Phenomena*, 21(6), pp.2794-2799.
- [12] Almeida, V.R., Xu, Q., Barrios, C.A. and Lipson, M., 2004. Guiding and confining light in void nanostructure. *Optics letters*, 29(11), pp.1209-1211.
- [13] Di Falco, A., O'Faolain, L. and Krauss, T.F., 2008. Dispersion control and slow light in slotted photonic crystal waveguides. *Applied Physics Letters*, 92(8), p.083501.
- [14] Chen, X., Jiang, W., Chen, J., Gu, L. and Chen, R.T., 2007. 20 dB-enhanced coupling to slot photonic crystal waveguide using multimode interference coupler. *Applied Physics Letters*, 91(9), p.091111.
- [15] Jágerská, J., Zhang, H., Diao, Z., Le Thomas, N. and Houdré, R., 2010. Refractive index sensing with an air-slot photonic crystal nanocavity. *Optics letters*, 35(15), pp.2523-2525.
- [16] Di Falco, A., O'faolain, L. and Krauss, T.F., 2009. Chemical sensing in slotted photonic crystal heterostructure cavities. *Applied physics letters*, 94(6), p.063503.
- [17] Yamamoto, T., Notomi, M., Taniyama, H., Kuramochi, E., Yoshikawa, Y., Torii, Y. and Kuga, T., 2008. Design of a high-Q air-slot cavity based on a width-modulated line-defect in a photonic crystal slab. *Optics express*, 16(18), pp.13809-13817.
- [18] Gao, J., McMillan, J.F., Wu, M.C., Zheng, J., Assefa, S. and Wong, C.W., 2010. Demonstration of an air-slot mode-gap confined photonic crystal slab nanocavity with ultrasmall mode volumes. *Applied Physics Letters*, 96(5), p.051123.
- [19] Kuramochi, E., Notomi, M., Mitsugi, S., Shinya, A., Tanabe, T. and Watanabe, T., 2006. Ultrahigh-Q photonic crystal nanocavities realized by

the local width modulation of a line defect. Applied physics letters, 88(4), p.041112.



# 3

## Wafer scale fabrication of PhC cavities

Substrate-less free-standing PhC cavities allowing access from both sides of the cavity membrane enable the transportation of analytes and simultaneous detection of signal variation induced by the analytes. In order to achieve a substrate-less free-standing PhC cavities, a significant number of post-processing steps is required. Therefore, I have developed a complete methodology to post-process a large array of 2D PhC membrane. Furthermore, when the substrate is removed, a nanometer sized tip can be conveniently positioned near the PhC cavity and emulate the effect of a nano-object on the cavity field. In this chapter I will focus on the fabrication of complementary metal-oxide-semiconductor (CMOS) compatible planar PhC cavities, their post processing steps and fabrication of silica fiber nano-tip. This chapter is adapted from the manuscript which we published in IEEE photonics Journal [1].

The organization of this chapter is as follows: In the first section, a short introduction to the Silicon-On-Insulator (SOI) platform is provided. The second part deals with the fabrication of 2D PhC slabs in SOI using Deep -Ultraviolet (DUV) lithography. This section also highlights the critical aspects that need to be considered in the mask design of PhC structures for its accurate fabrication. Moreover, it illustrates the complete process flow to fabricate substrate-less free-standing array of PhC cavities with integrated SU8 waveguide as spot size

converter. In the third section, the process steps to fabricate nanometer sized fiber tip starting from a standard single mode optical fiber (SMF 25) are described. The last section concludes the results of this chapter.

### 3.1 Silicon-On-Insulator platform

Silicon-On-Insulator (SOI) is rapidly emerging as a versatile platform for a variety of integrated nanophotonic components. Silicon and its oxide form high-index contrast, high-confinement waveguides. This is ideally suited for medium to high integration of photonic structure and small passive devices in their transparency wavelength range, including the most important 1300 and 1550 nm communication bands. One drawback of silicon is that it has an indirect band gap and this makes it very difficult to design active components (e.g. lasers or detectors). It is however possible to integrate silicon with other material systems which do allow for active components [2].

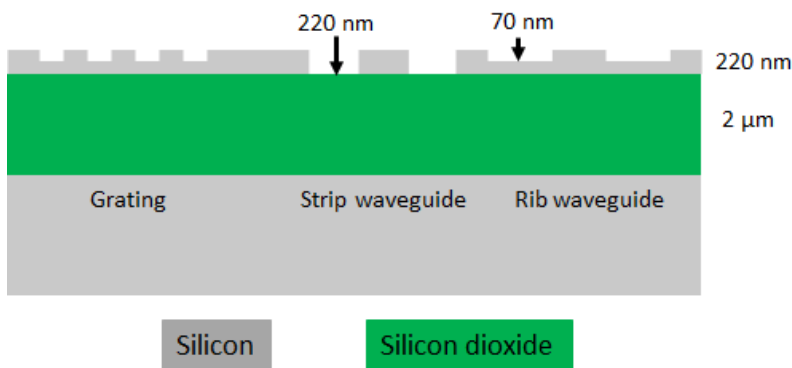


**Figure 3.1:** A full (220 nm) and shallow (70 nm) etch step is executed on the top silicon (device) layer using DUV lithography at imec.

In this thesis, the 200 mm pilot line fabrication facility at imec was used for wafer processing using DUV lithography at a wavelength of 193 nm [3]. The 8 inch wafers that were supplied to us by SOITEC consist of a three-layer stack. First a 220 nm top silicon layer in which photonic structures are etched. This crystalline silicon layer is located on top of a 2 μm buried silicon dioxide (SiO<sub>2</sub>) or, commonly referred to as buried oxide (BOX), which is supported by a 740 μm thick silicon substrate.

In order to fabricate PhC structures, a full silicon etch step (220 nm depth) is implemented on the DUV patterned top silicon (or device) layer as illustrated in

**Figure 3.1.** In some cases, another shallow silicon etch step (70 nm depth) is also carried out on the top device layer. In most cases, these two steps suffice to fabricate a photonic structure in silicon. After these two etching steps, normally no additional processing has to take place and all the dies of the wafer are ready to be used. But for our application, we needed to achieve a free access to the surface of the PhC membranes from the substrate side along and therefore, a series of post-processing had to be developed.

It should be noted that in the following sections, the work done during the PhD project has been carried out on single chips, diced from an entire wafer, since the total number of wafers at our disposal was limited. However, none of the following steps are inherently chip-based and are all applicable in principle on a wafer scale.

## 3.2 Fabrication of 2D photonic crystal slabs

Regardless of the specific material substrate, the general process of fabrication is similar for all semiconductor slab-PhCs. The PhC pattern is first written using some form of lithography before being transferred to the device layer via an etching technique. The most common method used for the patterning of PhC sensor is electron beam (e-beam) lithography. E-beam lithography is commonly used in literature-reported devices despite its relatively high cost and slow speed. This is due to its versatility in the prototyping process as no expensive photolithography masks need to be prepared. An e-beam-sensitive resist is first deposited on the substrate surface, and then a focused beam of electrons is used to write a pattern by serially scanning across desired pattern areas. Photolithography is another exposure method that can be used for pattern writing. In this parallel process, the pattern is first defined in a photomask. UV light is shined on the mask, and light transmitted through the mask interacts with the resist to either strengthen or weaken the material. Photolithography is more efficient and significantly cheaper for mass production, and thus can be produced for commercial distribution scales which is not possible with e-beam lithography. Silicon-on-Insulator (SOI) technological platform represents undoubtedly the most suitable platform due to its CMOS compatibility for fabricating ultra-compact and ultra-high performance PhC based integrated sensors. DUV lithography is the continuation of the optical lithography into the deep UV wavelengths range. With an illumination wavelength of 193 nm, this technique offers both the resolution and the speed required for the mass manufacturing of PICs with sub-micrometer features.

**Figure 3.2** compares photonic crystal holes with waveguide lines as a function of lithography exposure dose [4]. With increasing dose, the lines (width of the silicon

waveguide) shrink and diameter of the holes grow. Therefore, to pattern both the structures together on target, a bias must be applied to one or the other on the mask. Where a bias is still necessary, it should be applied directly on the mask at the design stage.

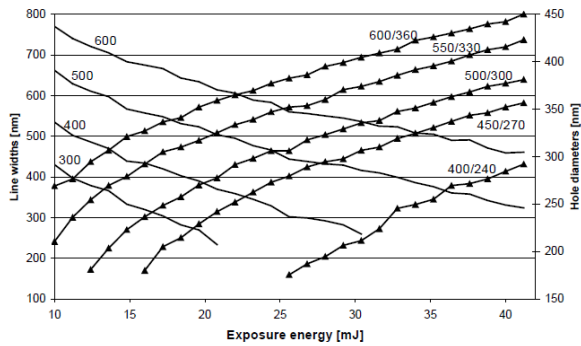


**Figure 3.2:** Hole diameters and line widths as a function of lithography exposure dose. Markers: hexagonal lattices of holes, marked with design pitch and diameter. Lines: Lines marked with design line width.

Reproduced from [4].

In our case, where the PhC structures were fabricated with a fixed exposure dose using the standard 193 nm DUV lithography, patterned PhC holes had smaller diameter than the designed ones. This shrinkage of holes occurred in this process because the exposure dose is standardized for a ridge waveguide of 450 nm width. Therefore in order to fabricate the PhC structure with desired dimensions, bias values must be added to the designed dimension of holes. To obtain these bias values, PhC structures with hole diameter varying from 130 nm to 350 nm were designed. The fabricated PhC holes were investigated via Scanning Electron Microscope (SEM) images and were compared to the dimensions of the designed ones. In the similar manner, the width of the air-slot inside PhC structures is varied from 120 nm to 160 nm. **Figure 3.3** shows the plot of the diameter of designed vs fabricated PhC holes and designed slots vs fabricated slots. The error bar considers the accuracy of the SEM measurement which is around 3 nm. This plot was used as a bias chart for the fabrication of the PhC structures that have been investigated in this thesis using DUV lithography.

Once the patterning of PhC structure is done, it is necessary to remove the BOX layer below PhC membrane. The presence of the BOX layer underneath a PhC partially decreases the light confinement in the structures and creates an imbalance in the symmetry of the device. So, the BOX layer needs to be removed below the PhC structure. This is done by a wet etching in Buffered-Hydrofluoric (BHF) acid through the PhC holes. First, the PhC chip is spin coated with an

adhesion promoter (Ti prime) and then with a second negative photoresist (TI 35E). The obtained layer is then baked and exposed to UV light in a SUSS Microtec mask aligner through a chromium mask. After careful alignment and exposure, the photoresist is developed in AZ400 and rinsed. This process leaves the chip completely protected by the photoresist except at the location of the PhC structures. The chip is then immersed in a BHF solution. This wet etching step underetches the sacrificial  $\text{SiO}_2$  layer, leaving the photonic crystal membrane fully suspended. Finally, the photoresist is stripped off and the chip is dried in a critical point drier in order to avoid any damage caused by surface tension forces during water evaporation.

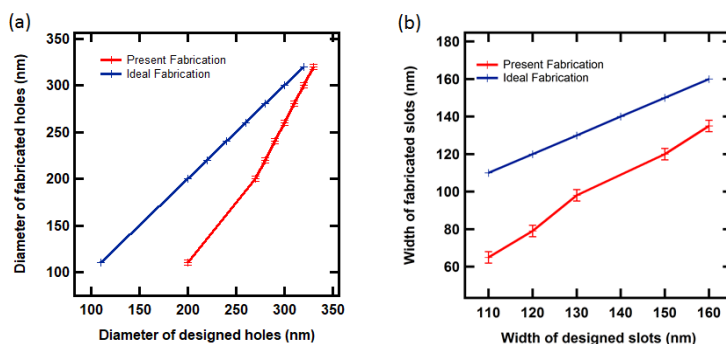


**Figure 3.3:** Plot of deviation in fabrication of diameter and slot width of PhC compared to the designed ones.

Removing only the BOX layer below the PhC makes the cavity free-standing already but it is difficult to access the cavity surface for analyte transportation as shown in **Figure 3.4(a)**. This difficulty arises when a detection system of high numerical aperture (NA) is used to optimize the signal to noise ratio. To solve the analyte transportation issue, the silicon substrate below the PhC cavity needs to be initially removed as shown in **Figure 3.4(b)**. The red colored droplet below PhC cavity in **Figure 3.4(b)** represents a micro-droplet containing analytes. The resulting free-standing cavity without substrate eases up the analyte transportation to the cavity surface.

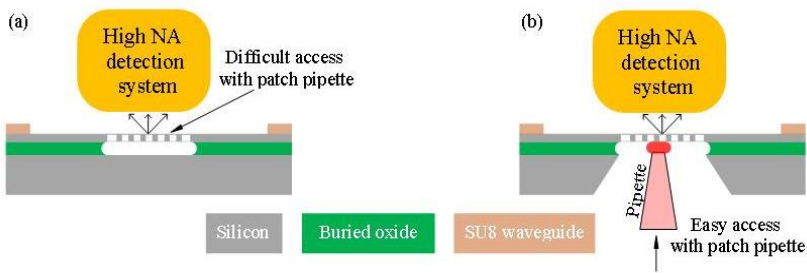


**Figure 3.4:** Schematic of an integrated PhC cavity cross-section (a) highlighting the congestion of the high NA signal detection system and (b) of the microdroplet transportation system of the analytes.

The next section will illustrate the process flow to fabricate substrate-less free-standing PhC cavities. The local substrate removal below the PhC was done in four steps: deposition of a thin film on the backside of a thinned and polished chip, which acts as a hard mask; a patterning on the hard mask layer to define the etching window by the contact photolithography; a wet etching in potassium hydroxide (KOH) solution to remove the silicon substrate; and BOX layer removal in BHF solution. **Figure 3.7** shows the schematic process flow illustrating major processing steps to fabricate substrate-less free-standing PhC membrane.

### 3.2.1 Anisotropic etching of silicon substrate

The etching of silicon has been investigated widely for over decades and is possible either by dry etching or wet etching as schematically illustrated in **Figure 3.5**. Dry etching of silicon is mainly done by placing the silicon substrate in a gas (plasma) chamber and utilizing a blend of a fluorine based gas (like  $\text{SF}_6$  or  $\text{CF}_4$ ) with other (like  $\text{O}_2$  or  $\text{N}_2\text{O}$ ) gasses. The main principle of this etching methodology relies upon generating a plasma of the precursor gasses that comes into contact with silicon. Fluorine ions are mainly responsible for the etching of silicon while addition of oxygen prevents recombination of fluorine ions with fluorosulphur radicals, which increases the net amount of fluorine ions and consequently increases the etch rate of silicon [5].

In general, dry etching process is preferred since it is possible to etch structures with a high level of anisotropy (or high aspect ratio). Since, the dry etching process which is available in our cleanroom removes silicon very slow, we opted for wet etching. Wet etching of silicon can be done either isotropically or anisotropically. The demand of wet anisotropic etching in silicon bulk

micromachining is due to the formation of unique 3D structures depending on the silicon crystallographic orientation with various etchants. In addition, bulk micromachining using wet etching has the advantages of being lower in cost, having higher degree of selectivity and a faster etching rate in comparison to dry etching [6]. Due to these reasons, bulk micromachining using wet anisotropic etching has been intensively employed in MEMS technology over more than five decades.

For isotropic wet etch of silicon, a mixture of HF, HNO<sub>3</sub>, CH<sub>3</sub>COOH and deionized (DI) water is used while for anisotropic etching commonly used etchants are alkaline based aqueous potassium hydroxide (KOH) and tetramethylammonium hydroxide (TMAH) solution. Isotropic etch of silicon also removes unnecessary parts of the silicon substrate, which can compromise the mechanical integrity of the chip. More importantly, because the etching solution contains HF, once the silicon substrate has been removed, the solution will continue to etch through the buried oxide (BOX) layer. This implies that not only the silicon dioxide layer will be removed but the 220 nm thin top silicon layer will also be etched in a fraction of seconds which imposes a very precise timing.



**Figure 3.5:** Schematic of dry etching (left), isotropic wet etching (middle), and anisotropic etching (right) of Silicon.

Etchant used for anisotropic etch removes silicon with a high selectivity compared to silicon dioxide and hence this layer acts as etch stop layer. As a consequence, anisotropic etch does not require precise time monitoring. Moreover, since the etching profile in the anisotropic etch is determined by the crystalline planes of silicon due to different compactness of the crystal, we conserve much more material in the substrate, compared to an isotropic etch. More details about etching of different planes of silicon can be found in [6]. Due to all these reasons, anisotropic etch is advantageous over isotropic etch. For anisotropic etch of silicon, we have opted for KOH since it etches silicon faster than TMAH [7]. Also, use of TMAH was avoided as it is extremely destructive to tissue of the mucous membranes and upper respiratory tract, eyes, and skin [8]. KOH is an etchant which attacks silicon preferentially in the  $\langle 100 \rangle$  plane producing a characteristic V-etch with side walls that form a  $54.7^\circ$  angle with the surface.

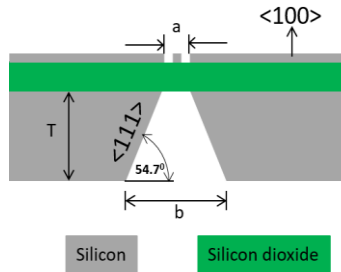


**Figure 3.6:** Anisotropic etching of  $\langle 100 \rangle$  silicon.

Since we wish to only etch certain parts of the silicon substrate, we need to apply a mask layer before etching. Due to the anisotropic nature of KOH etching, the dimension of the openings in the mask layer need to be much broader than the dimension of the required size of the opening near the buried oxide layer. From **Figure 3.6**, it can be calculated that the mask dimensions are equal to the opening size ‘ $a$ ’ multiplied by  $\sqrt{2}T$  where  $T$  is the substrate thickness.

We have used 20% KOH solution at  $80^\circ\text{C}$  to etch the silicon substrate, which removes silicon with an etch rate of  $1.3 \mu\text{m}/\text{min}$ . To illustrate: etching through the whole  $740 \mu\text{m}$  thick substrate will take approximately 9 hours. In order to decrease the etching time, the SOI chips is first thinned and then polished to  $200 \mu\text{m}$  thickness. In this case, the etching time gets substantially reduced to 2 hours and 30 minutes. The next sub-section explains the process flow to thinning and polishing of SOI chips in our cleanroom.

### 3.2.1 Lapping and polishing of silicon substrate

At first, we thinned down the chip to  $220 \mu\text{m}$  (see **Figure 3.7(b)**) by mechanically lapping the standard SOI chip. The backside of the chip is then polished by using a chemical slurry which contains  $30 \text{ nm}$  silica particle suspension.

We opted to remove approximately  $550 \mu\text{m}$  silicon substrate mechanically from a standard SOI chip which has an initial thickness of  $740 \mu\text{m}$ , using a PM5 Lapping Logitech machine. Thinning of the substrate is crucial as the mask layer deposited on top of the substrate might not survive in the silicon etchant for very long time and more importantly, the etching time will increase substantially for thick substrate. With this lapping machine as many as four chips of size around  $2.5 \text{ cm} \times 2.5 \text{ cm}$  can be easily thinned down simultaneously. A 12-inch radial grooved cast iron lapping plate was mounted on the machine and  $9 \mu\text{m}$  silica particle based chemical slurry was flown continuously over the plate from an abrasive autofeed cylinder. This plate was then conditioned by placing another 5-

inch grooved cast iron lapping plate on top of a 12-inch rotating plate at 70 rpm for 15 minutes. A weight and pressure block was placed on the top of the 5-inch grooved cast iron lapping plate to ensure good conditioning. This conditioning of the plate ensures uniform removal of the silicon substrate. The device layer of the four chips of size around 2.2 cm x 2.2 cm were spin coated with a 6  $\mu\text{m}$  thick photoresist (AZ 9260) in order to protect the structures from any probable scratches. These chips were then bonded on a thick glass plate using hot purple wax at 120  $^{\circ}\text{C}$ . The glass plate was then mounted on a logitech precision jig using vacuum and the jig was then placed on top of the iron plate. The chips were then thinned down in two successive steps while the plate was rotating at 60 rpm during this process. First, the chips were thinned down to 280  $\mu\text{m}$  using a 20  $\mu\text{m}$  silica particle based chemical slurry. Next, the chips were further thinned down to 220  $\mu\text{m}$  using a 9  $\mu\text{m}$  silica particle which helps in decreasing surface roughness. When the lapping process was finished, the glass plate was heated at 120 $^{\circ}\text{C}$  to remove the wax bonded chips. These chips once removed from the glass plate were immersed in purple wax solution to remove the wax. After removal of wax from chip surface, the chips were rinsed in acetone, isopropyl alcohol (IPA) and DI water.

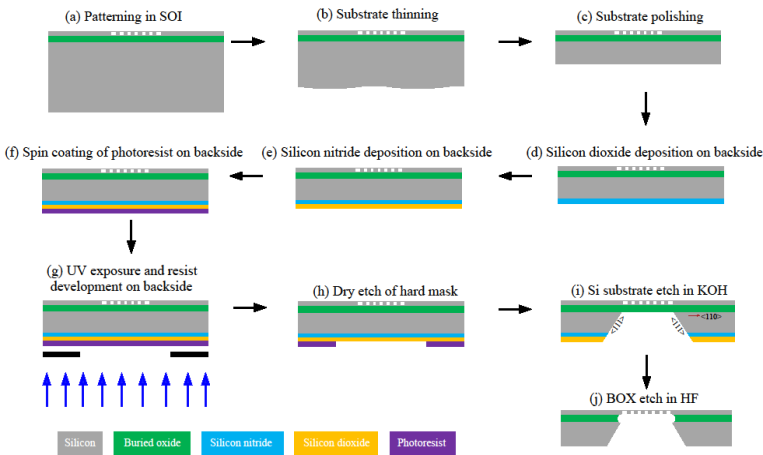


**Figure 3.7:** Schematic of process flow for fabrication of substrate-less free-standing PhC membrane. The top side of the chip was protected by placing the chip placed in a holder (see **Figure 3.8**).

These thinned chips were individually polished using a CMP presi machine. Each thinned chip was spin coated with a 6  $\mu\text{m}$  photoresist (AZ 9260) and bonded using a melted purple wax on a sample holder at 100 $^{\circ}\text{C}$ . Polishing of the substrate is done by applying a force on the sample head varying from 0-5 daN and rotating the polishing pad at 60 rpm. The chemical slurry used for polishing is a suspension

containing 30 nm silica particles which ensures high-quality polishing and strong adhesion of hard mask to the polished surface. The polished chip was removed from the sample holder by heating the holder at 120°C and immersing the polished chips in the purple wax solution. The polished chip was then rinsed in acetone, IPA and DI water.

### 3.2.2 Masking materials

Knowing the dimensions of the mask needed for the substrate etch, we need to choose an appropriate masking material. In this case, the use of a photoresist is not suitable as a masking material since it gets immediately removed by KOH in few seconds. One possible solution is to use silicon dioxide if the etching time is short (< 30 minutes for shallow etch) but for a through-chip etch (> 3 hours), this layer also gets etched away in KOH. For deep etch, silicon nitride layer must be employed which has a negligible (< 1 nm/hour) etch rate compared to silicon oxide (300 nm/hour) in 20% KOH solution [9]. But due to the lattice mismatch between silicon and silicon nitride layers, stress develops in the subsequent deposited layers. In this case an additional layer of silicon dioxide is deposited between silicon and silicon nitride. Here the silicon dioxide layer also acts as a buffer layer that minimizes the stress and improves adhesion on the polished backside. We have deposited a stack of 500 nm of silicon dioxide and mixed frequency low-stress 600 nm silicon nitride using plasma enhanced chemical vapor deposition (PECVD) [Figure 3.7(d-f)]. The mixed frequency silicon nitride deposition was done by changing the radio frequency (RF) generator frequency while using the same gas and power levels. In the mixed frequency PECVD process, both high (13.56 MHz signal) and low (100 KHz signal) RF frequency was applied alternatively for 6 second and 1 second, respectively. Adjusting the ion bombardment with high and low frequency mixture provides control over the film stress, film density and conformal properties [10]. This allows for densely stacked tensile and compressive layers.

### 3.2.3 Mask layer opening using photolithography

The photolithography process starts with a dehydration baking of the chip. Dehydration baking is performed to dry any excess moisture in the silicon substrate. In this process, all the chips are dehydration-baked on 150 °C hotplate for 30 minutes. To create openings in the mask layer for removing of the silicon substrate below the PhC cavity, we have to perform contact photolithography [Figure 3.7(g)]. We have spin coated a thick (3 µm) layer of a negative photoresist (e.g. AZ MicroChemicals TI 35E) on the substrate side of the chip and patterned the etching window using the backside alignment module of our Suss Mircotech

contact lithography tool. Cross and vernier markers located on the top layer of the chip ensures the high accuracy of the alignment of the photolithographic step. It should be noted that for precise alignment accuracy, the separation between the alignment markers should be more than 1.5 cm.

The hard mask of the patterned window is dry etched with  $\text{SF}_6$  and  $\text{O}_2$  gases in a Reactive Ion Etching (RIE) chamber. Generally, in a contact mask there are various other structures near the patterned window of interest which will also get etched in RIE and as a result all these structures will be susceptible to KOH. This means that silicon from all the window will be etched, which will make the chip fragile and hence it increases the chance of etching failure. Therefore, before placing the chip in the RIE chamber, all the area of the developed chip is painted using a paint brush with TI 35 resist except the window that is needed to be etched. The chip is then baked at 135 °C. Any bubble formation is avoided during photoresist painting otherwise the removal of the photoresist becomes very difficult after dry etch of the hard mask.

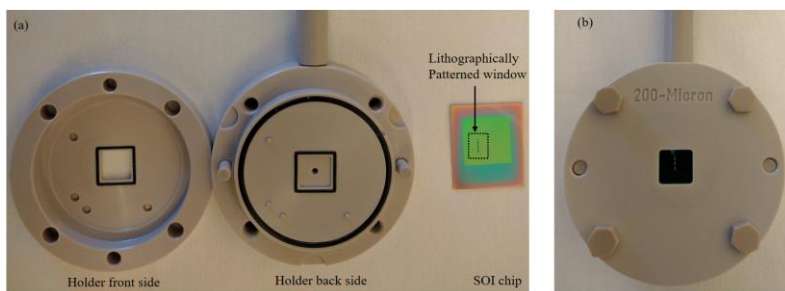


**Figure 3.8:** Camera image of the holder (a) in which the chip is mounted for silicon substrate etch and (b) with a mounted chip inside.

After removal of the resist mask from the lithographically patterned window, the SOI chip is placed in a holder (see **Figure 3.8**) that protects the top side and exposes the backside window to the etching solution. This holder is made of Polyether ether ketone (PEEK), which is resistant to KOH solution and protects the device layer during the course of substrate etch process. The black dotted rectangle at the center of the holder highlights the backside of the chip (lithographically patterned). The etch rate of silicon in the 20% KOH solution at 80°C is around 1.3  $\mu\text{m}/\text{min}$ .

The selectivity of silicon etch in the KOH solution between  $\langle 100 \rangle$  and  $\langle 111 \rangle$  crystalline plane is of the order of 200:1. This produces a characteristic anisotropic V-etch with sidewalls, which leads to a very narrow opening on the top layer as shown in **Figure 3.7(i)**. The size of the patterned window on the hard mask

depends on the substrate thickness. As in the present case, for the substrate thickness of  $200\ \mu\text{m}$ , a window size of around  $50\ \mu\text{m} \times 3.5\ \text{mm}$  was required on the device layer, a rectangular window of  $305\ \mu\text{m} \times 3.75\ \text{mm}$  was patterned on the backside by using contact photolithography.

The holder was removed from the KOH solution after the etching of the silicon stops at the BOX layer. The chip was then removed from the holder and rinsed in deionized water thoroughly. **Figure 3.9(a)** and **Figure 3.9(b)** shows optical microscope images of an array of PhC cavities without local silicon substrate from the backside and top side respectively.

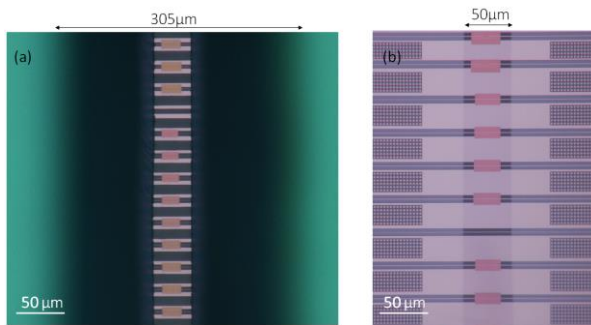


**Figure 3.9:** Optical microscope image of local silicon substrate etched PhC array seen from (a) backside and (b) topside.

**Figure 3.10** shows the scanning electron microscope (SEM) image of the cross section of the fabricated PhC cavity without local silicon substrate. The trapezoidal window below the BOX layer represents the area with no silicon substrate and is a characteristic signature of anisotropic silicon etch. The red dotted rectangular window highlights the BOX layer below PhC cavity. A platinum layer was deposited on the top layer for sectioning purpose through the PhC structures.

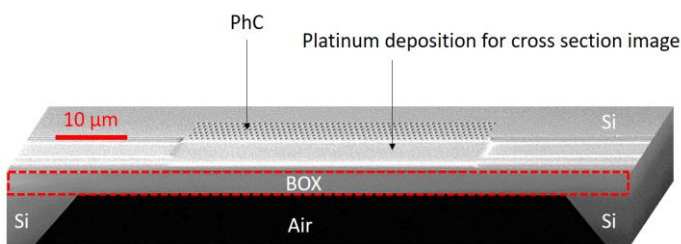


**Figure 3.10:** SEM image of the cross section of PhC cavity after removal of the silicon substrate.

### 3.2.4 Fabrication of Spot size converters

Efficient injection (coupling) of light from an optical fiber to a photonic integrated circuit (PIC) can be done by integrating coupling structures directly on the chip. These possible coupling structures can be classified into two main groups depending on the physical direction in which the fiber is coupled to PICs: in-plane and out-of-plane coupling. Typical in-plane coupling schemes is based on horizontal spot size converters, where the fiber is positioned in the chip plane. For out-of plane coupling, grating couplers is widely employed which couples light from a different direction (mainly vertical) than that of the waveguide. Since these grating couplers have a limited bandwidth, we have considered horizontal spot size converters. More specifically, we developed polymer waveguide coupler which are compatible with an end-fire coupling scheme. The goal of using SU8 polymer waveguide is to efficiently couple light from an optical lensed fiber into a strongly confined high index contrast 450 nm wide silicon waveguide. The spot-size conversion is achieved by using a silicon adiabatic taper with the taper tip width of 150 nm covered by a low-index SU8 waveguide of width 3  $\mu\text{m}$ . Once the mode is coupled from the SU8 polymer waveguide to underlying the higher-index waveguide, it can be coupled efficiently into the wire waveguide and hence into the PhC cavity. The integration of the spot size converter in our case decreases the coupling loss in a wire waveguide by factor of 15 with taper tip width of 150 nm. The coupling efficiency of such spot size converter improves with the reduction in the taper tip width. However, a minimal feature size of the tip width (150 nm) is imposed by standard deep UV lithography due to technological challenges.

Generally, the SU8 polymer waveguide can be patterned on an adiabatic silicon inverted taper by using contact photolithography on the top layer. Since removal of the silicon substrate locally makes the device layer very fragile, patterning of the SU8 waveguide before thinning the substrate would be an obvious choice. But after various processing steps (lapping, polishing, substrate etch), the chip will contain organic residues, particles. Therefore, it is very important to rinse the chip using Pirahna (3  $\text{H}_2\text{SO}_4$  : 1  $\text{H}_2\text{O}_2$  at room temperature) and SC-1 (5 DI water:1  $\text{H}_2\text{O}_2$  :  $\text{NH}_4\text{OH}$  at 80°C) solution between each step. It should also be noted that SU-8 polymer waveguide gets damaged and peeled off from the top layer during rinsing of chip in Pirahna and SC-1 solution as shown in the **Figure 3.11(a)**. That is why we opted to pattern SU-8 waveguide after the substrate removal process. After substrate etch, chip was rinsed in SC-1 for 15 minutes.

To ensure the maximum process reliability, the substrates must be cleaned and dried prior to applying the SU8 resist. Therefore, the substrate was rinsed using

piranha clean, followed by a DI water rinse. In order to dehydrate the surface, the substrate was baked at 200°C for 5 minutes on a hotplate. This treatment to the surface improves adhesion of the SU8 resist.

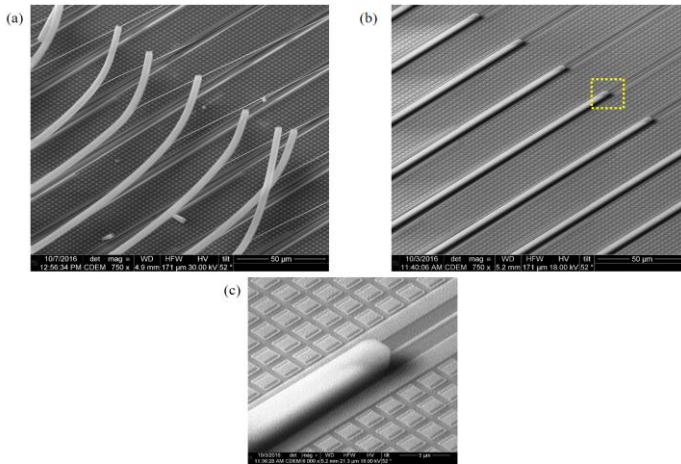


**Figure 3.11:** SEM image of (a) Peeling of patterned SU8 waveguide observed after mechanical lapping. (b) Patterned SU8 waveguide after silicon substrate removal. (c) Zoomed in interface of SU8 waveguide and silicon wire waveguide.

SU8-2 photoresist from Microchem was spin coated on the top of the device layer, which results in a film thickness of 3  $\mu\text{m}$ . The SU8 spin coated layer has to be completely baked otherwise the chip will stick to the contact mask during lithography process. Therefore, right after SU8 coating, we pre-baked the substrate at 65  $^{\circ}\text{C}$  on a hot plate for 1 minute. Then, the hot plate was ramped to 95  $^{\circ}\text{C}$  for soft-baking. The resist was soft baked for 3 minutes. After the completion of the soft bake, the hot plate was turned off and the substrates was left on the hot plate to cool slowly to the room temperature. Any air bubbles can be removed during the bake at 95  $^{\circ}\text{C}$  by gently tapping the air bubbles with a 24-gauge needle. Using Cross and Vernier markers located on the top layer of the chip, a 3  $\mu\text{m}$  wide and 500  $\mu\text{m}$  long rectangle was aligned on the top of the inverted silicon waveguide with high accuracy using alignment markers before exposure in photolithographic step. After exposure, the substrate was placed on a hot plate and post exposure bake (PEB) was done at 65  $^{\circ}\text{C}$  for one minute. Then, the hot plate was ramped to 95  $^{\circ}\text{C}$  for a second PEB and the substrate was baked for 3 minutes. After PEB, the hot plate was turned off and the substrate was allowed to cool down slowly to the room temperature. It must be noted that the rapid cooling of the substrate may cause thermal stress to built in the SU-8 film, and results in film crack. Therefore, slow cooling of the exposed substrate is necessary. **Figure 3.11(b)** shows the SEM image of the access waveguide array with patterned SU8

waveguide after complete removal of the substrate. In **Figure 3.11(c)**, a zoomed in image of the yellow dotted rectangular area marked in **Figure 3.11(b)** highlights the clear interface between the silicon wire waveguide and the SU8 waveguide. The exposed structures were developed by immersing the chip in a SU8 developer for 30 seconds. In order to stop the further development, the chip was rinsed in IPA for another 30 seconds. To make the SU8 waveguide hard for good cleave, the substrate was ramp hard baked between 150-200°C on a hot plate further cross link the material. The height of the fabricated structures was measured using a Veeco Dektak 6M profilometer. The characterization of such structures will be presented in the next section.

### 3.2.5 Isotropic etch of silicon dioxide layer

Once the silicon substrate is etched and the SU8 waveguide is patterned, we can proceed to the fourth and final step of **Figure 3.7** (i.e. last image of process flow **Figure 3.7(j)**), which is the etching of the BOX layer. Removing the BOX layer creates vertically symmetric structures, moreover it results in an increase of the vertical index contrast. The latter increases the optical field confinement and reduces propagation loss due to radiative leakage into the substrate.

The device layer was spin coated with TI35 photoresist. A window was then patterned on the top of photonic crystal structure using contact photolithography. The size of this patterned window is the same as that of the photonic crystal area. The BOX layer below the photonic crystal structures was then removed selectively by putting a droplet of buffered hydrofluoric acid (BHF) on the top of device layer. The etch rate of BOX layer in BHF is about 70 nm/min. The substrate-less free standing chip was rinsed in DI water and the photoresist from the device layer was removed in acetone. Stiction is a problem that may arise when processing certain photonic structures using liquids [11]. Substrate-less free-standing structures are not rigid enough and wet etching can alter the topography: during the drying phase of the liquid, capillary forces can pull the small silicon wires towards each other. Depending on several material parameters (e.g. spring constant), the photonic waveguides can remain stuck to each other after the liquid has dried.

To circumvent the above-mentioned problem of stiction (**Figure 3.12(a)**), we considered the use of critical point drying (CPD): conventionally, when a liquid dries, it converts from liquid to gas at a finite rate. However, for certain combinations of temperature and pressure, a distinction between liquid and gas can no longer be made and the system is said to be in the supercritical phase. By going from the liquid to the supercritical to the gas phase, we avoid the direct transition from liquid to gas and can avoid stiction, caused by capillary forces.

**Figure 3.12(b)** shows the optical microscope image of stiction free array of structures.

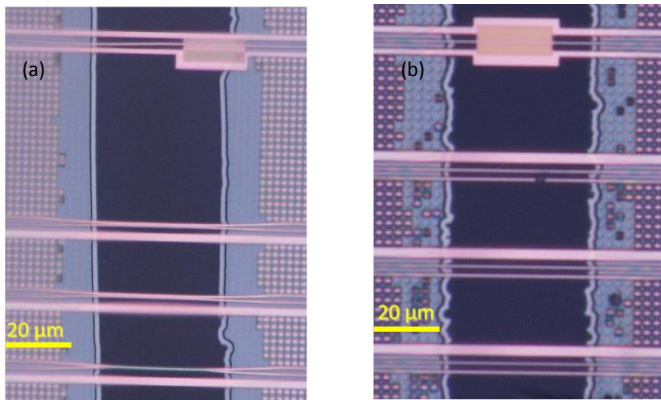


**Figure 3.12:** Optical microscope image of the substrate-less chip dried (a) without CPD (b) with CPD.

**Figure 3.13** shows various SEM images of a substrate-less PhC cavity array where the local oxide below PhC was individually removed for each of the devices. It can be seen that most of the structures cracked due to stress developed between the presence of the BOX layer in-between the waveguides. Therefore, we opted to etch the complete BOX layer from the backside (through the area whose silicon substrate is removed). Etching of BOX layer from back remove all the in-between BOX layer between the nearby waveguides. This will be otherwise present when it was etched from top and can cause stress.

Note that tiling as highlighted in **Figure 3.13**, a technique used in CMOS industry to improve etch uniformity, should be avoided in the neighborhood of the underetched structures: tiles are released due to removal of the silicon dioxide and can redeposit on the photonic structure after drying, causing additional scattering losses. Therefore, a no tiling layer must be used near the PhC structures during the mask design phase.

**Figure 3.14** shows the optical microscope image of a substrate-less free-standing PhC cavity array fabricated with the optimized process. To observe with high-resolution image of substrate-less free-standing PhC cavity SEM images were taken, see **Figure 3.15**. As can be seen in the figure, the PhC membranes are deflected out-of-plane. This bowing was characterized by a white light interferometer. As can be seen from **Figure 3.16**, the silicon membrane is deflected upwards by 320 nm. It results from the stress which is caused by the thermal expansion coefficient mismatch between different materials and is

therefore difficult to avoid. This is an issue since large compressive or tensile stresses can lead to buckling or breaking of the membrane. In the present case, the problem of buckling is due to compressive stress and is not further investigated here but can be the subject of future work.

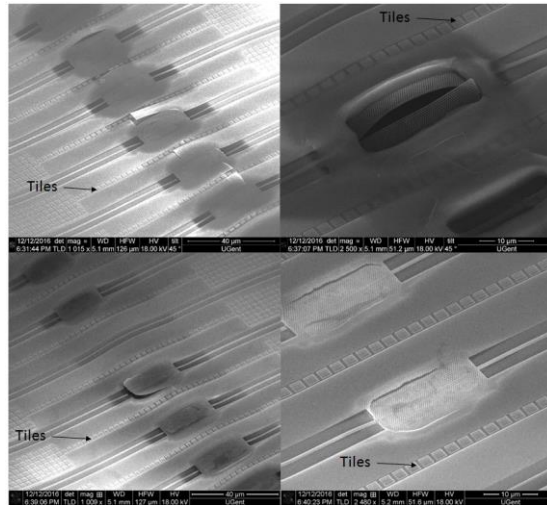


**Figure 3.13:** SEM image of the substrate-less PhC array where some PhC membrane collapsed due to stress developed between top silicon and BOX layer.

E. Iwase *et al.* described a general method to avoid stress-induced buckling of thin and large freestanding membranes [12]. They showed that using properly designed supports, in the form of microbeams, the out-of-plane deflection of the membrane can be reduced while maintaining its stiffness. But it should be noted that design of support structure will vary depending on the individual structure.

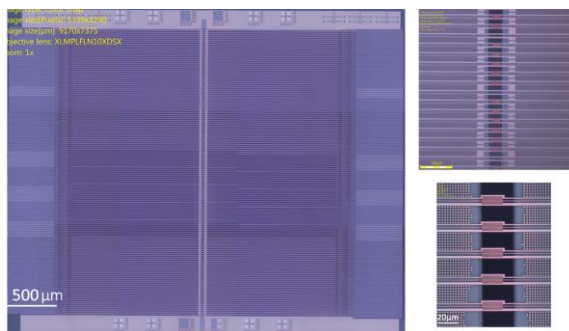


**Figure 3.14:** Optical microscope image of the free-standing substrate-less PhC array.

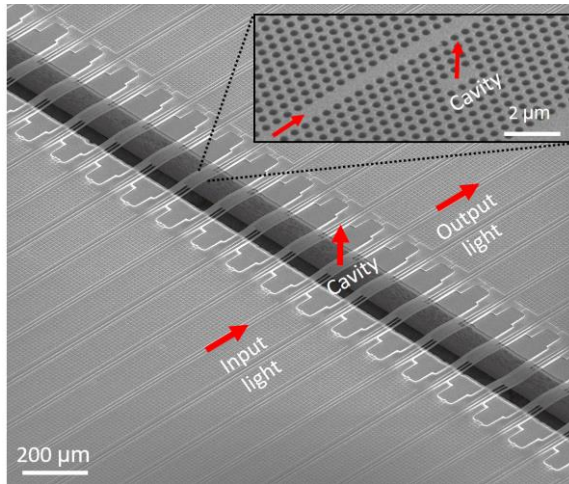


**Figure 3.15:** SEM image of a free-standing substrate-less photonics crystal cavity array (Inset shows the zoomed in image of the cavity).

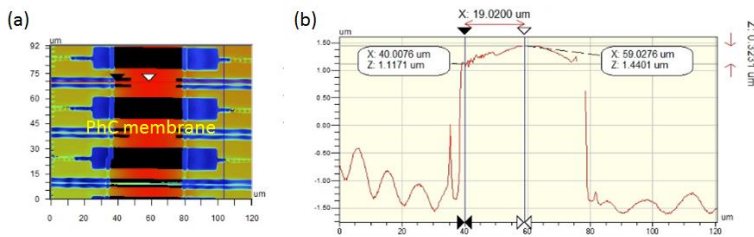


**Figure 3.16:** (a) White light interferometer image of substrate-less free-standing PhC cavities (b) Upward deflection of 320 nm was measured.

In addition, although a significant number of processing steps is required to achieve such free-standing substrate-less cavities, the quality (Q) factors of the cavities that is of the order of a few thousand remains unaffected. **Figure 3.17(a)** shows the experimental setup that was used to characterize the PhC cavities. **Figure 3.17(b)** and **3.17(c)** shows the transmission spectra of two PhC cavity membranes where cavity 1 is free-standing with substrate and cavity 2 is also free-standing but without substrate. The black curve in the figure is the measured intensity collected from the top cavity surface and red curve is the Lorentzian fit of the transmission spectrum.

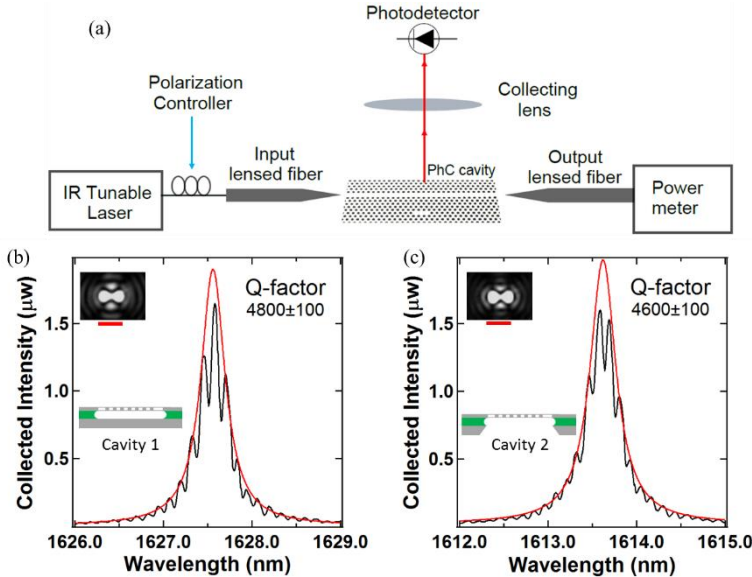


**Figure 3.17:** (a) Experimental setup for the characterize the PhC cavities. Transmission spectra of suspended PhC cavity (a) with substrate and (b) without substrate, respectively. (Inset) Intensity pattern of the cavity field at resonance; the red scale of the image corresponds to 1.5  $\mu\text{m}$

### 3.3 Fabrication of nano-fiber tip

The process that I have developed enables access to the cavity from both sides. In particular, a high NA collection of the scattered cavity field and the controlled approach of a nano-object are made possible simultaneously. As a result, the refractive index sensing properties and the light confinement properties can be investigated if we are able to control the position and the size of a nano-object in the near field of the cavity. We have chosen to use a nano-fiber tip as a nano-object. Many publications discuss methods for fabricating nano-fiber tips for Near-field scanning optical microscopy (NSOM) application. The two most common techniques are adiabatic pulling and chemical etching. The pulling technique has been quite well characterized [13,14] and generally results in tips with small cone angles, but yield low throughput. There are two different general chemical etching methods, the meniscus etching and selective etching. The latter has been pioneered primarily by Ohtsu and involves the use of variable concentrations of HF,  $\text{NH}_4\text{F}$  and BHF to etch single-mode and multimode fibers into selected tip geometries [15]. Here, we have used the meniscus etching method for fabricating the nano-fiber tips (see **Figure 3.18**). Meniscus etching employs an organic protective solvent that forms a layer above the HF acid solution. The etching of  $\text{SiO}_2$  fibers by HF is an isotropic etching process [16] so the fiber is a

cylinder of decreasing radius below the meniscus. At the meniscus, the decreasing radius causes the meniscus height to drop steadily, resulting in a conical tip shape.

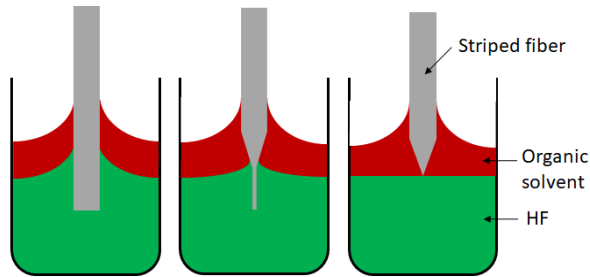


**Figure 3.18:** Schematics of the meniscus etching process. The fiber at time zero (left), at time  $\tau/2$  (middle) and at time  $\tau$  (right). The meniscus formed at the liquid–liquid and liquid–solid interfaces lowers height, as the fiber radius decreases. When the fiber radius converges to zero at time  $\tau$ , the final taper portion is created.

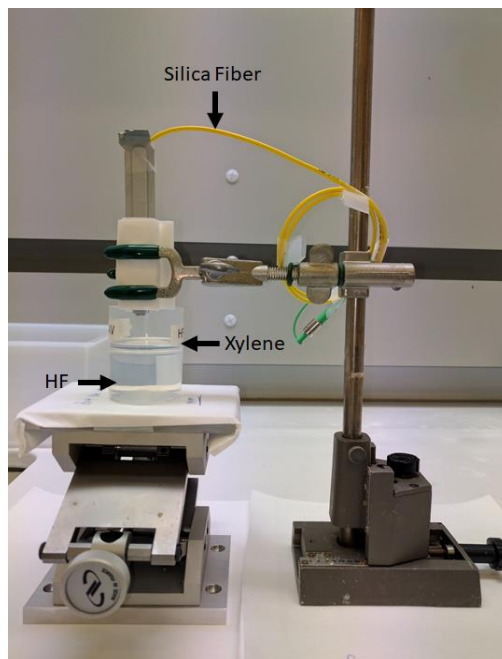


**Figure 3.19:** Setup for nano-fiber tip fabrication.

**Figure 3.19** shows the experimental meniscus etching set-up for nano-fiber fabrication. The fiber was positioned in the center of the beaker that contained the two-phase etching solution. The translation stage controlled the fiber's vertical position. Fiber (Thorlabs single mode, 8  $\mu\text{m}$  core, 125  $\mu\text{m}$  cladding) were etched

with 50% aqueous HF with an organic protective layer of xylene for 35 minutes. Prior to etching, the fiber end to be etched was soaked in acetone for 7 minutes to remove the acrylate jacket. After 35 minutes, the fiber is pulled out slowly from the beaker and dipped in another beaker filled with DI water. Scanning electron microscopy (SEM) was used to characterize tip shapes, lengths and angles. With each of the etching techniques used here, tip diameters of  $\sim 20\text{--}100$  nm were achieved. **Figure 3.20(a)** shows the SEM image of the fabricated nano-tip from this process.

For our application, we also need to fabricate nano-fiber tips with cylindrical apex instead of conical one. Another demonstrated technique for probe fabrication is the dynamic etching method, in which the fiber is translated vertically while being etched [17]. By moving the fiber at variable speeds for different times, a variety of tip shapes can be created. In order to fabricate cylindrical apex tips, at first the fiber is etched for 33 minutes without moving the fiber tip. This etches the fiber down to  $1\ \mu\text{m}$ . Next, the etched fiber is dipped in BHF solution and moved vertically in the etching solution. This resulted in fabrication of nano-fiber with cylindrical apex as shown in **Figure 3.20(b)**.

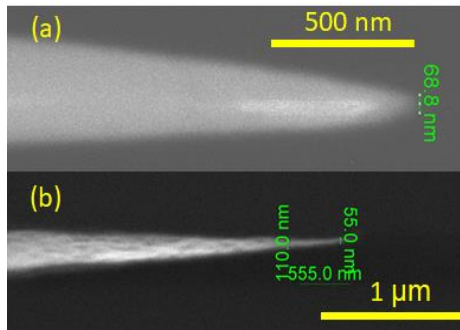


**Figure 3.20:** SEM image of fabricated nano-fiber tip (a) without and (b) with vertical fiber movement.

### 3.4 Conclusion

In this chapter, we have described all the technological processes that have been developed to study the sensing properties of the PhC cavities. We have implemented a process for anisotropic etching of the silicon substrate of SOI chips in our clean room facilities. It should be noted that E. Hallynck [18] also developed a process for anisotropic silicon etching but it involved deposition of protective layer of hard mask on the top side, which is difficult to remove accurately after the silicon etching. This process is not practical if the top layer has active devices as the deposition of hard mask on such layer will jeopardize

the device performance. Also, if the hard mask of the top layer is not completely removed then fabrication of horizontal size converter will be difficult. One of the major benefits of the process developed in this chapter is that, although the processing in this work is carried out on individual chips, it is possible to execute the entire flow on wafer-scale. As can be gathered from this chapter, there are many pitfalls and factors to consider in this process. Problems of stiction and mask adhesion have been described here and we have proposed a solution. The process itself can also be fine-tuned further, e.g. by using better quality PECVD silicon nitride or by simply using low pressure chemical vapor deposition (LPCVD) silicon nitride. I have also described the fabrication process of the nano-fiber tip for probing of PhC cavities from backside.

## Reference

- [1] K. Saurav, S. Kumari, N. Le Thomas, "CMOS Fabricated Large Array of Free Standing Substrate-Less Photonic Crystal Cavities for Biosensing Applications", *IEEE Photonics Journal*, 9(2), (2017).
- [2] G. Roelkens, A. Abassi, P. Cardile, U. Dave, A. de Groote, Y. de Koninck, S. Dhoore, X. Fu, A. Gassenq, N. Hattasan, Q. Huang, S. Kumari, S. Keyvaninia, B. Kuyken, L. Li, P. Mechet, M. Muneeb, D. Sanchez, H. Shao, T. Spuesens, A. Z. Subramanian, S. Uvin, M. Tassaert, K. van Gasse, J. Verbist, R. Wang, Z. Wang, J. Zhang, J. van Campenhout, X. Yin, J. Bauwelinck, G. Morthier, R. Baets and D. van Thourhout, "III-V-on-Silicon Photonic Devices for Optical Communication and Sensing," *Photonics*, 2(3), pp.969-1004 (2015)
- [3] S. Kumar Selvaraja, P. Jaenen, W. Bogaerts, D. Van Thourhout, P. Dumon, R. Baets, "Fabrication of Photonic Wire and Crystal Circuits in Silicon-on-Insulator Using 193nm Optical Lithography," *Journal of Lightwave Technology* 27(18), pp. 4076 - 4083 (2009).
- [4] W. Bogaerts, P. Dumon, V. Wiaux, J. Wouters, S. Beckx, R. Baets, Tolerance control for photonic crystal structures fabricated with deep UV lithography, *ECOC 2003*, 5, Italy, p.46-47 (2003).
- [5] Y. Tzeng and T. H. Lin, "Dry etching of silicon materials in SF<sub>6</sub> based plasmas," *Journal of Electrochemical Society*, 134(9), pp. 2304–2309 (1987).
- [6] M. J. Madou, *Manufacturing Techniques for Microfabrication and Nanotechnology* By, CRC press (2011).
- [7] O. Tabata, R. Asahi, H. Funabashi, K. Shimaoka, S. Sugiyama, "Anisotropic etching of silicon in TMAH solutions," *Sensors and Actuators A: Physical* 34(1), pp. 51-57 (1992).
- [8] <http://www.hazard.com/msds/mf/baker/baker/files/t1816.htm>
- [9] <https://cleanroom.byu.edu/KOH>
- [10] K. K. Schuegraf, "Handbook of Thin-Film Deposition Processes and Techniques: Principles, Methods, Equipment, and Applications," Park Ridge, NJ, USA: Noyes (1988).

- 
- [11] J. Roels, "Actuation of integrated nanophotonic devices through the optical gradient force," PhD thesis, Ghent University (2011).
- [12] E. Iwase, P.-C. Hui, D. Woolf, A. W. Rodriguez, S. G. Johnson, F. Capasso, and M. Loncar. Control of buckling in large micromembranes using engineered support structures. *Journal of Micromechanics and Microengineering*, 22(065028), 2012.
- [13] G. A. Valaskovic, M. Holton, and G. H. Morrison, "Parameter control, characterization, and optimization in the fabrication of optical fiber near-field probes," *Appl. Opt.* 34(7), pp. 1215-1228 (1995).
- [14] X. Liu, J. Wang, and D. Li, "Simple device and reproducible approach for producing high efficiency optical fiber tips for a scanning near-field optical microscope," *Review of Scientific Instruments* 69, p. 3439 (1998).
- [15] Ohtsu, M. (1998) *Near-Field Nano/Atom Optics and Technology*. SpringerVerlag, Tokyo
- [16] M.A. Unger, D.A. Kossakovski, R. Kongovi, J.L. Beauchamp, J.D. Baldeschwieler, and D.V. Palanker, "Etched chalcogenide fibres for near-field infrared scanning microscopy," *Rev. Sci. Instrum.* 69, pp. 2988–2993 (1998).
- [17] H. Muramatsu, K. Homma, N. Chiba, N. Yamamoto, and A. Egawa, "Dynamic etching method for fabricating a variety of tip shapes in the optical fibre probe of a scanning near-field microscope," *J. Microsc.* 194, pp. 383–387 (1999).
- [18] E. Hallynck, "Applications of Integrated Photonic Structures on Membranes Fabricated by Locally Etching the Silicon Substrate," PhD thesis, Ghent University (2013).



# 4

## **Development of an advanced optical set-up for characterizing PhC cavities**

To study the optical property of the different PhC cavities that were designed, we have developed an advanced experimental set-up. This set-up allows: 1) collecting the field radiated by the cavity, 2) detecting the transmission of the access waveguide, 3) exciting the PhC cavity, 4) probing of the near field of the cavity, 5) locating a nano-object in the near field of the cavity in a controlled way.

This chapter is organized as follows: In the first section, a general description of the experimental apparatus is provided. The second section focuses on the imaging part of the set-up which is used in the characterization of PhC cavity structures. In the third section, the placement and the imaging of the nano-fiber tip is presented. The evaluation of a 3D nanoparticle interaction using a nano-tip will be presented in the fourth section. In the last section, we discuss the development of a new technique to map the interaction between a nano-object and a photonic crystal cavity mode.

## 4.1 Overview and general considerations

**Figure 4.1** shows a schematic of the experimental setup in its current configuration. The main building blocks are highlighted using the following color code: brown for end-fire path (for measurement of transmission and reflection spectra eventually), blue for the visible imaging path (for the alignment purpose), red for infrared (IR) imaging path (for near field and far-field imaging of scattered light from the cavity surface). The optical assembly is such that the sample lies in the object focal plane of the high NA (0.95) microscope objective which forms an image at infinity. In order to create an image with such infinity corrected objective, a tube lens (L3) of 300 mm focal distance is introduced to focus the image. As parallel light beam passes between the objective lens and tube lens, parfocality between different objectives can still be maintained even when one or more auxiliary components (such as beam splitters, prisms or polarizers etc.) are added into the optical path without the introduction of spherical aberration. In such system, the magnification does not change even if the distance between the objective lens and tube lens is changed.

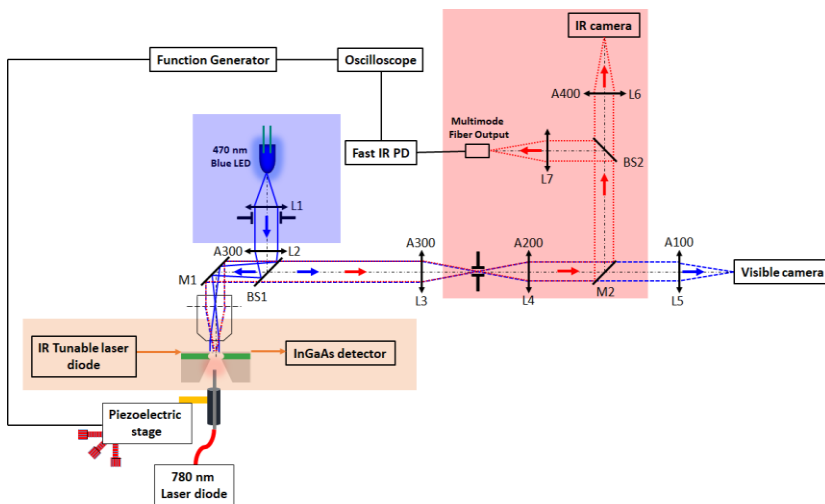


**Figure 4.1:** Schematic of the experimental apparatus illustrating the main functions. The PhC cavities are excited using a tunable laser diode, on the bottom left. The light scattered out of the plane by the photonic structure is collected in the IR imaging arm (red area). Blue LED illuminate the sample that is imaged on the CCD camera.

### 4.1.1 End-fire path

As shown in the bottom left part of **Figure 4.1**, we have used a standard end-fire setup to excite the photonic structures under study and obtain their transmission spectra. The excitation laser source is a highly monochromatic external cavity laser Nettest Tunics Plus, tunable within the wavelength range of 1500 nm to 1640 nm. The resolution of the wavelength tuning is  $\Delta\lambda = 0.1$  pm. For a few experiments, we have used Santec 1550 nm laser as it has a much narrower linewidth compared to Tunics and consequently better noise performances. The laser output is linearly polarized in the vertical direction; however, we can control the polarization direction in the excitation path using polarized controller to excite separately the TE or TM modes. The optical signal is then injected into the structure via a lensed fiber and an adiabatically tapered spot size converter. The signal transmitted through the photonic structure is coupled out by means of another lensed fiber and detected using a InGaAs power meter. The accurate positioning of the input and output fiber (spot diameter  $2\ \mu\text{m} \pm 0.3$ , working distance  $6\ \mu\text{m} \pm 1$ ) in front of the coupling ridge waveguides ( $3\ \mu\text{m}$  wide and  $3\ \mu\text{m}$  high) is a critical aspect of the experiment. It is ensured with the aid of three 6-axis nano-positioning Luminos stages (20 nm step) and homemade fiber-supporting mechanical element.

### 4.1.2 Visible imaging path

The visualization of the sample surface is crucial for the alignment of the end-fire path, i.e., for the adjustment of the position between the lensed fibers and the integrated spot size converter to allow for light in/out-coupling. Nevertheless, it also allows for a quick visual observation of the chip surface that can disclose any possible imperfections in the device quality. Some obvious damage can be such as broken structures, dusts and large sample defects.

The visible imaging block comprises two parts: the visible illumination arm and the imaging arm. The main goal is to provide good uniformity illumination over the field of the view of the microscope objective. The Köhler illumination is a typical architecture for this purpose. As shown in **Figure 4.1**, the light emitted from a blue light emitting diode (LED) is collected by a condenser lens system L1 ( $f = 50.8$  mm), L2 ( $f = 300$  mm) and collimated on the sample surface using either a low NA = 0.2 or high NA = 0.95 microscope objective. In this way, a homogeneous illumination of the chip surface is realized. The silicon photonic structures are opaque in the visible wavelength range, which makes it possible to obtain a high contrast image of the sample surface in epi-illumination (reflection) configuration. Light reflected from the chip surface is collected by the same

objective and projected by the achromatic lenses L3 ( $f = 300$  mm), L4 ( $f = 200$  mm) and L5 ( $f = 100$  mm) on a CCD Camera from Thorlabs as shown in **Figure 4.1**. The combination of 470-nm illumination, high numerical objective of  $NA = 0.95$  and the high magnification of the visible path make it possible to resolve features at the resolution limit of around 300 nm. **Figure 4.2** shows the image of a PhC cavity with and without substrate below captured by the visible camera.

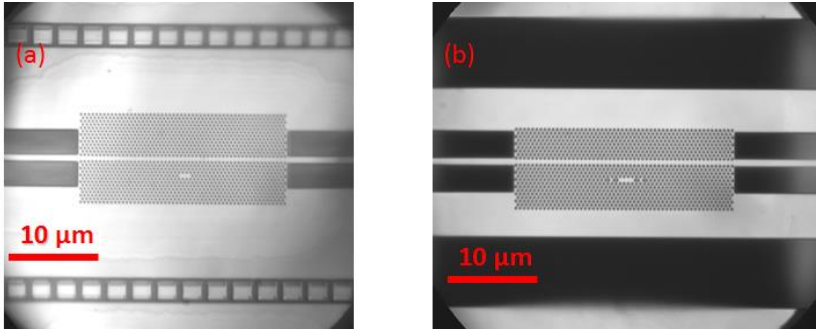


**Figure 4.2:** Visible camera image of PhC cavity (a) with substrate and (b) without substrate below.

### 4.1.3 Infrared imaging path

The infrared (IR) path constitutes the main part of the imaging setup and it allows for imaging of the light intensity distribution at the cavity surface. Light scattered from the cavity surface is collected by a high numerical aperture microscope objective ( $NA = 0.95$ ), which is placed at one focal distance from the top cavity surface. The front focal plane of the objective lens where the real space image is found, is projected onto a near infrared (NIR) camera by a series of achromat doublets L3, L4 and L6 as shown in **Figure 4.3**. The lenses are placed in the so-called f-f configuration, where the back focal plane of one lens coincides with the front focal plane of the following lens. All lenses are oriented with the convex facet towards the collimated beam to minimize the spherical aberration.

The lens L6 projects the image on the InGaAs Xeva camera (by XenICs), sensitive to a wavelength range between  $0.9 - 1.7 \mu\text{m}$ . The mirror M2 allows to switch between the visible image and IR image. The beam splitter (pellicle) BS2 splits the scattered light from the cavity with ratio of 50:50 where 50% of scattered light falls on the InGaAs Photodetector and the other 50% of the light falls on the IR camera. In order to efficiently collect the reflected light by BS2, a fiber-collimator ( $f=6.18$  mm,  $NA=0.28$ ) is placed in front of the photodetector.

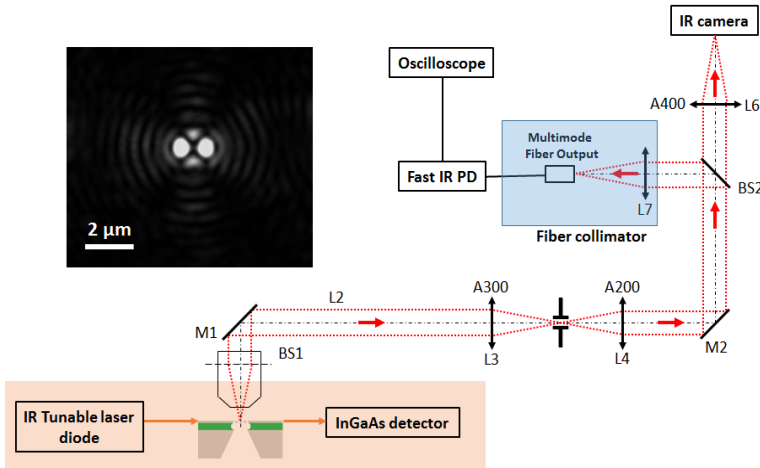


**Figure 4.3:** Infrared path used for real-space imaging (Inset - intensity pattern of a cavity field at resonance captured by the IR camera).

## 4.2 Spectral characterization of different types of PhC cavities

This section presents the transmission spectra of various PhC cavities fabricated using DUV lithography. From the transmission spectrum, The Q factor can be extracted which is an important parameter to infer the sensing properties of the cavity. Such cavities can be categorized in two groups: the first group focuses on the cavities whose maximum of EM field is localized in the high index (silicon in our case) medium and the second group focuses on the cavities whose maximum of EM field is localized in the low index (air in our case) medium.

### 4.2.1 L3 based PhC cavities

**Figure 4.4(a)** shows a Scanning-Electron Micrograph (SEM) of a fabricated L3 cavity (lattice constant,  $a = 440$  nm, radius,  $r = 112$  nm). The local BOX layer below the PhC cavity is etched away. An input light power of  $750 \mu\text{W}$  is injected in the PhC cavity structure. The separation between the W1 waveguide and the L3 cavity is 4 holes and when this separation is less than 4 lines of holes, the Q factor of the cavity is substantially decreased due to over coupling. When this separation is further increased, the Q factor remains the same but the light intensity collected from the cavity surface decreases.

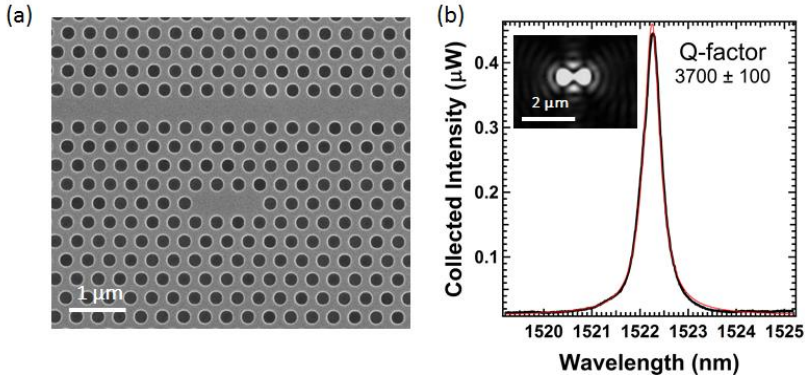


**Figure 4.4:** (a) Scanning Electron Micrograph image of a standard L3 cavity, (b) Transmission spectra of free standing L3 cavity, (Inset - intensity pattern of the cavity field at resonance).

The transmission spectrum collected from the PhC cavity surface is plotted in **Figure 4.4(b)**. The black curve in the **Figure 4.4(b)** is the measured intensity collected from the top cavity surface and the red curve is the Lorentzian fit of the transmission spectrum which are in very good agreement. The inset of the **Figure 4.4(b)** displays the intensity pattern of the cavity field at resonance; the white scale in the legend of the image corresponds to 2  $\mu\text{m}$ . The typical Q factor of a simulated standard L3 cavity when the separation between W1 and the cavity is  $2.5\sqrt{3}\times a$  is around 5000. This value is similar to what we have also measured.

In order to avoid any oscillation in the transmission spectra of the cavities due to Fabry-Perot fringes caused by reflections at the sample facets, this chip was cleaved only at one side. Moreover, the light into PhC structure was injected via a 450 nm wide wire waveguide instead of a horizontal spot size converter. The output waveguide width is tapered from 450 nm to 130 nm which allows the transmitted light to radiate in the silicon layer instead of getting back reflected.

As explained in chapter 2, the Q factor of a standard L3 can be increased by laterally shifting the holes and by varying the hole diameter. Noda et.al. [1] proposed one of such design, where 3 holes along  $\Gamma\text{K}$  direction on the both sides of cavity are laterally shifted away from the core by a length of  $(0.2a, 0.025a, 0.2a)$ , where 'a' is lattice constant of the cavity. **Figure 4.5(a)** shows a SEM image of such a fabricated modified L3 cavity (lattice constant,  $a = 460$  nm, radius,  $r = 112$  nm). The transmission spectrum of the cavity is plotted in **Figure 4.5(b)**. It should be noted that if the separation between modified L3 and W1 is further increased, then even higher Q factor can be achieved [16] but consequently the scattered power collected from the cavity surface will substantially decrease. As will be

discussed in chapter 5, for our application it is important that we collect significant amount of power from the cavity surface.

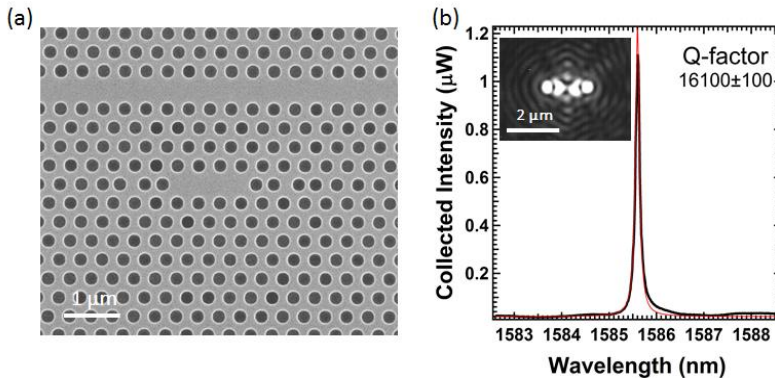


**Figure 4.5:** (a) Scanning Electron Micrograph image of a modified L3 cavity, (b) Transmission spectra of free standing modified L3 cavity, (Inset - intensity pattern of the cavity field at resonance).

## 4.2.2 Hollow core PhC cavities

A simple hollow core cavity can be realized by etching a narrow slot in the center of a standard L3 cavity. The width of such slot is around 80 nm. **Figure 4.6** shows the SEM image and the transmission spectrum of a fabricated L3 with slot cavity. The chip containing this structures was cleaved from both the sides, which explains the Fabry-Perot oscillation in transmission spectra of the cavities. Such oscillations are caused by reflections at the sample facets and at the interface between the PhC pattern and access waveguides. The simulated Q factor is around 5000.

Another kind of hollow core cavity can be realized by shifting the holes adjacent to the slot to form a width-modulated line-defect cavity reported by Yamamoto *et al.* [2]. The SEM images of the fabricated slot cavity is shown in **Figure 4.7**. The circle highlights the holes that were shifted to realize the slot cavity. The red, yellow and blue circle were shifted by 15 nm, 10 nm and 5 nm respectively. Exciting such a cavity is not straight forward as the input light first couples into the slot and through this slot the light gets coupled into the cavity. There is a need for a better design of air-slot cavities in which mode excitation can be done more efficiently without making use a slot waveguide in the PhC. Such kind of cavity is also prone to buckling due to the presence of the long slot along the PhC structure.

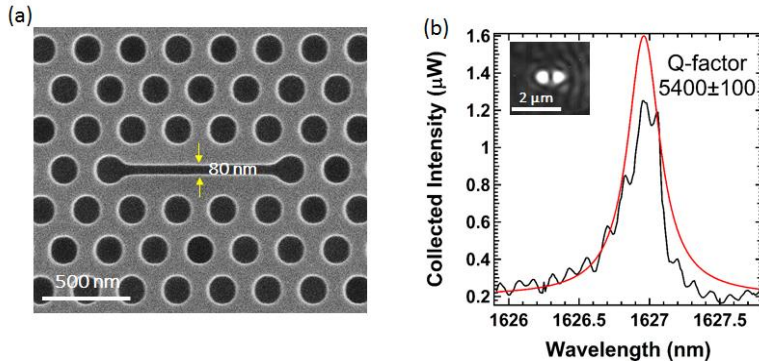


**Figure 4.6:** (a) Scanning Electron Micrograph image of a standard L3 with slot cavity (slot width = 80 nm), (b) Transmission spectra of free standing L3 with slot cavity.

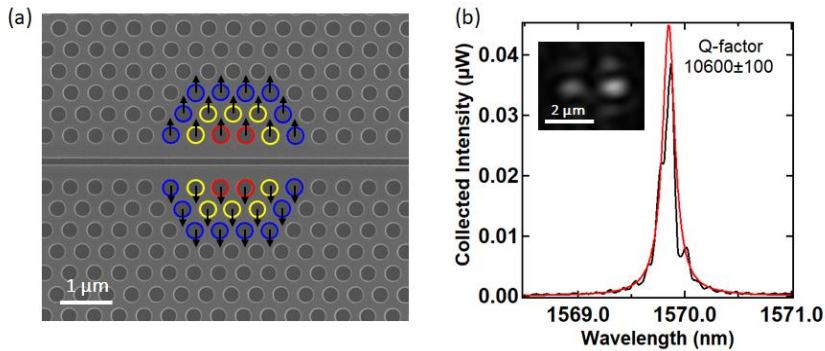


**Figure 4.7:** (a) Scanning Electron Micrograph image of a width modulated slot cavity, (b) Transmission spectra of free standing L3 with slot cavity (Inset: intensity pattern of the cavity field at resonance).

### 4.3 Technique to spatially characterize the interaction volume of PhC cavities

Probing of the mode volume of a PhC cavity can provide utmost relevant information for designing the light-matter interaction at the nanoscale. Spatially probing a cavity can be done by positioning a nano-fiber tip in the near field of the cavity and simultaneously measuring the scattered intensity from the cavity mode. The placement of the nano-tip of various apex sizes will allow us to determine the spectral sensitivity of the cavity. It should be noted that our approach is different from Scanning Near-field Optical Microscopy (SNOM) techniques. In conventional SNOM techniques, the light is collected through the near field tip. A modified version of SNOM consists in collecting the scattered

light induced by the presence of a tip in the far field [3]. Using an end-fire measurement technique, Hopman *et al.* have used an alternative approach by placing an AFM tip in the near field of the PhC cavity and mapping the response through the output waveguide [4]. In our case, the nano-object modifies the out of plane intensity of the field that is scattered by the cavity and the corresponding intensity variation are recorded.

When a dielectric nano-object approaches the near field of an optical cavity, the local refractive index changes. It results in a redshift of the wavelength of the cavity resonance and a concomitant variation of the intensity stored in the cavity for an excitation at a fixed wavelength. In this case, the bandwidth of the exciting laser field must be much smaller than the cavity linewidth.

For weak perturbations, the intensity variation is proportional to the local cavity field intensity and to the volume of the nanoparticle. It follows that spatially mapping the perturbation-induced intensity variation provides a map of the intensity distribution of the cavity field if the pump is tuned to a linear part of the cavity spectrum. The change in the transmission properties of the cavity due to the presence of a nano-object can be measured by collecting either the out-of-plane scattered signal directly from the cavity surface (scattering mode) or by measuring the variation of the exciting light transmitted at the output waveguide (transmission mode) or the reflection of the signal at input (reflection mode).

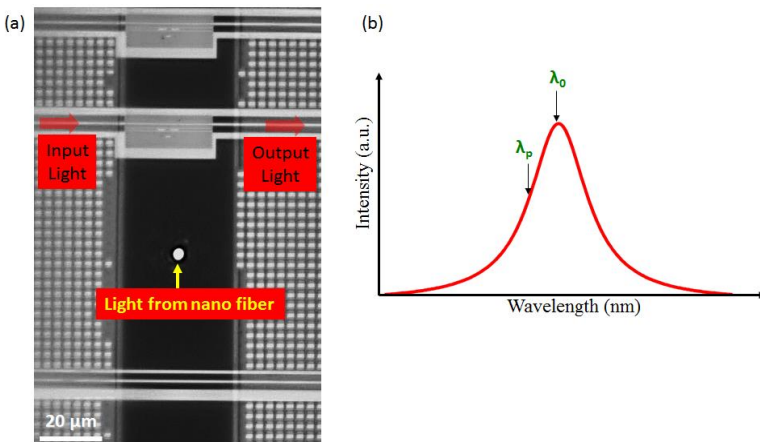


**Figure 4.8:** (a) Visible image of a PhC cavity array along with a nano-tip (by high NA microscope objective) fiber in the neighborhood. The highlighted PhC structure has fiber coupled at the input and the output, (b) Cavity excitation scheme,  $\lambda_0$  is the resonance and pump wavelength respectively.

We first discuss the information generated by a nano-tip whose apex diameter is 70 nm. This is achieved by introducing a silica nano-fiber tip mounted on a piezoelectric stage below the cavity surface and by probing the photonic crystal cavity region. In order to locate the position of the tip the other end of the fiber is initially connected to a 780 nm laser diode. The emission of this laser diode is scattered at the apex of the fiber, which allows locating the position of the tip. For this investigation, we have used a free-standing substrate-less L3 cavity, which allows us to bring the nano-tip close to cavity surface from the backside as shown in **Figure 4.8(a)**.

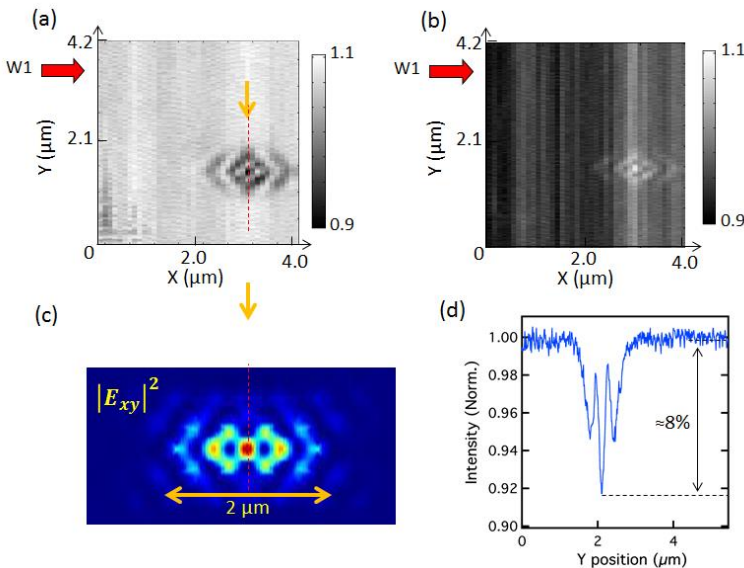


**Figure 4.9:** Measured map of the intensity variation induced by the interaction between the nano-tip fiber and the L3 cavity in (a) Scattering mode, (b) transmission mode, (c) Simulated mode profile of a L3 cavity at the cavity surface (red and blue represents high and low intensity respectively), (d) variation of intensity at center of the cavity in y direction along red dotted line in scattering mode (extracted from (a)).

At first, the cavity is excited using the setup schematically shown in **Figure 4.1**. The wavelength at resonance ( $\lambda_0$ ) of the cavity is measured and the pump wavelength ( $\lambda_p$ ) is then blue shifted compared to  $\lambda_0$  such that it lies in the wavelength range where the cavity spectrum can be considered linear. While accurately maintaining the alignments, a silica fiber consisting of a nano-tip at one side is approached near the backside of cavity surface. As shown in the **Figure 4.8(a)**, the tip is brought closer to the cavity surface by tracking the light scattered from the nano-fiber tip. **Figure 4.8(a)** shows the visible camera image of an array of substrate-less PhC cavity structures and the nano-fiber tip that is positioned in

between the two photonic structures. Next, the nano-fiber is brought below the cavity surface carefully by using a piezoelectric stage and by avoiding any contact with the photonic chip. After a careful positioning of the tip below the cavity, the 780 nm laser diode emission is switched off.

The tip is scanned near the cavity laterally (XY plane) for different positions in Z axis below the cavity surface. The interaction of the tip with the cavity at different positions on Z axis induces a variation of the out-of-plane scattering intensity (and from the output waveguide). Two 1.2 GHz InGaAs photodiode from Thorlabs (DET01CFC) detects the scattered and transmitted intensity and the corresponding photo voltage is recorded with a 1 GHz oscilloscope from Agilent Technologies (DS06104A).

The Y piezoelectric stage was connected to a function generator which applies a triangular ramp of maximum amplitude of 0.3 Volt. This allows the collection of the signal from the cavity surface with a resolution of 10 nm in Y direction (see **Figure 4.9(a)**). After one scan acquisition along Y (which corresponds to a total displacement of 4  $\mu\text{m}$ ), the X piezo moves the tip by 100 nm (smaller step is also possible). In this way the nano-tip moves near the cavity surface and the corresponding intensity variation is recorded.

When the tip comes very close ( $\sim 100$  nm) to the cavity surface, it starts to touch the part of the PhC membrane around the cavity area. This is because the membrane is not flat and is bend upwards due to the buckling effect as explained in Chapter 3. This does not allow the intensity variation recording at a very close proximity of the cavity surface, i.e. closer than 10 nm in general by restricting the scanning area. When the tip starts to touch the membrane, a change in scattering pattern was observed compared to scattering from other part of the membrane as shown in **Figure 4.9(a)** below  $x = 0.1 \mu\text{m}$ . **Figure 4.9(a)** and **4.9(b)** shows the map of the interaction between the nano-fiber tip and the cavity field in scattering and transmission mode respectively. This map of the cavity field was recorded at around 100 nm far from the cavity surface. Such an estimate relies on the determination of the bending angle with a white light interferometric technique. It can be seen in **Figure 4.9(a)** and **4.9(b)** that the intensity distribution maps are complementary to each other. A decrease in the scattered intensity is accompanied by an increase in the transmission intensity. **Figure 4.9(c)** shows the FDTD simulated intensity of the in-plane component of the cavity field,  $|E_{xy}|^2$ , the envelope of which is very similar to the one that is showed in **Figure 4.9(a)**. **Figure 4.9(d)** shows the intensity variation at the center of the cavity in Y direction along the red dotted line present in **Figure 4.9(a)**. We observe an intensity drop of 8 % (with a signal to noise ratio of  $S/N = 21$ ). Based on the current noise, the smallest shift in resonance wavelength is expected to be 20 pm,

which corresponds to a figure of merit,  $F = \delta\lambda_{\min}/\Delta\lambda_{\text{FWHM}} = 1/180$ , where  $\delta\lambda_{\min}$  is the minimum detectable wavelength shift and  $\Delta\lambda_{\text{FWHM}}$  is cavity linewidth (the full width at half maxima). In view of the intensity noise measurement performed in chapter 5, we attribute the current noise contribution to the vibration of the nano-tip.

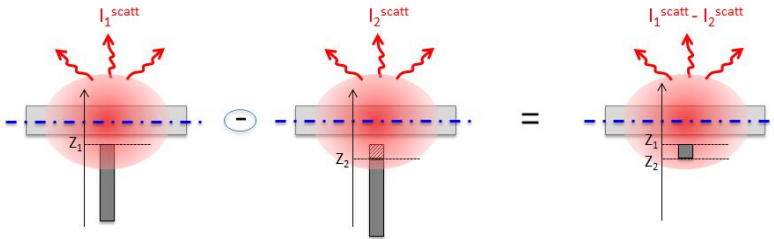


**Figure 4.10:** Superposition principle: Scattered intensity collected from the cavity surface due to the presence of the nano-tip at different axial positions normal to cavity surface is subtracted to calculate the impact of the resulting nano-object on collected intensity.

#### 4.4 Experimental determination of the sizing capabilities of the PhC cavity

The ability of planar 2D PhCs to confine the electric field to small volume (few  $\mu\text{m}^3$ ) has garnered considerable interest for sensing particles, such as viruses. For sensing, two crucial issues must be addressed. First the sensing element has to be able to distinguish nano-objects of different size or shape when the particle of interest is delivered to the region of high electric field intensity.

The second issue is the delivery of the nanoparticle close to the cavity. To characterize the sensing capabilities of the PhC cavities, we have addressed both of these issues by using a cylindrical nano-tip. This nano-tip can be approached close to the cavity and based on the superposition principle, different size of nanoparticles can be evaluated. Based on collected intensity variation due to the axial movement of nano-tip in the near field of the cavity, it is possible to emulate the nano-objects of various sizes by a superposition principle as shown in **Figure 4.10**.

The superposition principle relies on the variation in collected scattered intensity from the cavity surface due to the presence of the nano-tip at in the near field of the cavity. As shown in the **Figure 4.10**, the difference in the intensity collected at  $Z_1$  and  $Z_2$  position can provide the information about the signal variation induced by a nano-object of height  $(Z_1 - Z_2)$ . This measured intensity variation will

correspond to the variation predicted by the perturbation theory. If the nano-tip has cylindrical apex, then the subtraction in intensity at two different position will correspond to a nano-cylinder with  $(Z_1-Z_2)$  height. In order to ease the data analysis, we have chosen nano-tips with cylindrical apex. **Figure 4.5 (a)** shows the SEM image of the modified L3 which we have investigated with the nano-tip. **Figure 4.11 (a)** shows the map of intensity variation of the cavity when the nano-tip is in the near field of the cavity. This measurement was done with an apex diameter of 75 nm as show in **Figure 4.11 (b)**.

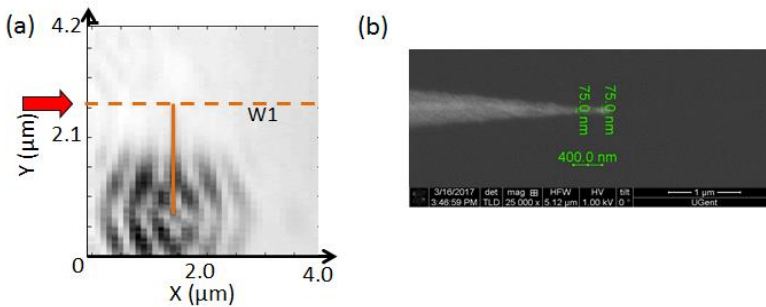


**Figure 4.11:** Measured map of the intensity variation induced by the interaction between the nano-tip fiber and the modified L3 cavity.

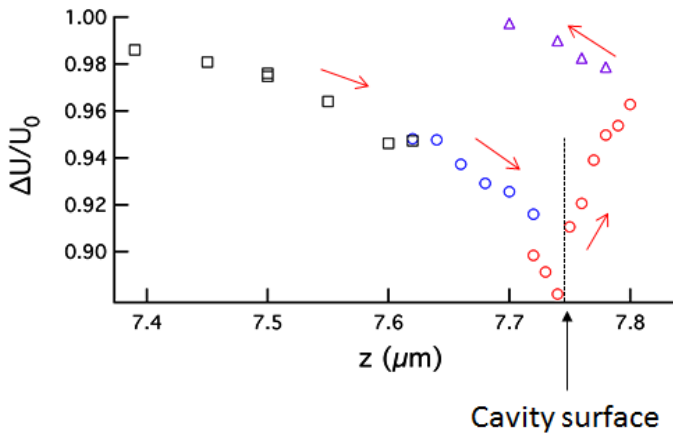


**Figure 4.12:** Measured intensity variation induced by the interaction between the nano-tip fiber and center of the modified L3 cavity along y direction at different axial position ( $z$ ).

The intensity variation along the center of the cavity along y direction at different axial position (z) is shown in the **Figure 4.12**. It can be clearly seen that as the tip approaches the cavity, exponential decay like behavior in the intensity is recorded. As it can be inferred from the plot, such a cavity can distinguish cylinders which has radius of 75 nm and is at least 5 nm high. When the tip touches the cavity surface, it might have broken which explains the offset in the collected intensity when the tip was moved further away from the cavity surface axially.

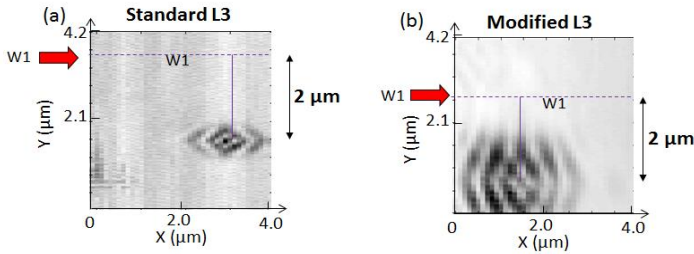


**Figure 4.13:** Comparison of the mapped mode volume between a standard L3 and modified L3.

## 4.5 Investigation of mode volume of PhC cavity using nano-tip

By mapping the mode of a cavity with a nano-tip, it is possible to experimentally retrieve the mode volume of the cavity. It can be seen from **Figure 4.13**, mode of modified L3 looks almost double compared to that of a standard L3. We did FDTD simulation to confirm our measurement results but the simulated data showed that both the cavities has similar mode volume. In order to understand this discrepancy, there is need of further investigate the impact of the access waveguide near the cavity.

## 4.6 Conclusion

This chapter discussed the detailed description of an advanced experimental setup that was built during this PhD project. It allows for visible and IR imaging of the chip. Spectral characterization of various cavities were presented by measuring their resonant wavelength from the transmission spectra. The set-up allows the collection of almost half of the scattered light via 0.95 NA objective lens from the cavity surface which is important for the intensity noise analysis. Later, we demonstrated the implementation of a technique to spatially characterize the interaction volume of PhC cavities with a silica fiber based nano-tip and investigated the interaction of PhC cavity field with such nano-tips.

## References

- [1] Akahane, Y., Asano, T., Song, B.S. and Noda, S., 2005. Fine-tuned high-Q photonic-crystal nanocavity. *Optics Express*, 13(4), pp.1202-1214.
- [2] Yamamoto, T., Notomi, M., Taniyama, H., Kuramochi, E., Yoshikawa, Y., Torii, Y. and Kuga, T., 2008. Design of a high-Q air-slot cavity based on a width-modulated line-defect in a photonic crystal slab. *Optics express*, 16(18), pp.13809-13817.
- [3] Bazylewski, P., Ezugwu, S. and Fanchini, G., 2017. A Review of Three-Dimensional Scanning Near-Field Optical Microscopy (3D-SNOM) and Its Applications in Nanoscale Light Management. *Applied Sciences*, 7(10), p.973.
- [4] Hopman, W.C.L., Hollink, A.J.F., De Ridder, R.M., Van Der Werf, K.O., Subramaniam, V. and Bogaerts, W., 2006. Nano-mechanical tuning and imaging of a photonic crystal micro-cavity resonance. *Optics express*, 14(19), pp.8745-8752.



# 5

## **Investigation of the intrinsic detection limit of photonic crystal cavities**

The accurate characterization of single nanoparticles in colloidal solutions in terms of their size and morphology is important for medical diagnostics and aerosol investigations. However, it is challenging to achieve a high throughput for very small (sub-100 nm) particles. In particular, it is not well established what the fundamental limits are on the trade-off between speed and the smallest detectable particle. In this chapter, we investigate these limits for photonic crystal (PhC) cavities. The first section provides a brief introduction on measurement principle of PhC cavity used in this chapter. In the second section, we investigate contribution from various noise levels on PhC cavity spectrum at small (30 ns) to large (0.7 ms) time scale. We investigate the variation of frequency fluctuation versus the Q factor at resonance frequency and at another frequency which is red shifted in the third section. In the fourth section, fundamental thermorefractive noise of such cavities which has different mode volumes are investigated. The fifth section provides the minimum detectable shift at different time scale which sets the ultimate intrinsic detection limit. The last section concludes this investigation and indicate that it is possible to monitor up to 33 million particles per second with a particle size down to 34 nm, making it a promising technique for fast real-time biosensing. This chapter is adapted from the manuscript which we published in Optica journal.

## 5.1 Introduction

Optical microcavities, such as microspheres, microtoroids, microring resonators, or photonic crystal (PhC) cavities [2,3] have enabled the noninvasive detection of biological molecules, reaching even the single molecule level for sensing based on high-quality factor (Q factor) whispering gallery (WG) modes [4]. Reaching sensitivities at the level of a single nanoparticle is now sparking the challenge of accurately tracking its motion at an acquisition time in line with its inertial time, in view of sensing fast chemical or biological events at the nanoscale [5,6].

Increasing the acquisition speed unfortunately jeopardizes the amount of collected information, and consequently the detection limit. In this context, integrated PhC cavities can play a key role, as they feature both high Q factor and small mode volume [7], and their specific design enables an efficient signal collection. Nevertheless, their intrinsic detection limit versus the acquisition speed of the sensing signal has not been experimentally unveiled up to now.

Here, we experimentally investigate and accurately quantify the trade-off between the acquisition time and the detection limit of integrated silicon PhC cavities. As a result, a frequency-shift noise level amounting to 1/2000th the linewidth of the cavity mode has been achieved for an acquisition time and a mode volume as small as 3  $\mu\text{s}$  and 0.06  $\mu\text{m}^3$ , respectively. Such a noise floor originates from the fundamental thermal fluctuations of the medium and sets the ultimate detection limit of dielectric optical cavities.

The principle of optical cavity sensors relies on detecting shifts of the resonant frequency  $\omega_0$  of the cavity. The frequency shifts are induced by local perturbations of the refractive index map due to the presence of the nanoparticle under investigation. Knowing the optical spectrum of the cavity mode, one fast approach to quantify any spectral shifts consists of recording the fluctuations of the intensity  $I^{\text{scat}}$  of a single frequency laser field scattered by the cavity. In this case, the refractive index perturbation triggers a dynamic detuning between the fixed laser field frequency  $\omega_p$  and the resonant frequency  $\omega_0$ , which results in intensity fluctuations of the scattered field. As a forerunner experiment towards single nanoparticle tracking, the temporal variations of the local density of nanoparticle solutions near a WG mode were monitored with a 5  $\mu\text{s}$  acquisition time by Keng *et al.* [8] for sizing purposes.

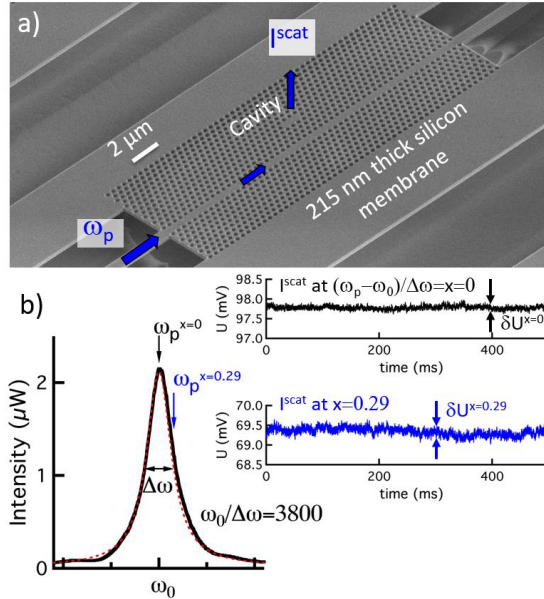


**Figure 5.1** (a) Scanning electron micrograph of the top surface of an integrated L3 PhC cavity. The silicon oxide has been removed below the 215 nm thick free-standing slab. The blue arrows indicate the light path of the pump laser beam at a frequency  $\omega_p$ . (b) Experimental optical spectrum of the cavity (dark curve) with the corresponding Lorentzian fit (red dotted curve) whose cavity linewidth is  $\Delta\omega = \omega_0/3800$ . The resonant frequency  $\omega_0$  corresponds to a wavelength of 1599.3 nm. On the right: Time traces of the photovoltage induced by the collected scattered light  $I_{\text{scat}}$  for a  $x = 0$  (black trace) and  $x = 0.29$  (blue trace) frequency detuning. Each of the traces is made of 50,000 equidistant data points.

Using a high-quality-factor WG mode to retrieve reliable quantitative information about the fast Brownian motion of a single colloidal nanoparticle only from induced intensity fluctuations is difficult due to the presence of splitting and broadening of the mode spectrum that add to the expected frequency shift. In addition, implementing high-Q cavities requires a careful stabilization of the exciting laser source. To overcome these issues, we focus here on nondegenerate PhC cavity modes of sufficiently low Q factor and small mode volume  $V_{\text{eff}}$  [9], such as the fundamental mode of the L3 cavity presented in **Figure 5.1**.

## 5.2 Experiment

A standard L3 PhC cavity is defined by removing three adjacent holes from a triangular lattice in the  $\Gamma K$  direction, i.e., in the direction of the in-plane blue arrows in **Figure 5.1(a)**. A W1 (line defect) PhC waveguide, created by removing

one line of holes also in the  $\Gamma K$  direction and separated by four lines of holes from the L3 defect, ensures the excitation of the fundamental resonant cavity mode. The light intensity  $I^{\text{scat}}$  that is scattered out-of-plane by the cavity is collected through a high-numerical-aperture ( $NA = 0.95$ ) microscope objective and detected with a fast photodiode. A fast oscilloscope records the photo voltage  $U$  generated by the photodiode (see Section 7). By analyzing the noise on  $U$ , our purpose is to experimentally identify the main constraints on the acquisition speed and the minimal frequency shift that is detectable with a PhC cavity of a given  $Q$  factor and mode volume. The quality factor  $Q$  is defined as the ratio between the resonant frequency  $\omega_0$  and the linewidth  $\Delta\omega$  of the optical spectrum of the cavity coupled to the access W1 waveguide.

As revealed by the black and blue temporal traces in **Figure 5.1(b)**, the photovoltage  $U$  induced by the scattered intensity  $I^{\text{scat}}$  at a load resistance  $R_{\text{load}} = 11.8 \text{ k}\Omega$  is subject to temporal fluctuations even without any intentional extrinsic perturbations of the PhC cavity. The origin of the observed noise is of diverse nature, as recently theoretically investigated in [10,11]. The most relevant noise contributions are the thermal noise in the load resistance (Johnson noise), the shot noise, the relative intensity noise (RIN) of the laser source, the frequency noise of the laser source, the thermorefractive noise resulting from the fundamental thermal fluctuations, and the noise contribution resulting from any mechanical vibrations. Some of these contributions are not intrinsic to the cavity, such as the noise contributions related to the laser pump, the photodetector, and the mechanical vibrations.

Importantly, the standard deviation  $\delta U$  of these fluctuations that is reported in **Figure 5.1(b)** depends on the detuning between the frequencies of the pump and of the cavity resonance,  $x = (\omega_p - \omega_0)/\Delta\omega = \delta\omega_p/\Delta\omega$ . For zero detuning  $x = 0$ , the noise is 3 times lower than in the case of a blue-shifted detuning  $x = 0.29$ , which is the optimal value for sensing intensity variations induced by a cavity frequency shift. It implies that the intensity noises related to the laser source, the photodetection, and mechanical environment are not the main contributions at  $x = 0.29$ . The dependence of the noise on the detuning  $x$  is in line with a frequency noise, either on  $\omega_0$  or on  $\omega_p$ .

To highlight the impact of the different contributions to the noise level, we have measured the scattered intensity  $I^{\text{scat}}$  for different load resistances. Lowering the load resistance decreases the possible acquisition sampling time  $t_{\text{acq}}$  at the expense of a lower signal voltage  $U$ . We define here the acquisition sampling time  $t_{\text{acq}}$  as the minimal response time that is needed to reach 99% of the average value of a steady state under a step variation of the signal. For a load resistance of  $1 \text{ M}\Omega$ ,  $t_{\text{acq}} = 0.7 \text{ ms}$ , whereas for  $560 \text{ }\Omega$ , the acquisition sampling time drops to  $0.7 \text{ }\mu\text{s}$  [12].

In **Figure 5.2**, the noise-to-signal ratio of the photo voltage, defined as the ratio of the standard deviation  $\delta U$  to the average voltage  $U$ , is plotted versus the load resistance and the acquisition sampling time for a pump frequency in resonance with the frequency of the cavity  $\omega_0$  ( $x = 0$ ), see black data points with error bars, and for a detuning  $x = 0.29$ , see blue data points. The values of  $\delta U/U$  are determined from temporal signal traces similar to the ones in **Figure 5.1(b)**.

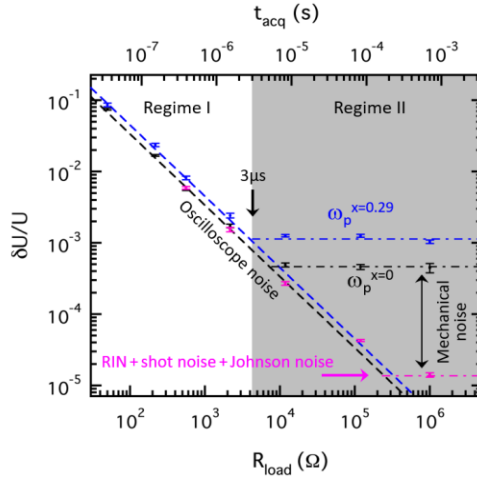


**Figure 5.2.** Noise-to-signal ratio  $\delta U/U$  of the photovoltage  $U$  induced by the radiated field from the PhC cavity versus the load resistance  $R_{\text{load}}$  of the photodetector, and the corresponding acquisition sampling time  $t_{\text{acq}}$  for pump frequency detuning of  $x = 0$  (dark points) and  $x = 0.29$  (blue points). The error bars correspond to the standard deviation of ten repeated measurements. The black and blue dashed lines correspond to the noise limit imposed by the oscilloscope for  $x = 0$  and  $x = 0.29$ , respectively. The collected powers measured at resonance with  $R_{\text{load}} = 1 \text{ M}\Omega$  for  $x = 0$  and  $x = 0.29$  are  $8 \mu\text{W}$  and  $6 \mu\text{W}$ , respectively. Purple data points: noise-to-signal ratio without any PhC cavity between the laser source and the photodetector for the same collected power, as in the case of  $x = 0$ . The gray area corresponds to a regime limited by the fundamental thermo-optic noise.

For a load resistance of  $1 \text{ M}\Omega$ , the average photovoltage  $U$  amounts to  $8 \text{ V}$  for  $x = 0$  and  $6 \text{ V}$  for  $x = 0.29$ . Considering that the responsivity of the photodetector is  $G \sim 1 \text{ A/W}$ , the collected power at resonance is  $8 \mu\text{W}$ . In both cases, two regimes take place: for  $t_{\text{acq}} < 3 \mu\text{s}$ ,  $\delta U/U$  decreases linearly (regime I), whereas for  $t_{\text{acq}} > 3 \mu\text{s}$ , it is independent of the acquisition sampling time (regime II). As confirmed by the black and blue dashed lines, regime I can be explained by taking into account the standard deviation  $\delta U_{\text{osc}} = 30 \mu\text{V}$  of the electronic noise of the fast oscilloscope. In this regime, the noise-to-signal ratio drops by increasing the value of the collected signal. In regime II, which is indicated by the gray area, the

noise at resonance ( $x = 0$ ) is larger than the expected contribution from the sum of the RIN of the laser source, the shot noise, and the Johnson noise. The purple data points correspond to this sum of noise contributions. We attribute the difference between the noise floor level measured at  $x = 0$  (black data points) and the intensity noise floor of the laser source to the intensity instability induced by the mechanical vibrations of the setup.

### 5.3 Cavity spectral noise

The noise-to-signal ratio can be separated into two contributions as  $(\delta U/U)^2 = (\delta U/U)^2|_{\delta\omega} + (\delta U/U)^2|_I$ . The first contribution is associated to fluctuations of the scattered intensity  $\delta I^{\text{scat}}$  that are triggered by a frequency noise  $\delta\omega$ , whereas  $\delta U/U|_I$  takes into account all other sources of noise. The intensity variation  $\delta I^{\text{scat}}$  is related to the frequency shift of the perturbed cavity via the envelope of the cavity mode spectrum.

Our goal is to express the relative voltage fluctuation  $\delta U/U$  in function of the frequency fluctuations  $\delta\omega$  of the cavity resonance. Setting,  $a = 1/4Q_iQ_c$  and  $b = 1/4Q^2$ , where  $Q_i$  is the intrinsic cavity quality factor, i.e. the quality factor of the photonic crystal cavity free of any access waveguides, and  $Q_c$  the quality factor resulting from the in-plane coupling, the spectral response of the cavity is given by:

$$S(\omega_0, \omega_p) = \frac{a}{(\omega_p - \omega_0)/\omega_0)^2 + b} \quad (5.1)$$

Introducing  $I^{\text{in}}$  as the incident power in the access waveguide coupled to the cavity and  $I^{\text{scat}}$  as out of plane scattered intensity,  $I^{\text{scat}} = \frac{a}{b} I^{\text{in}}$  at zero detuning, i.e.  $x = 0$ , the equation 5.1 can be rewritten as

$$S(\omega_0, \omega_p) = \frac{b}{(\omega_p - \omega_0)/\omega_0)^2 + b} \frac{I^{\text{scat}}}{I^{\text{in}}} \quad (5.2)$$

$$S(\omega_0, \omega_p) = \frac{1/4Q^2}{(\omega_p - \omega_0)/\omega_0)^2 + 1/4Q^2} \frac{I^{\text{scat}}}{I^{\text{in}}} \quad (5.3)$$

The fluctuation of the scattered intensity for a given variation of the cavity frequency  $\delta\omega$  can be expressed as:

$$\frac{\delta I^{\text{scat}}}{I^{\text{in}}} = -S(\omega_0, \omega_p) + S(\omega_0 + \delta\omega, \omega_p) \quad (5.4)$$

Using  $x = \frac{\omega_p - \omega_0}{\Delta\omega}$  provides a simplified expression of the two following quantities that are involved in the development of equation 5.2:

$$\left(\frac{\omega_p - \omega_0}{\omega_0}\right)^2 = 4bx^2, \quad (5.5)$$

$$\left(\frac{\omega_p - \omega_0 - \delta\omega}{\omega_0 + \delta\omega}\right)^2 = 4b\left(\frac{x - \delta\omega/\Delta\omega}{(1 + \delta\omega/\Delta\omega)/Q}\right)^2 \quad (5.6)$$

It follows:

$$\frac{\delta I^{\text{scat}}}{I^{\text{in}}} = -\frac{1}{1 + 4x^2} + \frac{1}{1 + 4\left(\frac{x - \delta\omega/\Delta\omega}{(1 + \delta\omega/\Delta\omega)/Q}\right)^2} \quad (5.7)$$

The intensity that is measured without fluctuations for a given detuning  $x$  is  $I^{\text{scat}}|_x = \frac{1}{1 + 4x^2} I^{\text{scat}}$ , which implies:

$$\frac{\delta I^{\text{scat}}}{I^{\text{scat}}|_x} = -1 + \frac{1 + 4x^2}{1 + 4\left(\frac{x - \delta\omega/\Delta\omega}{(1 + \delta\omega/\Delta\omega)/Q}\right)^2} = \delta U/U|_{\delta\omega} \quad (5.8)$$

Measuring the noise-to-signal ratio at  $x = 0$  and  $x = 0.29$  allows us to retrieve the experimental values of the relative frequency noise  $\delta\omega/\Delta\omega = 5.8 \pm 0.5 \times 10^{-4}$ , and of the contribution  $\delta U/U|_1 = 4.5 \pm 0.5 \times 10^{-4}$ . The laser source has a spectral linewidth of 200 kHz. It corresponds to a relative frequency noise  $\delta\omega/\Delta\omega|_{\text{laser}} = 4 \times 10^{-6}$ , which is 2 orders of magnitude smaller than the retrieved experimental value. Consequently, we attribute the current spectral noise to the thermorefractive noise, which is also supported by **Figure 5.3**.

In **Figure 5.3**, we compare the ratio  $\delta U/U$  for three different L3 cavities, including the one of  $Q = 3800$  studied in **Figure 5.1**, and for  $x = 0$  and  $x = 0.29$ . One of these cavities has a  $Q$  factor of 2200, and differs from the previous one by its separation of three lines of holes between the W1 access waveguide and the cavity defect. This cavity operates almost in the optimal coupling condition based on simulation of the intrinsic  $Q$  factor of the cavity. For the third cavity, whose  $Q$

factor amounts to 16,800 and whose coupling is identical to the one of the cavity of  $Q = 3800$ , the first three holes located on both sides of the line defect have been slightly laterally shifted away from the core by a length of  $(0.2 a, 0.025 a, 0.2 a)$ , as initially proposed in [13,14].

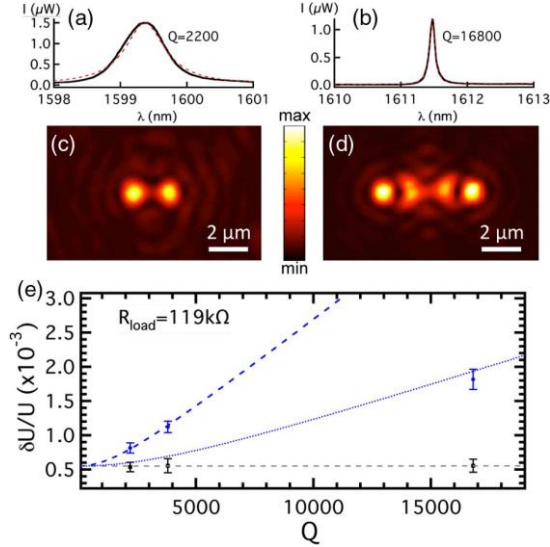


**Figure 5.3** (a) and (b) Optical spectra of L3 PhC cavities with  $Q = 2200$  and  $Q = 16800$ , respectively. The red dotted lines are Lorentzian fits. (c) and (d) Near-infrared optical images of the resonant field radiated from the  $Q = 2200$  and  $Q = 16800$  PhC cavities, respectively. (e) Noise-to-signal ratio  $\delta U/U$  of the photo voltage  $U$  versus the quality factor for  $x = 0$  (black dashed line) and  $x = 0.29$  (blue dashed line) with a load resistance of  $R_{\text{load}} = 119 \text{ k}\Omega$ . Black and blue dashed lines are expected variations with the effective mode volume of the  $Q = 3800$  cavity. The blue dotted line is the expected variation with the effective mode volume of the  $Q = 16800$  cavity. The collected power at  $x = 0$  is  $0.17 \mu\text{W}$ .

No variation of the ratio  $\delta U/U$  versus the  $Q$  factor is observed for  $x = 0$ . On the other hand, the case  $x = 0.29$  exhibits an increasing variation of  $\delta U/U$  versus the  $Q$  factor. Both trends are expected for a constant and sufficiently small frequency noise. As regards the cavity of  $Q = 16,800$ , its  $\delta U/U$  value is nevertheless 2.4 times smaller than the expected value from **equation (5.8)** (see blue dashed line in **Figure 5.3**). The origin of this departure lies in the larger mode volume of this cavity as explained below. The difference in mode volume is revealed by a larger spatial distribution of the intensity of the cavity mode in **Figure 5.3(d)** compared to the one of the cavities of lower  $Q$  in **Figure 5.3(c)**. Note that the impact of the volume on  $\delta U/U$  definitely excludes any major contribution of the laser frequency  $\omega_p$  noise.

## 5.4 Fundamental thermorefractive noise

Any medium of density  $\rho$  in thermal equilibrium at a temperature  $T$  is subject to fundamental thermal fluctuations [15]. The variance of these fluctuations in a local volume  $V$  of the medium is given by  $\delta T^2 = \frac{k_B T^2}{(\rho V) C_V}$ , where  $k_B$  is the Boltzmann constant  $C_V$  the heat capacity at constant volume. The thermal fluctuations  $\delta T$  within the cavity mode volume induce a frequency noise on the resonant frequency  $\omega_0$  of the cavity. It results from the perturbation of the dielectric constant of the medium that depends on the temperature via the optical index  $n$  and the thermo-optic coefficient  $\partial n / \partial T$  [16]. Based on a perturbation approach, the relative frequency noise is given by

$$\frac{\delta \omega}{\Delta \omega} = \frac{Q \delta \omega}{\omega_0} = \frac{Q}{n} \left( \frac{\partial n}{\partial T} \right) \sqrt{\frac{k_B T^2}{(\rho V_{ovl}) C_V}} \quad (5.9)$$

where  $V_{ovl}$  is an interaction overlap volume between the cavity mode and the thermal fluctuations [17]. For a cavity mode of electric field distribution  $E$ , the volumes  $V_{eff}$  and  $V_{ovl}$  are functions of  $|E|^2$  and  $|E|^4$ , respectively.

Assuming a Gaussian distribution of the cavity field intensity,  $V_{ovl} = 2\sqrt{2} V_{eff}$ . Based on the experimental value of the relative frequency noise  $\delta \omega / \Delta \omega = 5.8 \pm 0.5 \times 10^{-4}$ , the thermo-optic coefficient of the silicon  $\partial n / \partial T = 1.8 \pm 0.5 \times 10^{-4}$ , [18] and the effective optical index of the silicon slab waveguide  $n = 2.74$  [19], we obtain  $V_{ovl} = 0.13 \mu\text{m}^3$ , which is of the same order of magnitude as  $2 \sqrt{V_{eff}} = 0.17 \mu\text{m}^3$ .

Achieving the fundamental thermodynamic noise level with passive optical systems based on large effective mode volumes, such as in optical fiber sensors [20–23], is challenging in general, as it requires ultrastable laser sources. With PhC cavities, the effective mode volume is small enough to boost the thermodynamic noise level beyond the noise level of standard diode-laser sources. In particular, advanced lock-in techniques [24] are superfluous with these cavities.

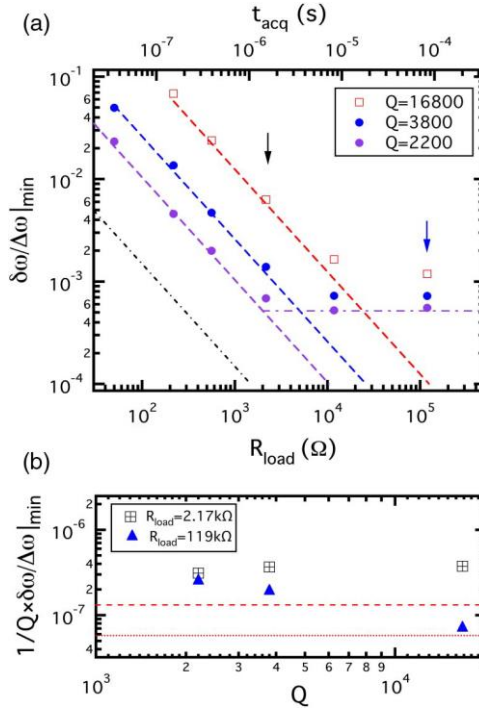


**Figure 5.4:** (a) Square and circle symbols are the minimum relative frequency shift that can be detected versus the load resistance  $R_{\text{load}}$ , and the corresponding acquisition time  $t_{\text{acq}}$  for three different quality factors  $Q$  with the same input power and the same frequency detuning  $x = 0.29$ . The purple, blue, and red dashed lines are oscilloscope noise limits for the powers of 15, 6, and 1.25  $\mu\text{W}$  that are collected with  $R_{\text{load}} = 1 \text{ M}\Omega$  for each cavity, respectively. Dark dot-dashed line is the oscilloscope noise for an optimal light collection. The purple dot-dashed line pinpoints the saturation level due to the thermal and mechanical noise for  $Q = 2200$ . (b) Minimum relative frequency shift normalized to the quality factor for two load resistances pinpointed by the black and blue arrows in (a). The red dashed line and dotted line are the fundamental thermal noise limits associated with a fundamental mode volume of  $V_{\text{eff}} = 0.060 \mu\text{m}^3$  (i.e., for  $Q = 2200$  and  $Q = 3800$ ) and  $V_{\text{eff}} = 0.126 \mu\text{m}^3$  (i.e., for  $Q = 16800$ ), respectively.

From the experimental near-field pattern of the cavity modes [25], we have estimated the effective mode volume and the interaction overlap volume of the  $Q = 16,800$  cavity mode to be 2.1 and 5.2 times larger than the corresponding ones of the standard L3 cavity, respectively. The factor 2.1 is in agreement with the far-field real-space images of the intensity distribution of the cavity modes in **Figure 5.3(a)** and **5.3(b)**. Considering that the frequency noise varies with the square root of the overlap volume  $\sqrt{V_{\text{ovl}}}$ , the factor  $\sqrt{5.2} \approx 2.3$  explains the drop of  $\delta U/U$  by a factor 2.4 for the cavity of  $Q = 16,800$ . The extended mode volume

of this cavity, whose theoretical intrinsic Q factor amounts to 65000 for the current slab thickness, is attributed to a strong coupling with the W1 waveguide.

## 5.5 Ultimate detection limit

The measured voltage noise  $\delta U/U$  allows us to define an ultimate minimal relative frequency shift  $\delta\omega/\Delta\omega|_{min}$ . Any frequency shift that is induced by a nanoparticle located in the surrounding of the cavity mode can be distinguished from the noise with a probability larger than 68%, i.e., “one-sigma” confidence interval, if it is larger than one time  $\delta\omega/\Delta\omega|_{min}$ . The minimal frequency noise that takes into account not only the intrinsic frequency noise, but also any extrinsic intensity noise of the signal, is given by

$$\frac{\delta\omega}{\Delta\omega}|_{min} = -Q + \frac{x + Q}{1 + (2Q)^{-1}\sqrt{(4x^2 + 1)/(1 + \delta U/U)} - 1} \quad (5.10)$$

It depends on the detuning  $x$ , and for a fixed  $\delta U < 0.01 U$  reaches a minimal value for  $x \approx 0.29$ . This figure of merit is plotted in **Figure 5.4(a)** versus the acquisition sampling time for  $x = 0.29$  and for the three cavities [26].

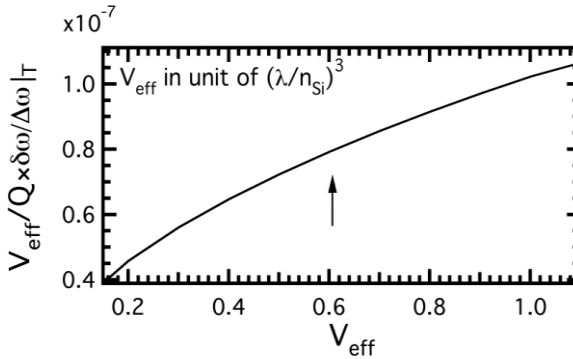


**Figure 5.5:** Relative frequency shift  $\delta\omega/\Delta\omega|_T$  induced by the fundamental thermal noise normalized to  $Q/V_{eff}$  versus the effective cavity mode volume  $V_{eff}$ . This quantity is proportional to the minimal nanoparticle volume that the sensor can detect when the fundamental thermal noise limit is reached. The arrow pinpoints the value for the standard L3 PhC cavity.  $V_{eff}$  is normalized to  $(\lambda/n_{Si})^3$  where  $n_{Si}$  is the index of the silicon material and the wavelength  $\lambda = 1.6 \mu\text{m}$ .

The three cavities are excited with the same power of 15.6 mW at the input of the photonic chip. In term of frequency noise, the cavity with the lowest Q factor

outperforms the other ones in the regime that is governed by the oscilloscope noise. It results from a better light coupling. A figure of merit of 1/45 is achievable with an acquisition sampling time of 30 ns. When  $t_{acq} > 2 \mu\text{s}$ , the figure of merit reaches 1/2000, which is 1 order of magnitude larger than the values reported in [27].

Note that the signal inside the numerical aperture of the collection path of the setup is attenuated by a factor of 7 until the photodetector, mainly due to the transmission through the high-NA microscope objective and a 50/50 beam splitter. The dot dashed line corresponds to the expected oscilloscope noise limit in the case of the cavity of  $Q = 2200$ , but without this extrinsic attenuation factor that can be cancelled by integrating the photodetector directly on chip. In this case, a figure of merit of 1/2000 is reachable with an acquisition sampling time of 100 ns.

Based on the knowledge of the figure of merit, the minimal nanoparticle volume  $V_{part}^{min}$  that is detectable can be estimated from a first-order perturbation approach by considering the photonic system as a closed system. The relative frequency shift induced by the modification  $\delta\epsilon$  of the refractive index map due to the presence of the nanoparticle at a location where the cavity field intensity is  $\|E_{part}\|^2$  can be approximated by

$$\left. \frac{\delta\omega}{\omega_0} \right|_{pert} = -\frac{1}{2} \frac{\delta\epsilon}{\epsilon_c + \delta\epsilon} \frac{V_{part}}{V_{eff}} \frac{\|E_{part}\|^2}{\|E_{max}\|^2} \quad (5.11)$$

with  $\epsilon_c$  the unperturbed dielectric constant at the position of the dielectric perturbation, namely the nanoparticle. **Equation (5.11)** is a good approximation for high-Q cavities, i.e., when any energy dissipation is neglected. As discussed in [28] and references therein, in the case of strong radiation leakage or absorption, the standard effective mode volume can be replaced by a generalized mode volume that takes into account the complex nature of the wave vector of the mode. In the following, we adopt the closed system approximation in view of the high quality factor of the current cavities. As a result, the minimal particle volume can be expressed as

$$V_{part}^{min} = 2 \frac{\epsilon_c + \delta\epsilon}{\delta\epsilon} \frac{\|E_{max}\|^2}{\|E_{part}\|^2} \frac{V_{eff}}{Q} \left. \frac{\delta\omega}{\Delta\omega} \right|_{min} \quad (5.12)$$

It follows that  $V_{part}^{min}/V_{eff} \propto \frac{\delta\omega}{\Delta\omega}|_{min}/Q$ , which is plotted in **Figure 5.4(b)** versus the Q factor for the three cavities, and for the two different regimes pinpointed by the blue ( $R_{load} = 119 \text{ k}\Omega$ ) and black arrows ( $R_{load} = 2.17 \text{ k}\Omega$ ) in **Figure 5.4(a)**.

In the regime limited by the electronic noise (see black squares with cross) the cavity of  $Q = 2200$  allows detection of the smallest particle, whereas in the regime limited by the thermal noise (blue triangles), increasing the quality factor improves the detection limit. This improvement comes from a relative drop of the noise contribution due to extrinsic intensity noise  $(\delta U/U)|_I$ .

As revealed by the red dashed line that corresponds to the previously determined intrinsic thermal noise limit,  $V_{part}^{min}/V_{eff}$  is independent of Q, and equal to a constant of  $1.3 \times 10^{-7}$  for the mode volume of the cavities of quality factor 2200 and 3800. This constant drops to  $5.8 \times 10^{-8}$  for the cavity of quality factor 16,800 due to a larger mode volume (see red dotted line). Although the thermal frequency noise  $\delta\omega/\Delta\omega|_T$  is lower for larger effective mode volume, it does not mean that a larger  $V_{eff}$  leads to a better detection limit for nanoparticle sensing, as indicated in **Figure 5.5**.

In **Figure 5.5**, the ultimate relative frequency shift  $\delta\omega/\Delta\omega|_T$  [see **Equation 5.9**] that corresponds to the fundamental thermal noise limit has been normalized to  $Q/V_{eff}$  and plotted versus the effective mode volume.  $V_{eff}/Q \times \delta\omega/\Delta\omega|_T$ , which is proportional to the ultimate minimal detectable nanoparticle volume, follows a square root variation when the fundamental thermal limit is reached. The square root variation of the thermal frequency noise, i.e., its sublinear variation, versus the effective mode volume implies that  $V_{eff}$  still needs to be minimized to improve the detection limit in the case of single nanoparticle sensing. In contrast, the quality factor has no impact on the detection limit when the fundamental thermal limit has been reached [see **Figure 5.4(b)**].

Based on our experimental determination of the minimal relative frequency shift  $\delta\omega/\Delta\omega|_{min}$ , we can estimate the minimal size of a colloidal nanoparticle that can be detected for a given acquisition speed. We consider the case of a single silica nanoparticle in air and of a biological nanoparticle in water. In the case of a single silica nanoparticle ( $n_{SiO_2} = 1.44$ ) located in the air at a position of 10 nm from the surface of the silicon membrane, and at the smallest distance from the maximum value of the cavity field intensity, which corresponds to  $\frac{|E_{max}|^2}{|E_{part}|^2} \simeq 1.76$ , the minimum detectable equivalent spherical radius within a 1-sigma confidence interval is  $r_{SiO_2}^{min} = 5.5 \text{ nm}$  for the cavity of  $Q = 3800$  and  $t_{acq} = 10 \text{ }\mu\text{s}$  and  $r_{SiO_2}^{min} =$

4.8 nm when the fundamental thermal limit is reached [see red dashed line in **Figure 5.4(b)**]. It rises to 7.0 nm for a 3-sigma confidence interval.

With  $t_{\text{acq}} = 30$  ns, our current experimental limit provides  $r_{\text{SiO}_2}^{\text{min}} = 5.5$  nm/30.3 nm for the 1-sigma/3-sigma confidence interval. By optimizing the light collection [see black dot-dashed line in **Figure 5(a)**], a detection limit of  $r_{\text{SiO}_2}^{\text{min}} = 10$  nm with  $t_{\text{acq}} = 30$  ns is achievable. Considering the density of silica to be 2.65 g/cm<sup>3</sup>, the corresponding mass of a 10 nm silica particle is around 11 ag. As regards a biological nanoparticle in water ( $n_{\text{water}} \sim 1.3$ ), e.g., an extracellular vesicle such as an exosome [29,30] ( $n \sim 1.5$ ), the optical index contrast is  $\sim 0.2$ , which leads to  $r_{\text{bio}}^{\text{min}} \simeq 5.4$  nm/7.8 nm for the 1-sigma/3-sigma confidence interval and  $t_{\text{acq}} = 10$   $\mu$ s. Typical density of an exosome is around 1.22 g/cm<sup>3</sup> which corresponds to mass to be 0.8 ag/2.3 ag for exosome with radius of 5.4 nm/7.8 nm. Such values rely on the assumption that water does not induce extra fluctuations. For  $t_{\text{acq}} = 30$  ns, the minimum equivalent spherical radius drops to  $r_{\text{bio}}^{\text{min}} \simeq 23.3$  nm/33.7 nm for the 1-sigma/3-sigma confidence interval which corresponds to the mass of 71 ag/216 ag.

## 5.6 Conclusion

To conclude, we have quantified the intrinsic detection limit of integrated PhC cavities and identified the main limiting factors. Importantly, for an effective mode volume of 0.06  $\mu\text{m}^3$  we have reached a value  $\delta\omega/\Delta\omega|_{\text{min}} = 1.9 \times 10^{-7} \times Q$ , which is very close to the ultimate limit  $\delta\omega/\Delta\omega|_T = 1.3 \times 10^{-7} \times Q$  that is imposed by the fundamental thermodynamic fluctuations at room temperature. We have well posed the problem of the detection limit by considering the acquisition sampling time, and in a similar way to [11] we propose  $\frac{V_{\text{eff}}}{Q} \times \frac{\delta\omega}{\Delta\omega}|_{\text{min}} \times t_{\text{acq}}$  as a relevant figure of merit to compare the performance of optical cavity sensors. When dissipation effects are not negligible, for instance, for the case of plasmonic resonances,  $V_{\text{eff}}$  can be replaced by a generalized mode volume as introduced in [28]. The fundamental noise limit is currently reached for an acquisition sampling time  $t_{\text{acq}} \geq 3$   $\mu$ s. Improving the amount of light collected out of the cavity is necessary to further push the minimal acquisition sampling time. The current study makes it possible to answer the question: what is the trade-off between the acquisition speed and the detection limit to track a nanoparticle in real time with a resonant cavity field. In particular, our study shows that a single PhC cavity enables us to monitor up to 33 million particles per second with a particle size down to 34 nm with the currently achieved experimental conditions, and down to 10 nm by optimizing the light collection. From another point of view,

knowing the value of the ultimate intrinsic noise level allows tracking of the origin of any extrinsic fluctuations that are larger than the thermal fluctuations. For instance, fundamental fluctuations in liquid can, in principle, be investigated at the nanoscale, and with a temporal resolution of few nanoseconds by using a PhC cavity. In this context, we envision that our methodology will be of high interest for identifying the ultimate performances of optical biosensors and airborne nanoparticle sensors. Moreover, as the Brownian motion of single nanoparticles is dependent on the morphology of the nanoparticle, their tracking via the intensity fluctuations of a cavity mode has the potential for an unprecedentedly accurate and noninvasive characterization of colloidal solutions. Our approach can circumvent limitations intrinsic to fluorescence correlation spectroscopy [31]. In general terms, our experimental results suggest that implementing an integrated dynamic light scattering technique [32] is feasible with PhC cavities, which can trigger a major impact in the field of medical diagnostics and for the analysis of hazardous aerosols.

## References

- [1] Saurav, K. and Le Thomas, N., 2017. Probing the fundamental detection limit of photonic crystal cavities. *Optica*, 4(7), pp.757-763.
- [2] Vahala, K.J., 2003. Optical microcavities. *nature*, 424(6950), p.839.
- [3] Scullion, M.G., Krauss, T.F. and Di Falco, A., 2013. Slotted photonic crystal sensors. *Sensors*, 13(3), pp.3675-3710.
- [4] Vollmer, F., Arnold, S. and Keng, D., 2008. Single virus detection from the reactive shift of a whispering-gallery mode. *Proceedings of the National Academy of Sciences*, 105(52), pp.20701-20704.
- [5] Rosenblum, S., Lovsky, Y., Arazi, L., Vollmer, F. and Dayan, B., 2015. Cavity ring-up spectroscopy for ultrafast sensing with optical microresonators. *Nature communications*, 6, p.6788.
- [6] Tardif, M., Jager, J.B., Marcoux, P.R., Uchiyama, K., Picard, E., Hadji, E. and Peyrade, D., 2016. Single-cell bacterium identification with a SOI optical microcavity. *Applied Physics Letters*, 109(13), p.133510.
- [7] Priolo, F., Gregorkiewicz, T., Galli, M. and Krauss, T.F., 2014. Silicon nanostructures for photonics and photovoltaics. *Nature nanotechnology*, 9(1), p.19.
- [8] Keng, D., McAnanama, S.R., Teraoka, I. and Arnold, S., 2007. Resonance fluctuations of a whispering gallery mode biosensor by particles undergoing Brownian motion. *Applied Physics Letters*, 91(10), p.103902.
- [9] From the local intensity  $|E|^2$  of the cavity mode and the dielectric map  $\epsilon$  of the photonic structure, the effective volume can be defined as  $V_{\text{eff}} = \int \epsilon |E|^2 dV / \max\{\epsilon |E|^2\}$ , where the max function takes the maximum value over the entire space. The numerical value  $V_{\text{eff}} = 0.06 \mu\text{m}^3$  has been determined with a finite difference time-domain method.

- [10] Zhou, X., Zhang, L. and Pang, W., 2016. Performance and noise analysis of optical microresonator-based biochemical sensors using intensity detection. *Optics express*, 24(16), pp.18197-18208.
- [11] Hu, J., Sun, X., Agarwal, A. and Kimerling, L.C., 2009. Design guidelines for optical resonator biochemical sensors. *JOSA B*, 26(5), pp.1032-1041.
- [12] Note that the current definition of the acquisition time is much more restrictive than the conventional definition of the rise time, which amounts to 6  $\mu$ s for a load resistance of 1 M $\Omega$  with the current photodetector bandwidth of 1.2 GHz at  $R_{load}=50 \Omega$ .
- [13] Akahane, Y., Asano, T., Song, B.S. and Noda, S., 2003. High-Q photonic nanocavity in a two-dimensional photonic crystal. *Nature*, 425(6961), p.944.
- [14] Akahane, Y., Asano, T., Song, B.S. and Noda, S., 2005. Fine-tuned high-Q photonic-crystal nanocavity. *Optics Express*, 13(4), pp.1202-1214.
- [15] Landau, L.D., Lifshitz, E.M. and Pitaevskii, L.P., 1980. *Statistical physics*, part I.
- [16] In view of the value of the thermal expansion coefficient of the silicon, the impact of the density fluctuations can be neglected here.
- [17] Gorodetsky, M.L. and Grudinin, I.S., 2004. Fundamental thermal fluctuations in microspheres. *JOSA B*, 21(4), pp.697-705.
- [18] Komma, J., Schwarz, C., Hofmann, G., Heinert, D. and Nawrodt, R., 2012. Thermo-optic coefficient of silicon at 1550 nm and cryogenic temperatures. *Applied Physics Letters*, 101(4), p.041905.
- [19] As a first-order approximation, we assume that mode is located within a homogeneous medium whose index equals the effective index of the 215 nm thick silicon slab waveguide. The optical index of the silicon is 3.45.
- [20] Gagliardi, G., Salza, M., Avino, S., Ferraro, P. and De Natale, P., 2010. Probing the ultimate limit of fiber-optic strain sensing. *Science*, 330(6007), pp.1081-1084.
- [21] Cranch, G.A. and Foster, S., 2012. Comment on "Probing the Ultimate Limit of Fiber-Optic Strain Sensing". *Science*, 335(6066), pp.286-286.
- [22] Gagliardi, G., Salza, M., Avino, S., Ferraro, P. and De Natale, P., Response to Comment on " Probing the Ultimate Limit of Fiber-Optic Strain Sensing, 2012. *Science* 335, p286.
- [23] Dong, J., Huang, J., Li, T. and Liu, L., 2016. Observation of fundamental thermal noise in optical fibers down to infrasonic frequencies. *Applied Physics Letters*, 108(2), p.021108.
- [24] Knittel, J., Swaim, J.D., McAuslan, D.L., Brawley, G.A. and Bowen, W.P., 2013. Back-scatter based whispering gallery mode sensing. *Scientific reports*, 3, p.2974.
- [25] We have implemented a scanning near-field technique making use of silica nanotips to map the cavity near field, which will be discussed elsewhere.
- [26] Note that even if the total quality factor appears as a parameter in Equation 5.10, it has no impact on  $\delta\omega/\Delta\omega|_{min}$ , as expected from the normalization by  $\Delta\omega$ , which confers to this quantity a figure of merit character.
- [27] Vollmer, F. and Yang, L., 2012. Review Label-free detection with high-Q microcavities: a review of biosensing mechanisms for integrated devices. *Nanophotonics*, 1(3-4), pp.267-291.

- 
- [28] Yang, J., Giessen, H. and Lalanne, P., 2015. Simple analytical expression for the peak-frequency shifts of plasmonic resonances for sensing. *Nano letters*, 15(5), pp.3439-3444.
- [29] Andaloussi, S.E., Mäger, I., Breakefield, X.O. and Wood, M.J., 2013. Extracellular vesicles: biology and emerging therapeutic opportunities. *Nature reviews Drug discovery*, 12(5), p.347.
- [30] Théry, C., Ostrowski, M. and Segura, E., 2009. Membrane vesicles as conveyors of immune responses. *Nature reviews immunology*, 9(8), p.581.
- [31] Eigen, M. and Rigler, R., 1994. Sorting single molecules: application to diagnostics and evolutionary biotechnology. *Proceedings of the National Academy of Sciences*, 91(13), pp.5740-5747.
- [32] Berne, B.J. and Pecora, R., 1976. *Dynamic light scattering: with applications to chemistry, biology, and physics*, Wiley.



# 6

## Conclusions and perspectives

### 6.1 Conclusions

Photonic crystal (PhC) cavities have been intensively investigated in recent years for biosensing applications due to their high quality (Q) factor and low mode volume (V). PhC cavities with high Q/V ratio enable enhanced light-matter interactions in the cavity mode volume and can in principle provide fast label-free detection with small detection limits. In this work, we have developed silicon based PhC cavities that have been fabricated by DUV lithography for sensing applications. We have provided both a theoretical methodology for the understanding of the sensing limits and technical process for the realization of such cavities.

In our case, where the PhC structures were fabricated with a fixed exposure dose using the standard 193 nm DUV lithography at imec, the patterned PhC holes had smaller diameter than the designed ones. A bias chart was introduced to achieve the dimension of holes as targeted by the design. The minimum feature size in this case was limited to 130 nm, which restricted the fabrication of various interesting PhC cavities. However, when the same structures were fabricated using immersion lithography, the offset in hole diameter and slot width between designed and fabricated PhC structures was as low as 2 nm (limited by SEM accuracy). The minimum feature in this case was 80 nm which makes this technology more flexible.

Decreasing the sensing volume  $V$  of the PhC cavity challenges the transportation of low concentration analytes with standard integrated microfluidic channels as the velocity of fluid vanishes at the channel wall. The delivery time for low concentration analytes in some biosensors can exceed days or weeks. This mass transportation problem significantly slows down the detection speed. In this thesis, we realized a sensor architectures in which the transportation of analytes to the sensor surface can be done more effectively.

We developed a methodology to fabricate a large array of PhC membrane without any substrate below it. The post-processing leads to the local removal of the silicon substrate in KOH and of the buried oxide in HF, which provides a free access from both side of the photonic structures. We showed that the proposed process is compatible with the integration of micrometer-sized SU8-based polymer waveguides. These polymer waveguides, together with high index contrast adiabatic nanometer-sized silicon inverted tapers, act as spot size converters. All relevant parameters and common pitfalls are mentioned for the reader eager to reproduce this technique. In addition, although a significant number of processing steps is required to achieve such free-standing substrate-less cavities, the quality ( $Q$ ) factors of the cavities that is of the order of a few thousand remains unaffected.

To characterize the sensing capability of our cavities, we have developed a technique that enables to spatially probe the perturbation induced by a nano-object. This technique consists in positioning a dielectric nano-fiber tip with apex diameter of few tens of nanometers in the near field of the cavity and simultaneously measuring the intensity variations of the cavity mode. The positioning of nano-tips of various apex sizes allowed us to determine the spectral sensitivity of the cavity. We could measure intensity variation when the tip was moved with a step of 10 nm axially towards or away from the cavity surface. Based on the noise floor that we measured in this experiment, it is possible to track the intensity variation even when the tip moves by a step of 5 nm axially. The thesis also explains the fabrication of such nano-tip fiber in the cleanroom of UGent.

We have also studied the detection limit of PhC cavities for sensing application. In particular, we have determined the trade-off between the detection limit and acquisition speed. The fundamental noise limit is currently reached for an acquisition sampling time  $t_{acq} \geq 3 \mu s$ . Such an intrinsic fundamental limit corresponds to 1/2000th the linewidth of the optical spectrum of photonic crystal cavities of effective mode volume as small as  $0.06 \mu m^3$ . Improving the amount of light collected out of the cavity is necessary to further push the minimal acquisition sampling time. The current study makes it possible to answer the

question: what is the trade-off between the acquisition speed and the detection limit to track a nanoparticle in real time with a resonant cavity field. In particular, our study shows that a single PhC cavity enables us to monitor up to 33 million particles per second with a particle size down to 34 nm with the currently achieved experimental conditions, and down to 10 nm by optimizing the light collection.

## 6.2 Perspectives

By introducing an external perturbation in the near field of a cavity, we have shown that it is possible to measure the variation of the intensity of the cavity mode at nanosecond scale. A substrate-less free-standing PhC cavity was also demonstrated, below which we can position a nano-object and at the same time record the intensity fluctuation from the top surface of the cavity. Next step in this regard would be to track the Brownian motion of a nanoparticle or a biomolecule that can be transported to the PhC cavity surface via micropipetting. The fast tracking of such nano-object in the near field of the PhC cavity will allow us to determine the diffusion coefficient and hence the hydrodynamic radius of these nano-objects accurately.

As an important result, the current thesis has revealed that PhC cavities of small mode volume are prone to thermo-refractive noise. This experimental highlight was performed in air. As biosensing is mostly carried out in water solution, there is a need to investigate the noise contribution when the cavity is surrounded by water. The impact of the fundamental density fluctuations of water on the detection limit of the cavity sensors is still an open question.

Probing a liquid solution can be done by using a micro-pipette that is positioned below the substrate-less free-standing PhC cavity. However, the liquid, e.g. water, will also fill the PhC holes, which can significantly decrease the Q factor of the cavity due to large absorption loss in the near infrared ( $\lambda=1.5\mu\text{m}$ ). Therefore, in order to avoid the infiltration of the holes, a very thin layer of low index material can be deposited on the top side of the PhC cavity before removing the BOX layer. The deposition of such a low index material can be implemented for example, by atomic layer deposition (ALD) technique.

The cavities that were fabricated with immersion lithography were the best to study the detection limit, in particular due to the absence of any Fabry-Perot oscillations. However, the space that was allocated for the current project was limited. As a consequence, the access waveguides were only 500  $\mu\text{m}$  long on each side of the PhC, which made it very difficult to cleave. For all the samples processed, most of the PhC structures got damaged while cleaving. For future runs, it is crucial to increase the length of the samples.

PhC based slot cavities has majority of electric field confined in air which results in strong overlap of the electric field with the target molecules. This improves the maximum achievable sensitivity. But when the substrate below the PhC cavity is removed, these slots based cavity undergoes severe buckling. Hence, there is a need to carefully design the mechanical support around such cavities to avoid any buckling.

As, all the PhC cavities in thesis were fabricated on a passive multi-project-wafer (MPW) run at imec but in future it is also possible to integrate a laser and a photodetector on the same chip which will enable complete on-chip sensing.



